

Takafumi Hayashi

Abstract

A detailed and accurate pretherapeutic evaluation of stage plays a crucial role in the prognosis as well as the choice and extent of the therapeutic procedure required for patients with oral cancer. For this purpose, various modern diagnostic imaging modalities are routinely used. In this section, the potential roles of conventional X-rays, computed tomography (CT), magnetic resonance imaging (MRI), ultrasonography (US), and positron emission tomography (PET)/CT in the staging of oral cancer are addressed.

Keywords

Diagnostic imaging • Magnetic resonance imaging • Ultrasonography • X-ray computed tomography

5.1 Imaging Techniques

5.1.1 Conventional X-Ray in Oral Cancer

A conventional X-ray is commonly used for surveillance of oral cancer. Because of the limited viewing direction, its role in staging of oral cancer is limited. This technique renders a three-dimensional volume onto a two-dimensional plane. As a consequence, overlying and underlying tissues and structures are superimposed, which generally results in reduced conspicuity as well as subject contrast.

5.1.1.1 Dental X-Ray

The detailed shape of the margins of bone absorption in gingival carcinoma can be assessed with a dental X-ray. Small fragments of the destroyed bone can also be detected.

The exact extent of the tumor involvement can hardly be evaluated because of the superimposition of adjacent structures.

5.1.1.2 Orthopantomography (Panoramic X-Ray)

Orthopantomography is a two-dimensional half-circle view of the upper and lower jaws from ear to ear obtained by panoramic X-ray scanning. Its intrinsic value is screening for malignancy in routine dental practice. Marked maxillary or mandibular bone absorption caused by gingival, floor of mouth, and tongue carcinomas can be detected by orthopantomography. However, the diagnostic sensitivity for the extent of tumor involvement is insufficient compared with modern sectional imaging modalities such as computed tomography (CT) and magnetic resonance imaging (MRI), because of the limited viewing direction. From the viewpoint of treatment outcome, the Japan Society for Oral Tumors (JSOT) proposed a classification regarding the shape of the absorbed bone involved in gingival carcinoma [1]. The characteristic shape of the absorbed bone margin was classified into three types: pressure type; moth-eaten type; and intermediate type (Fig. 5.72). Moth-eaten type, which commonly shows a poorer outcome, is applied if an ill-defined permeated margin and small bone fragments within the lesion are observed.

T. Hayashi, D.D.S., Ph.D. (✉)
Division of Oral and Maxillofacial Radiology, Niigata University
Graduate School of Medical and Dental Sciences,
2-5274 Gakkocho-dori, Chuo-ku, Niigata 951-8514, Japan
e-mail: hayashi@dent.niigata-u.ac.jp

5.1.1.3 Other Conventional X-Ray

Posteroanterior projection and Waters projection X-rays can occasionally reveal bone destruction at the lateral portion of the maxilla and mandibular bone structure, which might be overlooked by orthopantomography.

5.1.2 CT in Oral Cancer

5.1.2.1 Plain CT and CECT

CT is a fundamental cross-sectional imaging modality for evaluating oral cancer and is superior for detecting cortical bone destruction and intratumoral calcification compared with other imaging modalities [2]. As modern CT equipment can deal with isotropic voxel data, three-dimensional evaluation using multiplanar reformatted images is routinely used to define the extent of tumor involvement. Contrast-enhanced CT (CECT) using iodine contrast materials is an excellent modality for oral cancer staging, i.e., determining the tumor extent (especially depth of invasion) and size, identifying lymph node metastases, assessing response to therapy, and evaluating recurrent disease.

On CT, tumors appear as homogeneous or heterogeneous soft-tissue-attenuated lesions that are variably enhanced after intravenous administration of iodine contrast materials [3]. Commonly, the tumor is intensely enhanced compared with adjacent normal structures because of the tumor neoangiogenesis, and a central necrotic portion is frequently identified as a non-enhanced or barely enhanced hypodense area within the tumor mass. There may be early or prominent enhancement of the tumor margins, because of the higher vascularity of the tumor periphery.

Tumors located around the occlusal plane level are frequently obscured with metallic artifacts caused by dental prostheses. A CT image is also degraded by motion artifacts, but is less affected by breathing and swallowing artifacts than MRI. Good-quality imaging obtained with CT is readily reproducible. A soft-tissue window setting image with a soft-tissue algorithm at a level of 40–50 with a window width of 250–350 is recommended for discrimination of enhanced tumor tissue. In addition, a bone window setting with a bone algorithm should be used for osseous involvement of the tumor (thin slice images of less than 1 mm are preferable). For routine examination in oral cancer, contiguous scanning from the level of the nasopharynx to the level of the supraclavicular fossa is recommended.

5.1.2.2 CT Perfusion

CT Perfusion (CTP) is a technique that measures the parameters of tissue perfusion through dynamic acquisition of images after contrast material administration (Fig. 5.130) [2]. The physiologic basis of contrast enhancement on CT closely mimics the physiologic effects of tumor angiogenesis.

Angiogenesis is a key factor for tumor growth and metastasis and is a complex process that includes endothelial cell breakdown, proliferation, and migration stimulated by angiogenic factors. CTP can be routinely performed on all modern CT equipment and is potentially useful to distinguish neoplasms from normal structures and posttreatment changes. The major drawback of CTP is an excessive radiation exposure dose, and therefore lower tube voltages and mAs are recommended.

5.1.3 CBCT in Oral Cancer

As a modern cone-beam CT (CBCT) system has relatively higher spatial resolution compared with a CT system, the significance of CBCT in the evaluation of osseous involvement is almost equal or superior to the bone-algorithm CT. The major disadvantage of CBCT is poor soft-tissue contrast because of the limited radiation exposure. The tumor mass is hardly visualized clearly with CBCT, and therefore neoplastic processes are frequently overlooked. The limited field of view is another drawback of CBCT in the evaluation of tumor extent. Therefore, the role of CBCT in oral cancer staging is limited.

5.1.4 MRI in Oral Cancer

5.1.4.1 Plain MRI and Contrast-Enhanced MRI

MRI uses the magnetic properties of hydrogen and its interactions with both a large external magnetic field and radio waves to produce highly detailed images of the human body.

MRI has superior soft-tissue contrast compared with CT and may provide better delineation of soft-tissue invasion of the carcinoma [3]. The lack of ionizing radiation makes it the preferred technique in patients with iodine allergy. There is also the advantage of reduced metallic artifacts from metallic dental prostheses. However, the images are often degraded by magnetic metallic materials and unexpected oral motion. The major drawbacks of MRI are the relatively high cost and claustrophobia.

On conventional T1-weighted images obtained without fat saturation, a squamous cell carcinoma (SCC) has intermediate signal intensity and is generally isointense to muscle. On T2-weighted images, an SCC is typically heterogeneous and hyperintense to normal muscle, making it more conspicuous. However, the tumor size might be overestimated on T2-weighted images because the tumor cannot be distinguished from surrounding inflammation and edema. On gadolinium-enhanced T1-weighted images, the tumor has variable enhancement and conspicuity. Fat-saturated images are helpful in distinguishing tumors from normal surrounding structures. Axial and coronal contrast-enhanced T1-weighted images with fat saturation are superior to CT

for defining the soft-tissue extent. One of the disadvantages of fat saturation is increased susceptibility to artifacts, particularly in locations near the bone or air.

MRI is the optimal modality for detection of perineural tumor spreading [3]. Direct signs of perineural tumor spreading are enlargement, irregularity, and abnormal enhancement of the major cranial nerves and their branches. Replacement of high-intensity fat-containing spaces adjacent to the major skull foramina, such as the pterygopalatine fossa, by tumor tissue is also a valuable clue to the presence of perineural tumor spreading. Although CT is generally considered superior for detection of cortical erosion, MRI is more sensitive for identification of early bone marrow invasion. Findings suggestive of marrow invasion are replacement of normal high-intensity marrow fat by tumor tissue. Dynamic contrast-enhanced MRI provides better delineation of the tumor margin.

5.1.4.2 Diffusion-Weighted MRI

Diffusion reflects the random motion of molecules, and diffusion-weighted imaging (DWI) is an MRI technique wherein images are weighted with the local characteristics of water diffusion [2]. The apparent diffusion coefficient (ADC) is a measure of the magnitude of freedom of water diffusion. Higher ADC values indicate greater magnitude of water diffusion, while lower ADC values indicate lesser magnitude of water diffusion and restricted motion. The DWI signal intensity is dependent on the magnitude of water motion. Highly cellular tissues exhibit lower ADC values than acellular or hypocellular tissues. Generally, the ADC of malignant lesions is lower than that of benign lesions (Figs. 5.54, 5.80 and 5.103). Malignant lymph nodes tend to have lower ADC values than nonmalignant lymph nodes.

5.1.5 Ultrasonography (US) in Oral Cancer

US is based on the pulse-echo principle, in which a short burst of ultrasound is emitted from a transducer and directed into a tissue, and echoes are produced as a result of the interactions of the ultrasound with the tissue, traveling back to the transducer. By timing the period that elapses between the emission of the pulse and the reception of the echo, the distance between the transducer and the echo-producing structure can be calculated. US is a real-time, multiplanar, dynamic assessment technique for oral, maxillofacial, and neck structures. The high spatial resolution of modern US equipment is superior to CT and MRI. US has limited beam penetration, with the depth inversely proportional to the frequency. Power or color Doppler sonography is useful for detection of blood flow. Elastasonography has a potential role in differentiating benign tissue from malignant tissue (Figs. 5.123 and 5.129).

5.1.5.1 Intraoral US

A small carcinoma (T1, T2) of the mobile tongue and buccal mucosa may be visualized by intraoral US (Figs. 5.60 and 5.68) [1]. Intraoral US is performed by direct contact with the surface of the carcinoma, and therefore a small intraoperative transducer is preferable. If a thin polymer gel pad is placed as an acoustic coupling device between the probe surface and the tumor surface, three layers are clearly distinguished: (a) surface layer (hyperechoic line); (b) mucosal layer (hypoechoic line); and (c) submucosal and muscular layer (heterogeneous internal echo). Commonly, an SCC arising from the mucous membrane appears as a focal hypoechoic area continuous with the surrounding normal mucosal layer and the depth of invasion can be measured accurately (Figs. 5.60 and 5.68). Evaluation of the invasion depth of a tongue carcinoma may be useful for prediction of subsequent lymph node metastasis. In addition, Doppler US demonstrates prominent vascularity around the deep margins, arising from neoangiogenesis at the tumor invasion front. Intraoral US has a superior ability to evaluate the depth of invasion of a tumor compared with other imaging modalities.

5.1.5.2 Face and Neck US

Nodal involvement is the most important prognostic factor for oral cancer. US is the most accurate method currently available for detecting neck lymph node metastasis. Retropharyngeal and mediastinal nodes are inaccessible by US and require evaluation by CT or MRI. The US features of metastatic nodes are round shape, heterogeneity, loss of normal hilum, internal necrosis, and peripheral vascularity (Figs. 5.122 and 5.128). An ill-defined border in a metastatic node suggests extracapsular spread. With regard to internal necrosis, marked cystic degeneration is interpreted as a hypoechoic or non-echoic area with an irregular margin, whereas keratinization is demonstrated as an ill-defined hyperechoic area within a node [1]. However, diffuse-spreading tumor tissue that lacks obvious necrosis may be overlooked on a routine B-mode image only.

5.1.6 PET/CT in Oral Cancer

Positron emission tomography (PET)/CT, reflecting PET combined with CT, is the best modality for staging, monitoring, and surveillance of advanced oral cancer (Fig. 5.125) [2]. The utility of PET/CT in staging depends on the size of the primary tumor, and therefore PET/CT is not useful for a very small tumor. PET/CT is useful for identifying unsuspected additional primary tumors and/or distant metastases at the time of staging of a known primary tumor. ¹⁸F-fluorodeoxyglucose (FDG) is transported into cells like glucose by transmembrane transporters and becomes

trapped, thereby accumulating in cells with high glucose metabolism. The standardized uptake value (SUV) is the quantified measure of FDG uptake. However, the SUV is highly dependent on the machine used and the patient characteristics. A small tumor size limits the detection of FDG uptake and the minimal size limit is about 5 mm. Normal physiologic uptake should be encountered. Normal salivary glands exhibit low-level FDG uptake, while lymphoid tissue uptake is highly variable, especially at the tonsils and tongue base.

5.2 Sectional Anatomy of the Oral Cavity (Figs. 5.1, 5.2, 5.3, 5.4, 5.5, 5.6, 5.7, 5.8, 5.9, 5.10, 5.11, 5.12, 5.13, 5.14, 5.15, 5.16, 5.17, 5.18, 5.19, 5.20, 5.21, 5.22, 5.23, 5.24, 5.25, 5.26, 5.27, 5.28, 5.29, 5.30, 5.31, 5.32, 5.33, 5.34, 5.35, 5.36, 5.37, 5.38, 5.39, 5.40, 5.41, 5.42, 5.43, 5.44, 5.45, 5.46 and 5.47)

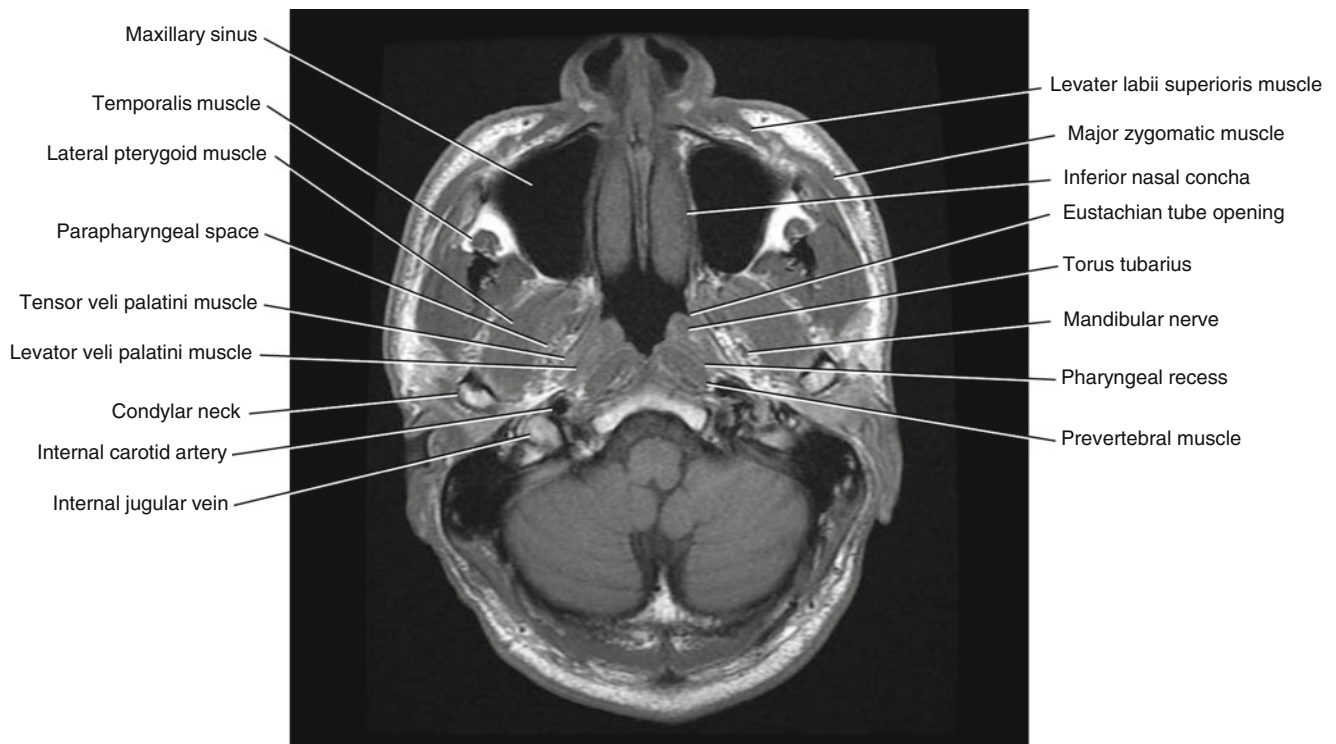


Fig. 5.1 Axial T1-weighted MRI

5.3 Oral Cancer Staging

5.3.1 TNM (UICC Staging)

(Mainly cited from: 2010 American Joint Committee on Cancer Definitions of TNM for the Lip and Oral cavity [4])

5.3.2 Primary Tumor (T)

T factor

TX Primary tumor cannot be assessed

T0 No evidence of primary tumor

Tis Carcinoma in situ

T1 Tumor 2 cm or less in greatest dimension

T2 Tumor more than 2 cm but not more than 4 cm in greatest dimension

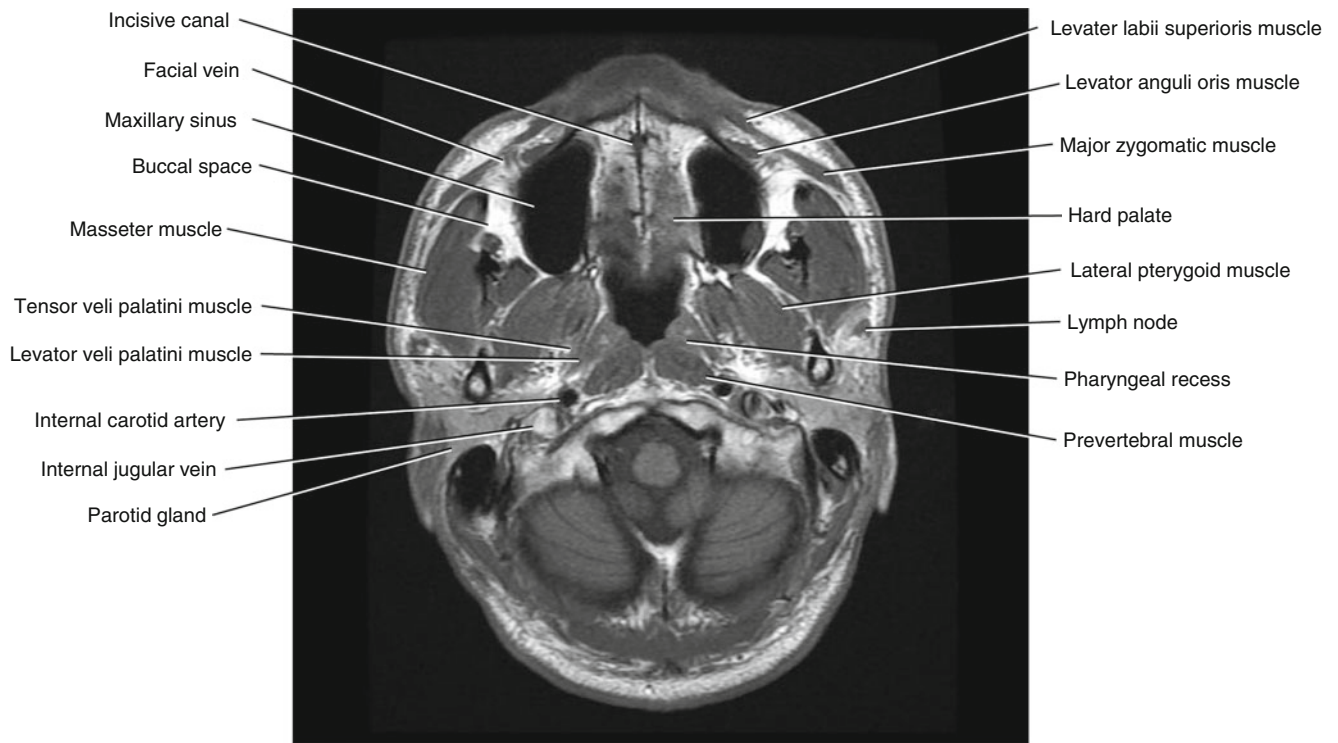


Fig. 5.2 Axial T1-weighted MRI

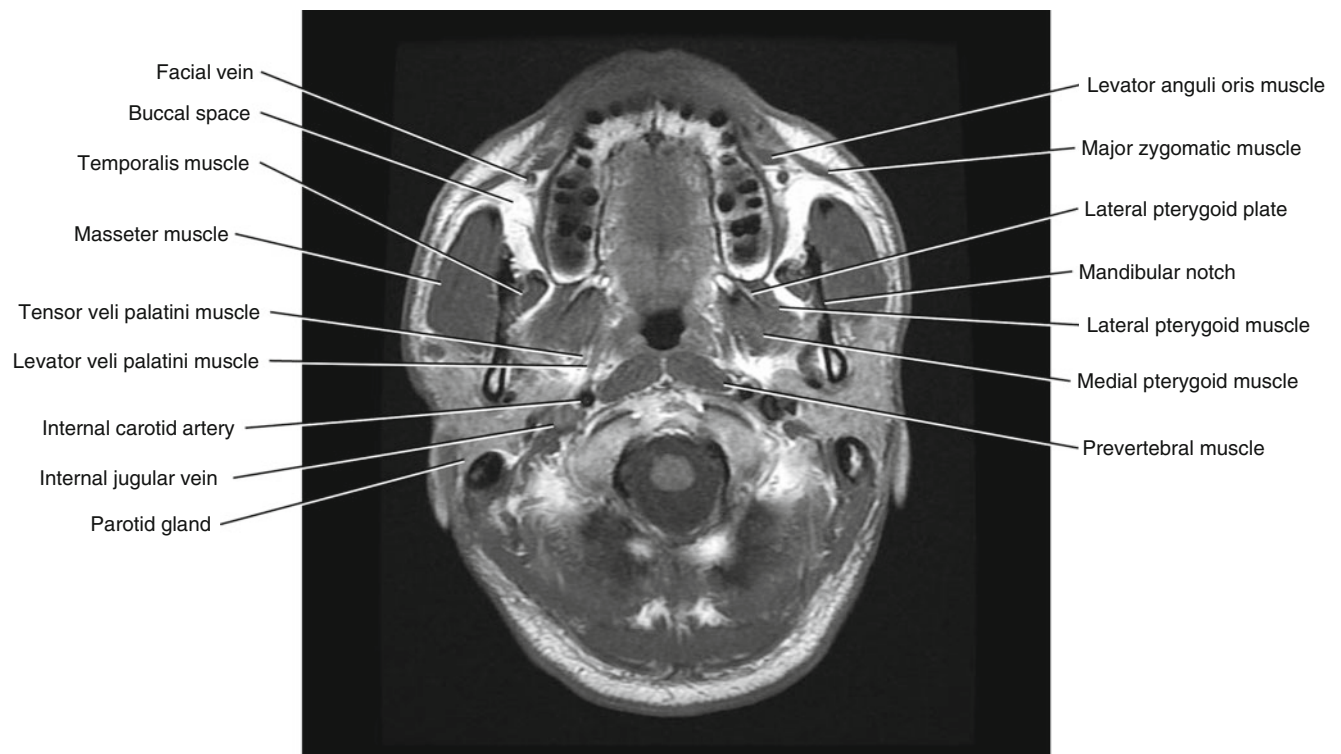


Fig. 5.3 Axial T1-weighted MRI

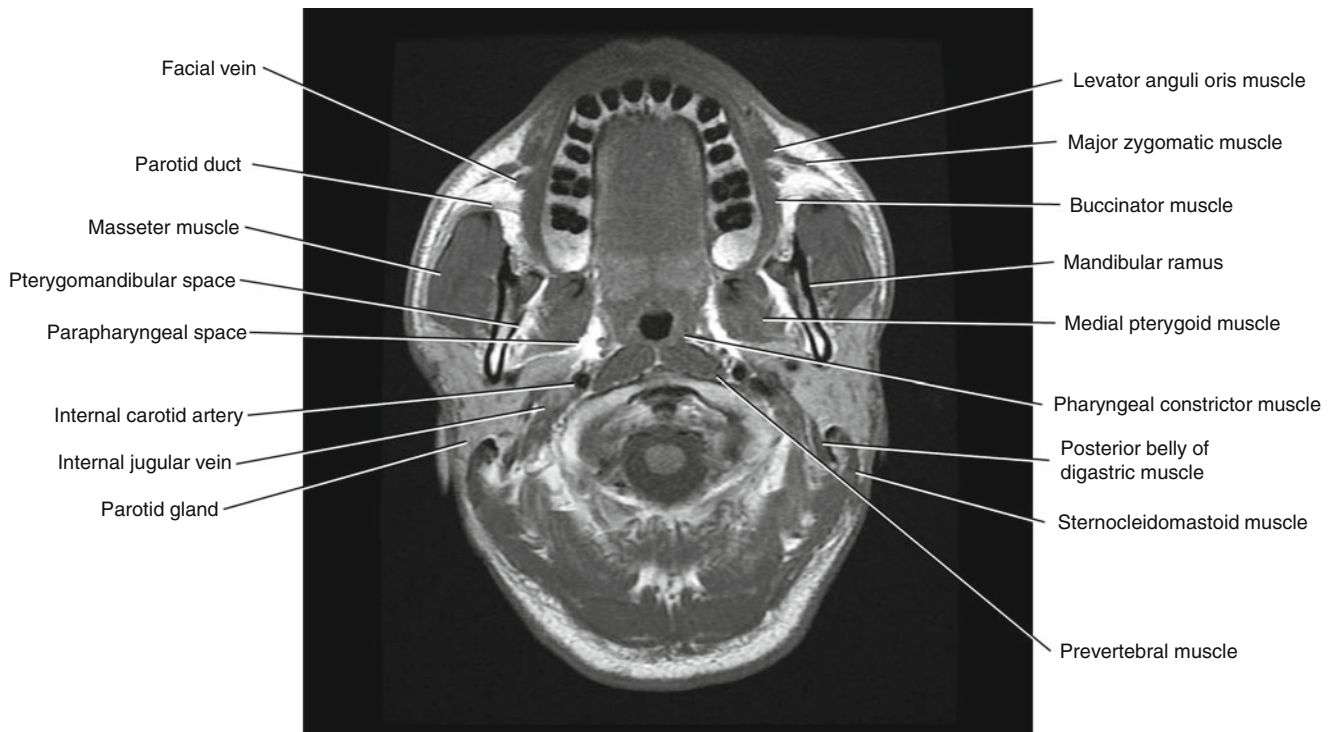


Fig. 5.4 Axial T1-weighted MRI

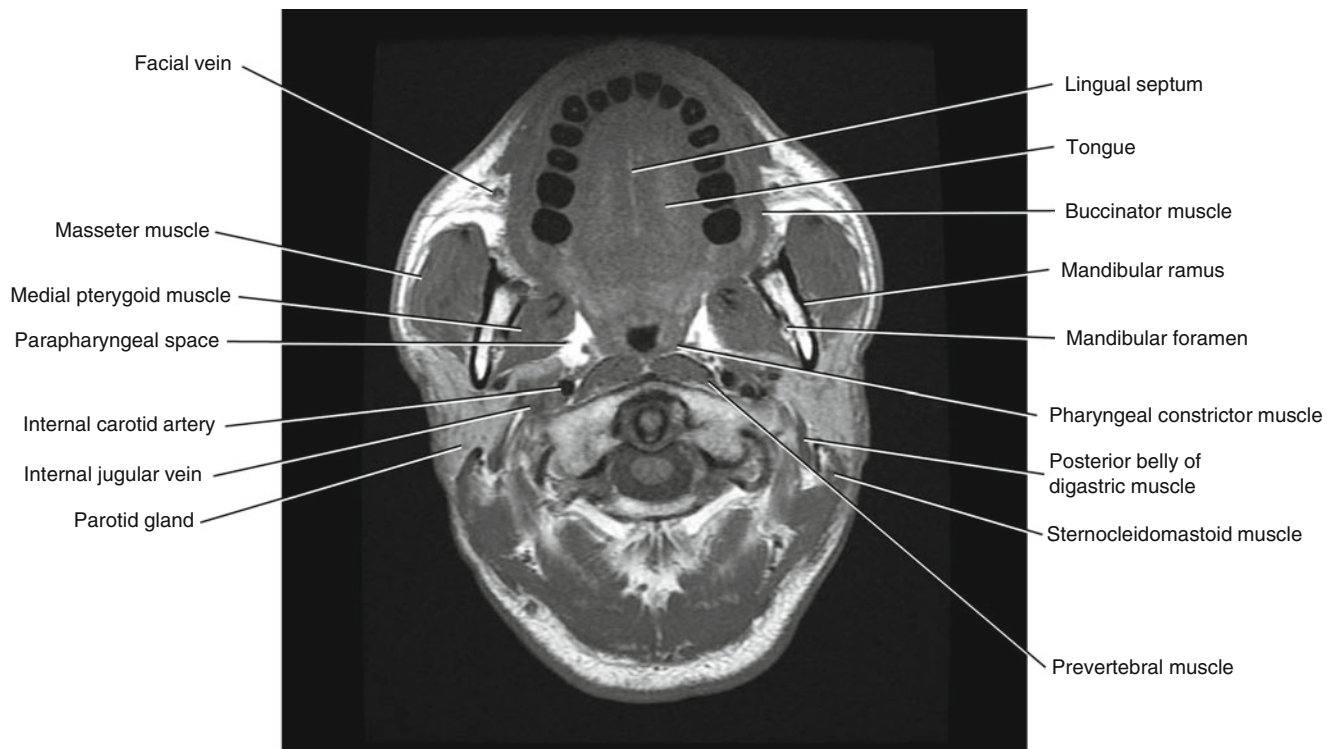


Fig. 5.5 Axial T1-weighted MRI

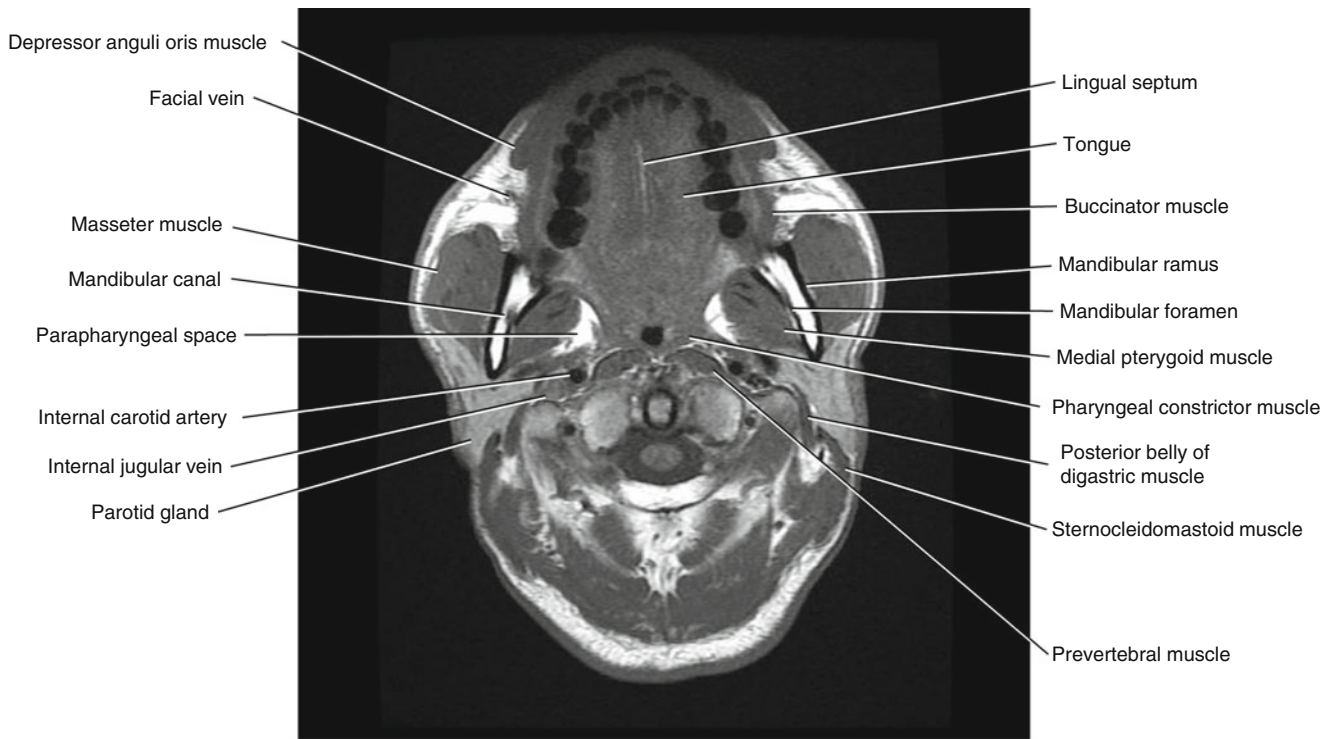


Fig. 5.6 Axial T1-weighted MRI

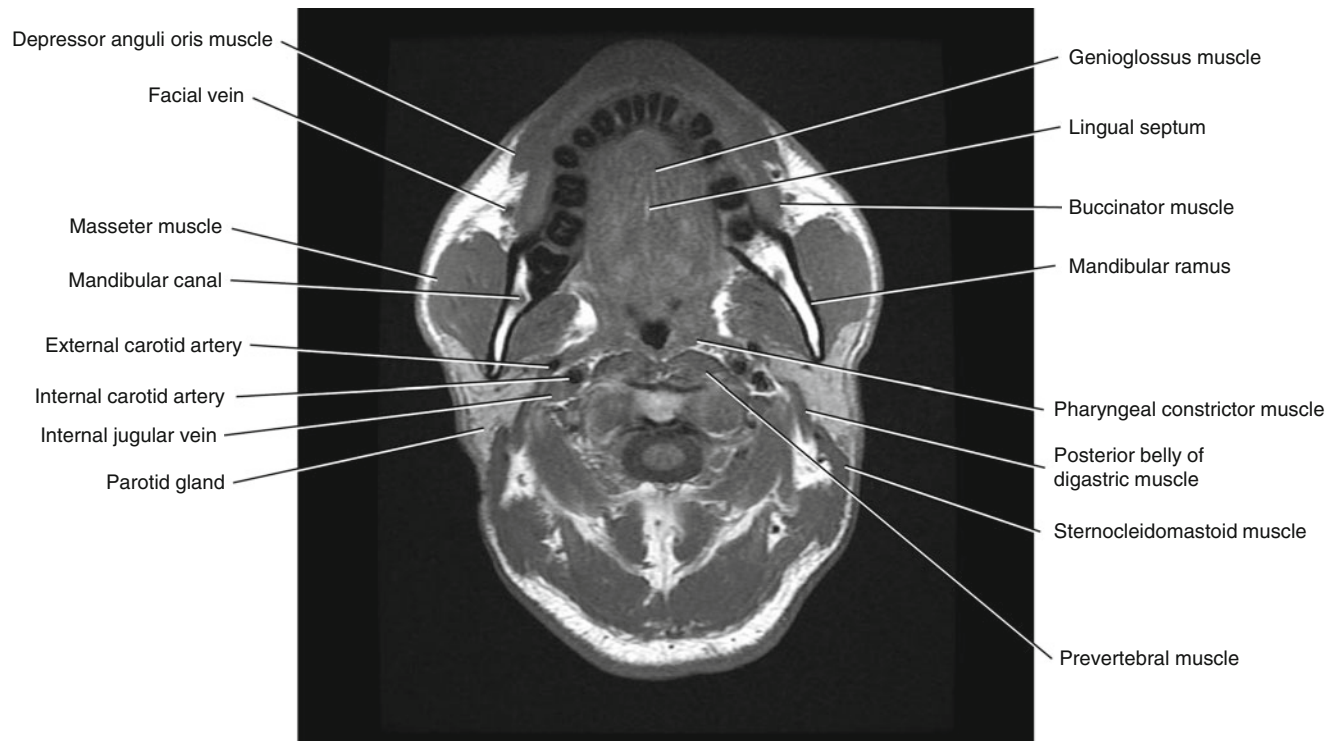


Fig. 5.7 Axial T1-weighted MRI

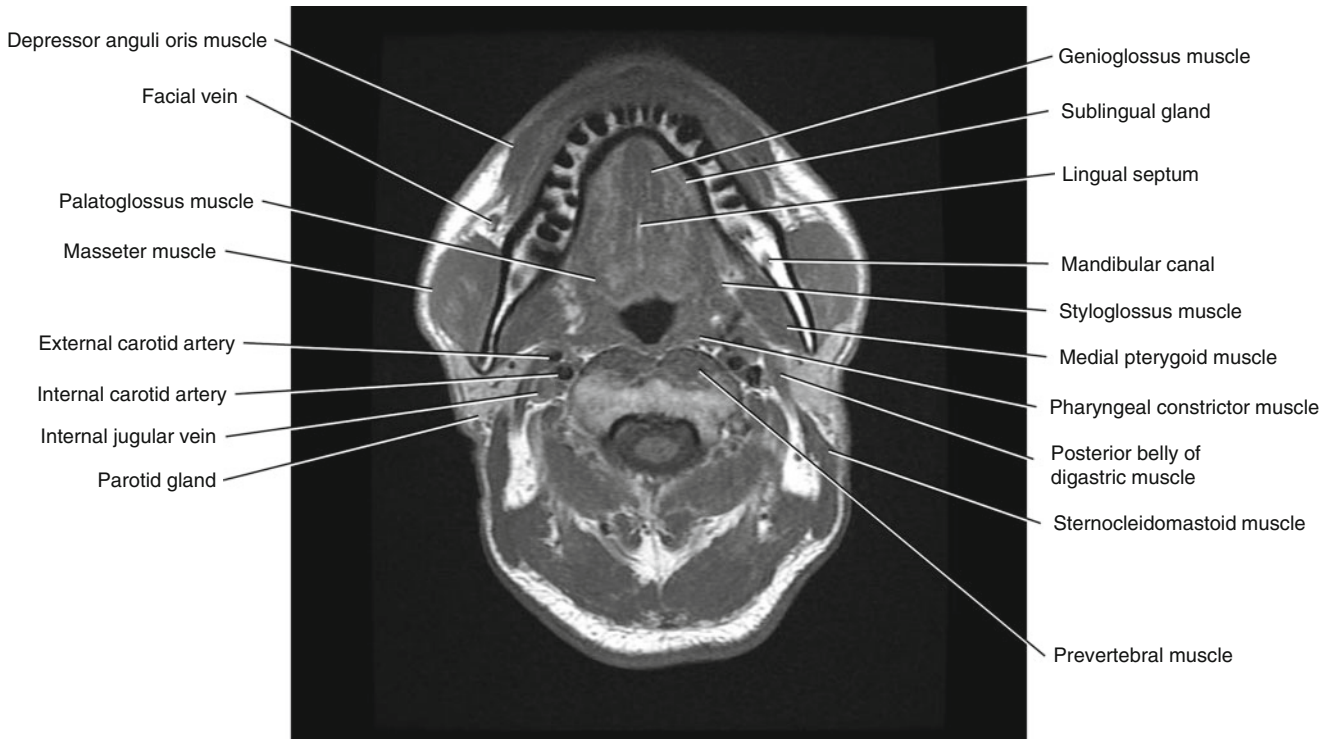


Fig. 5.8 Axial T1-weighted MRI

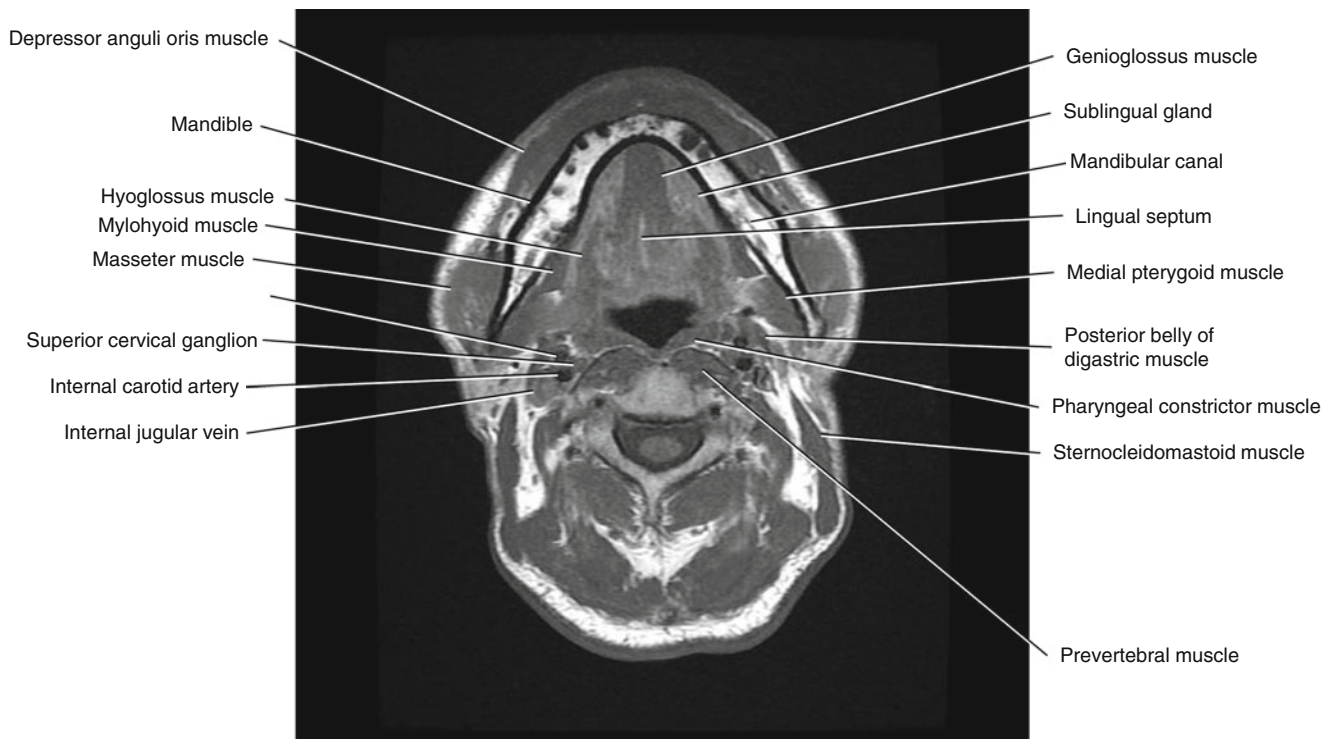


Fig. 5.9 Axial T1-weighted MRI

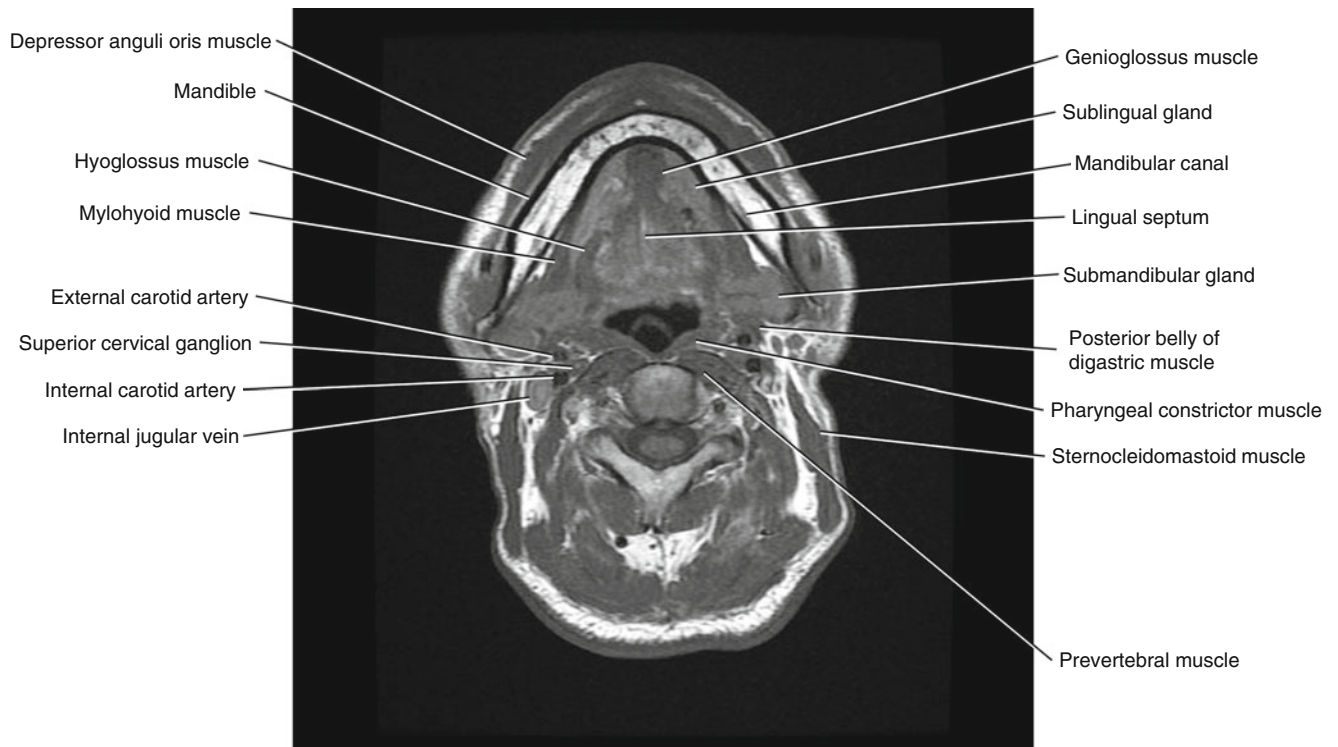


Fig. 5.10 Axial T1-weighted MRI

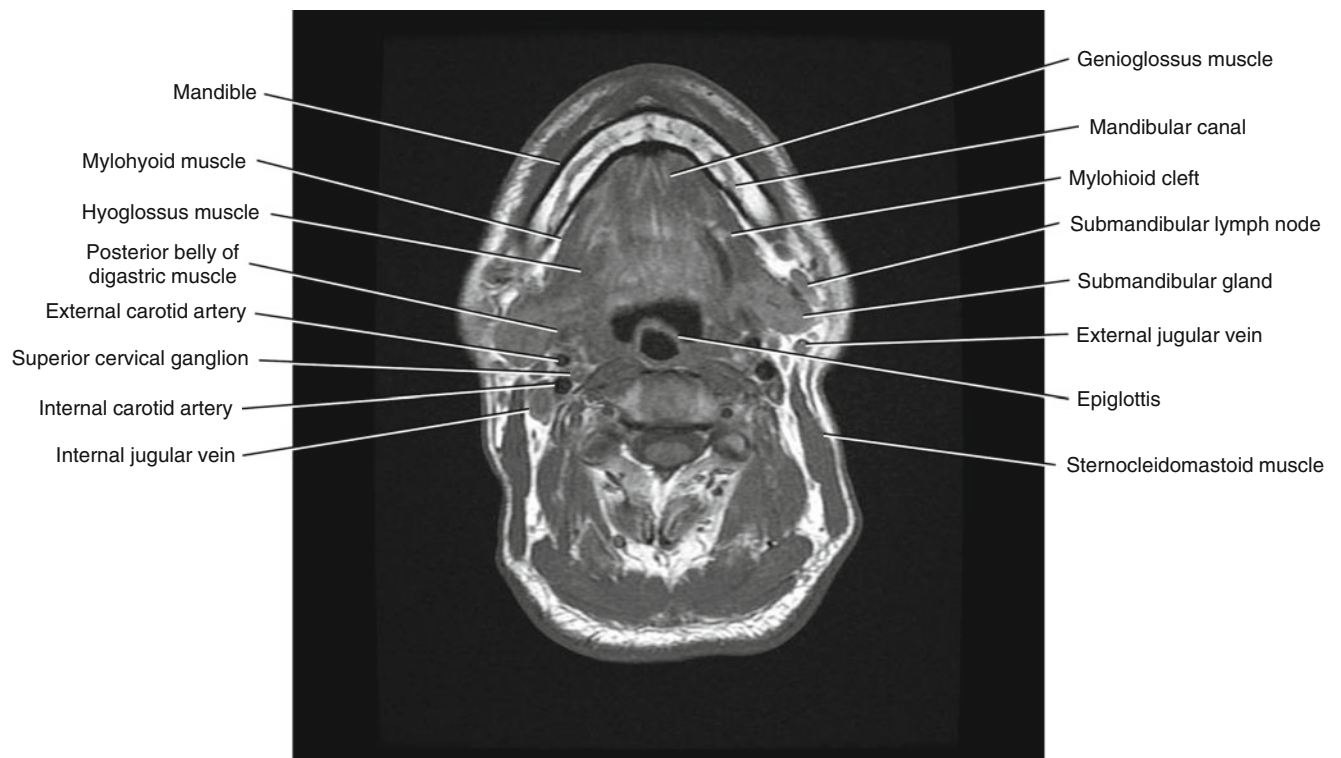


Fig. 5.11 Axial T1-weighted MRI

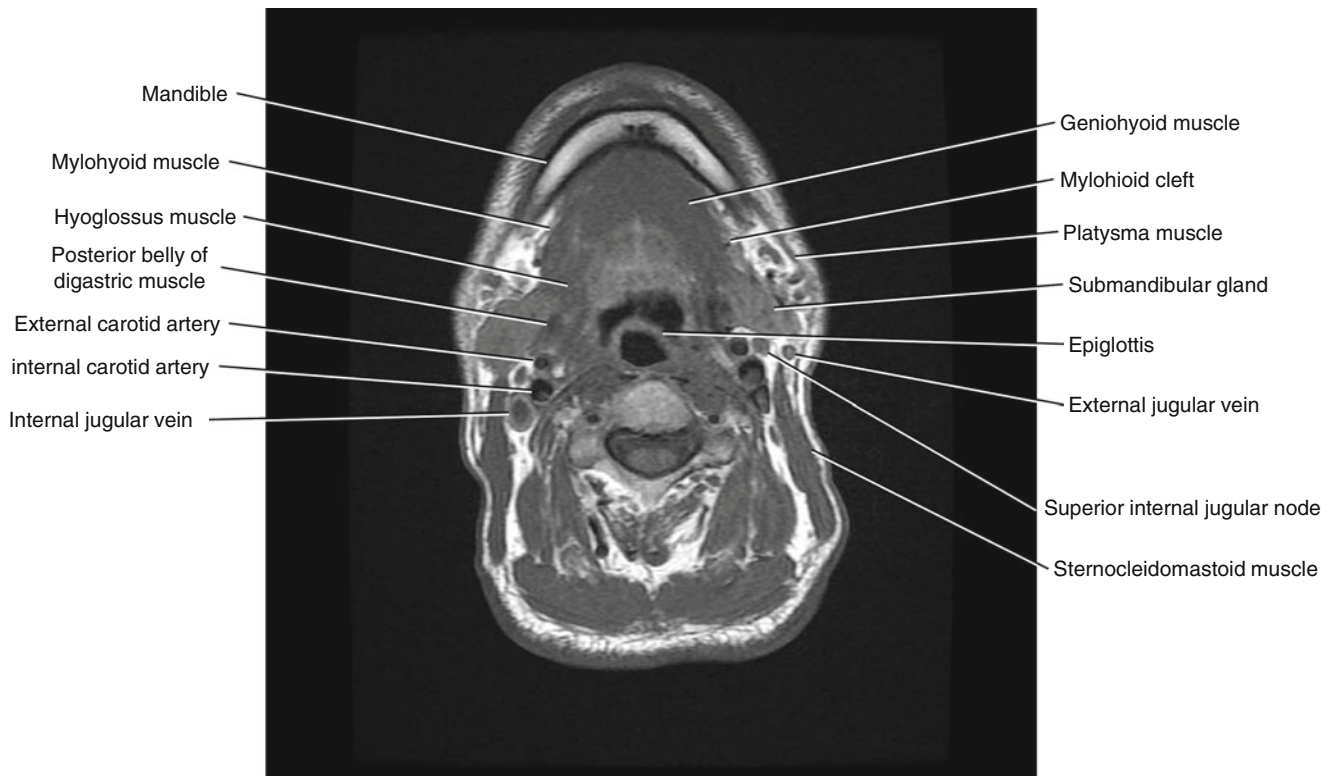


Fig. 5.12 Axial T1-weighted MRI

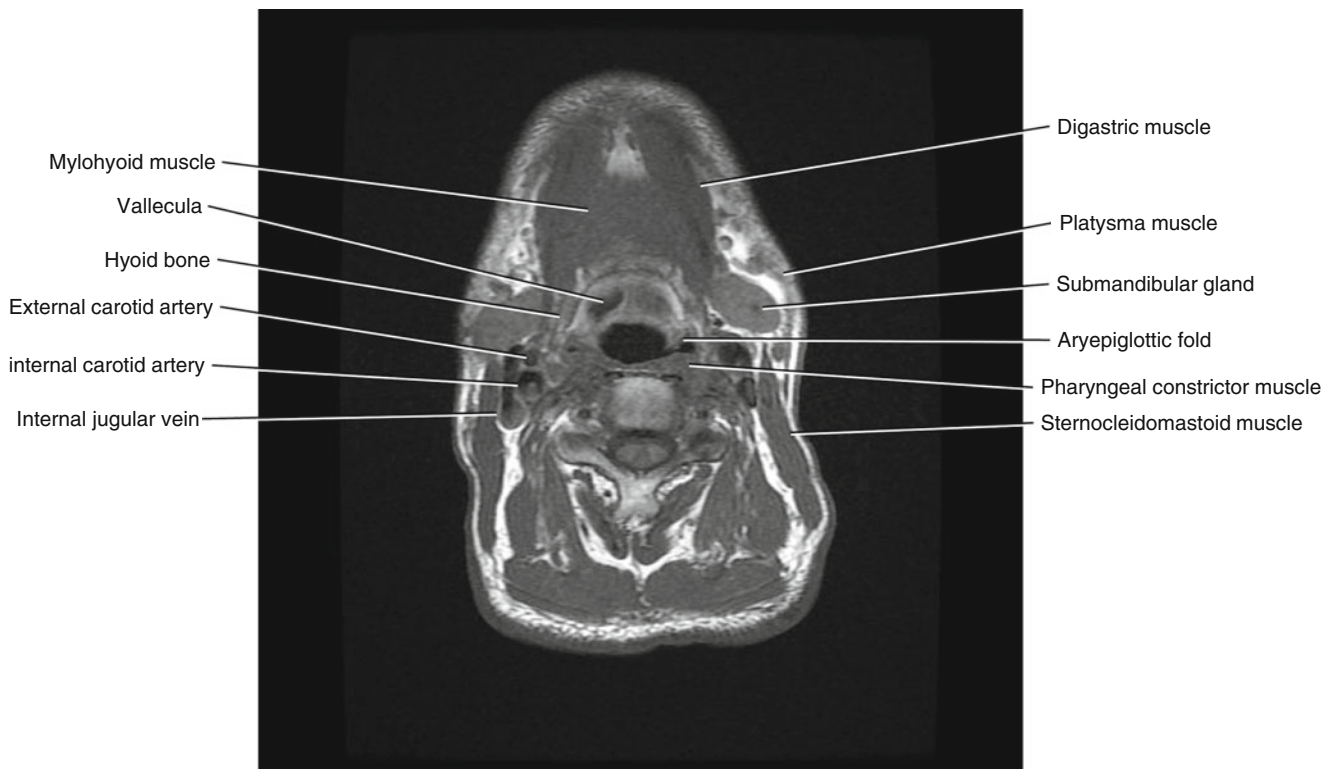


Fig. 5.13 Axial T1-weighted MRI

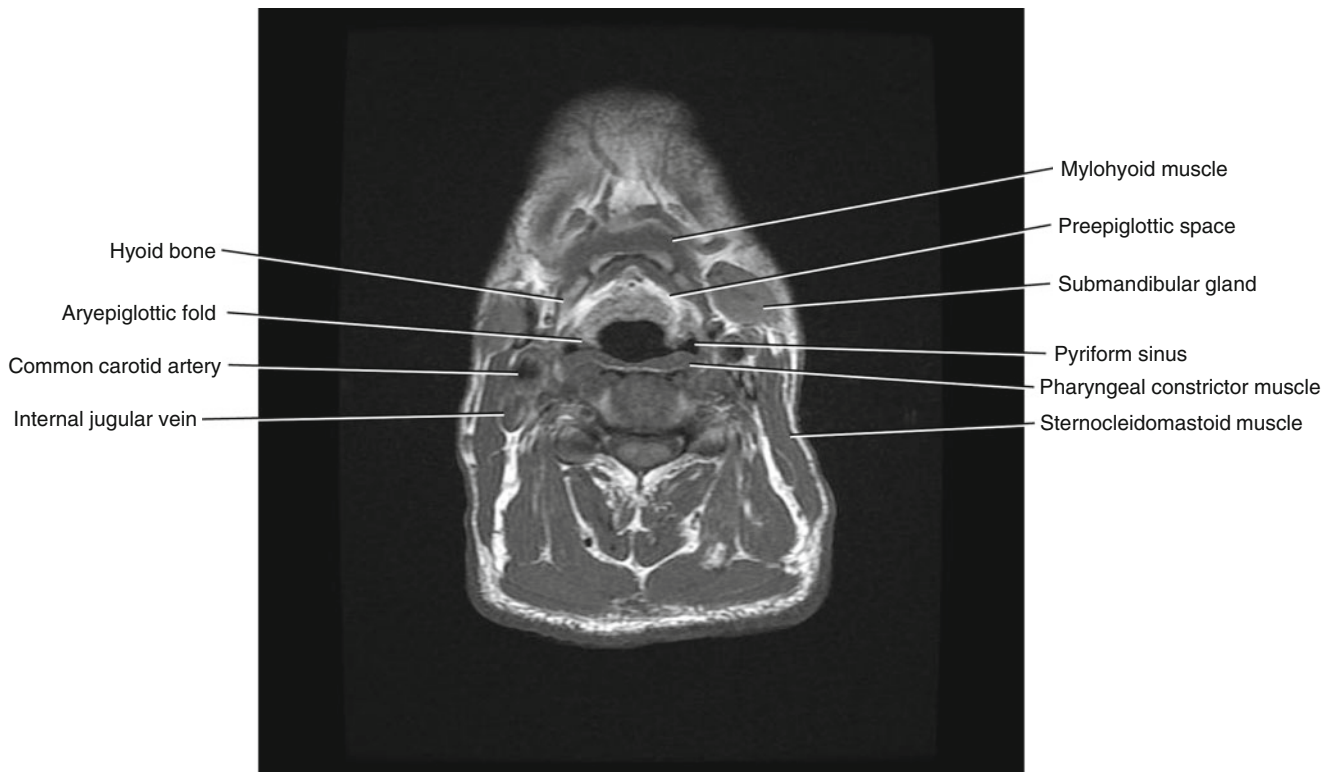


Fig. 5.14 Axial T1-weighted MRI

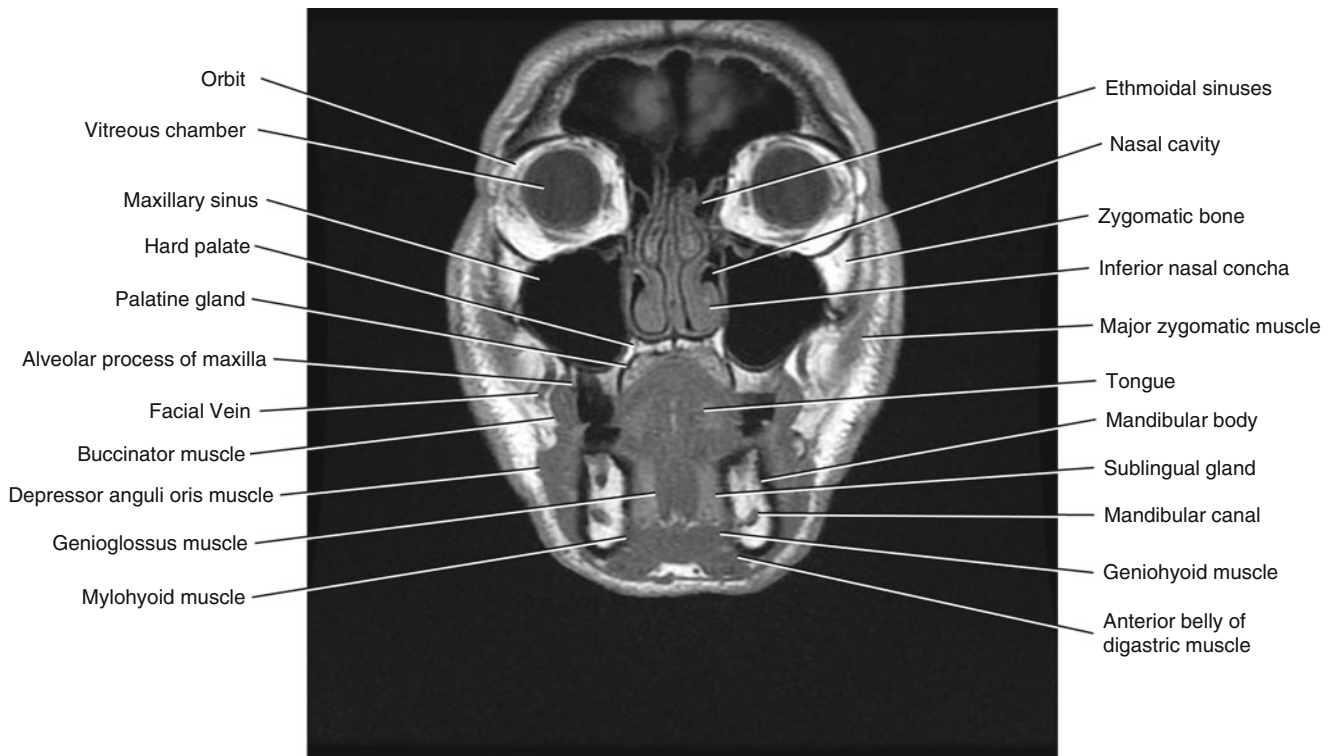


Fig. 5.15 Coronal T1-weighted MRI

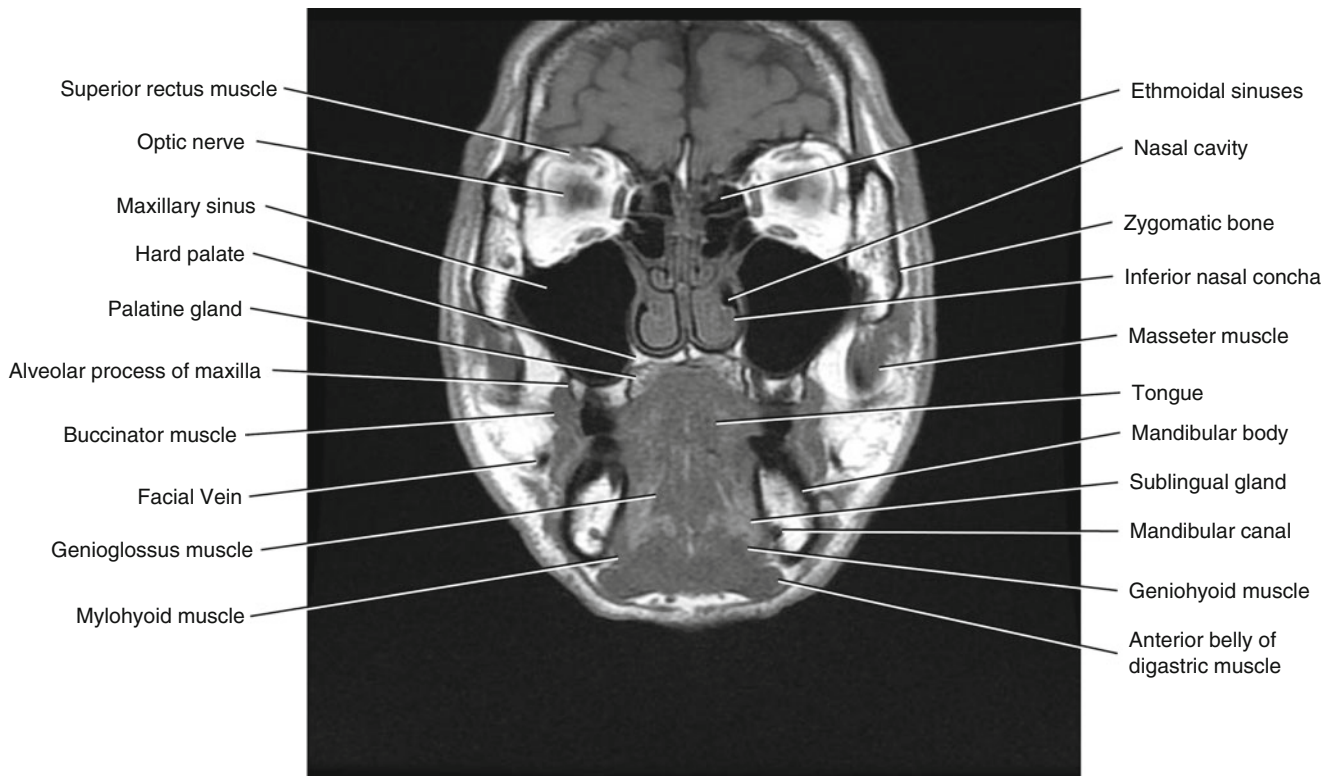


Fig. 5.16 Coronal T1-weighted MRI

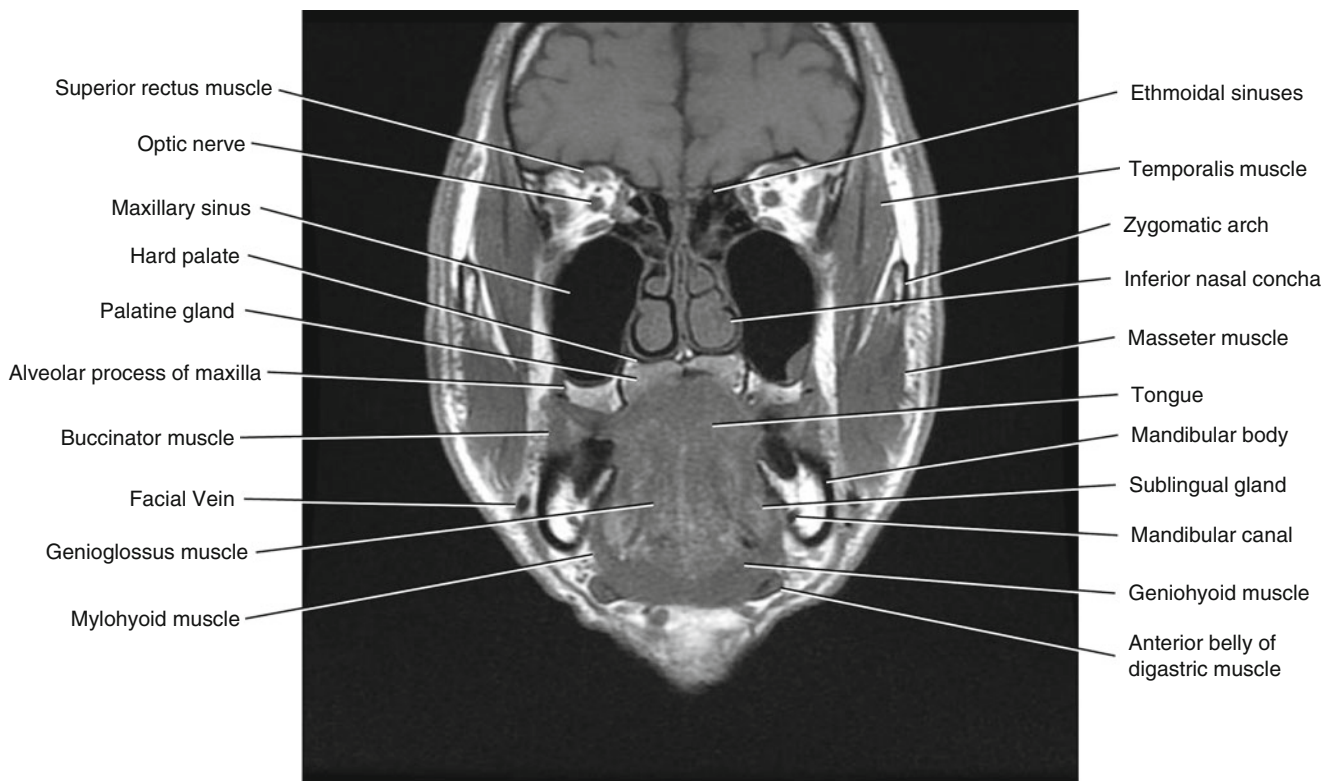


Fig. 5.17 Coronal T1-weighted MRI

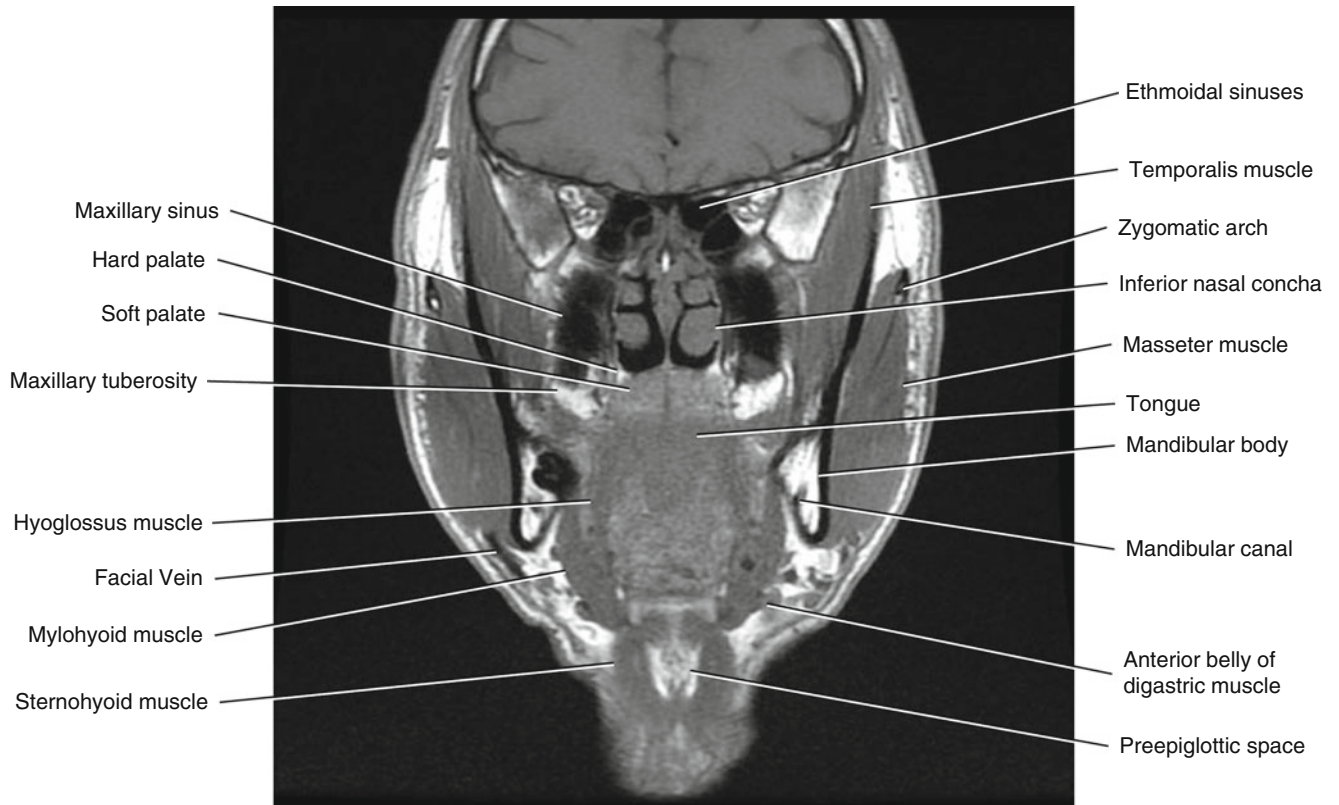


Fig. 5.18 Coronal T1-weighted MRI

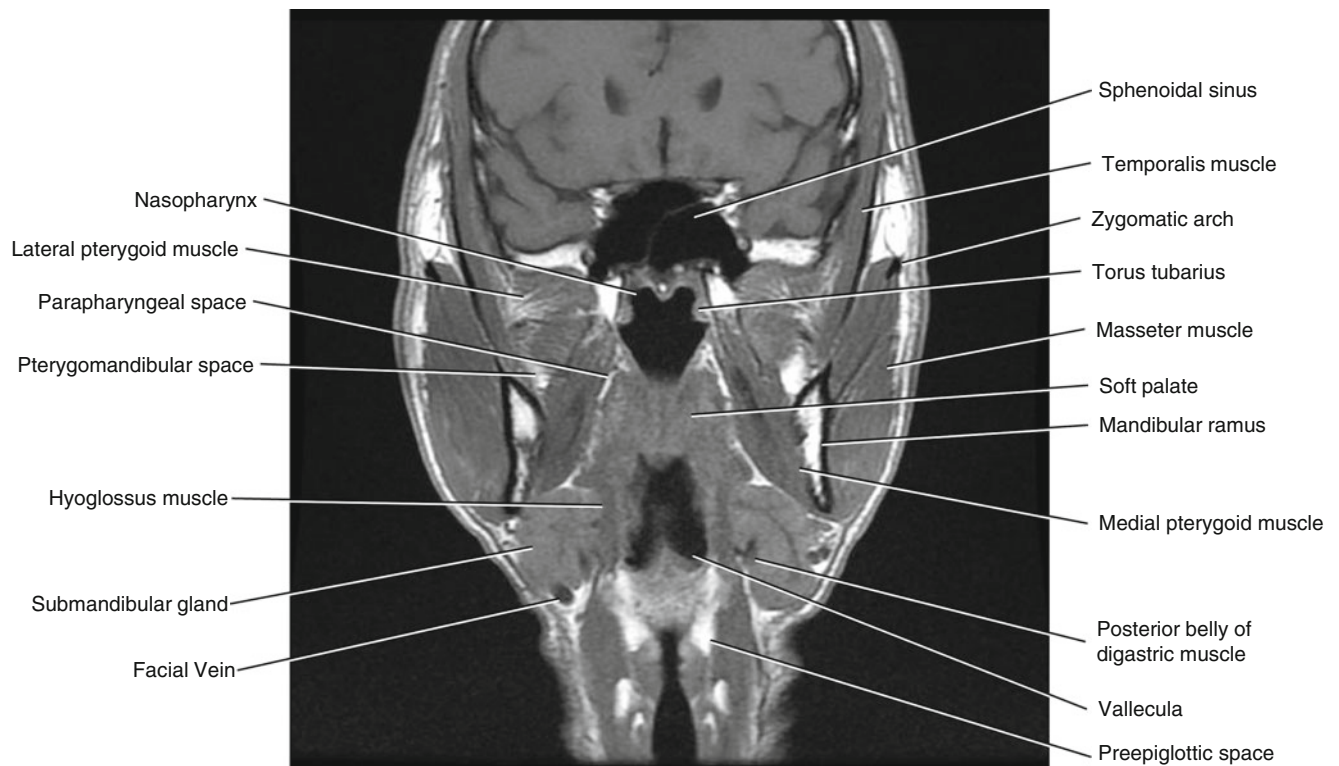


Fig. 5.19 Coronal T1-weighted MRI

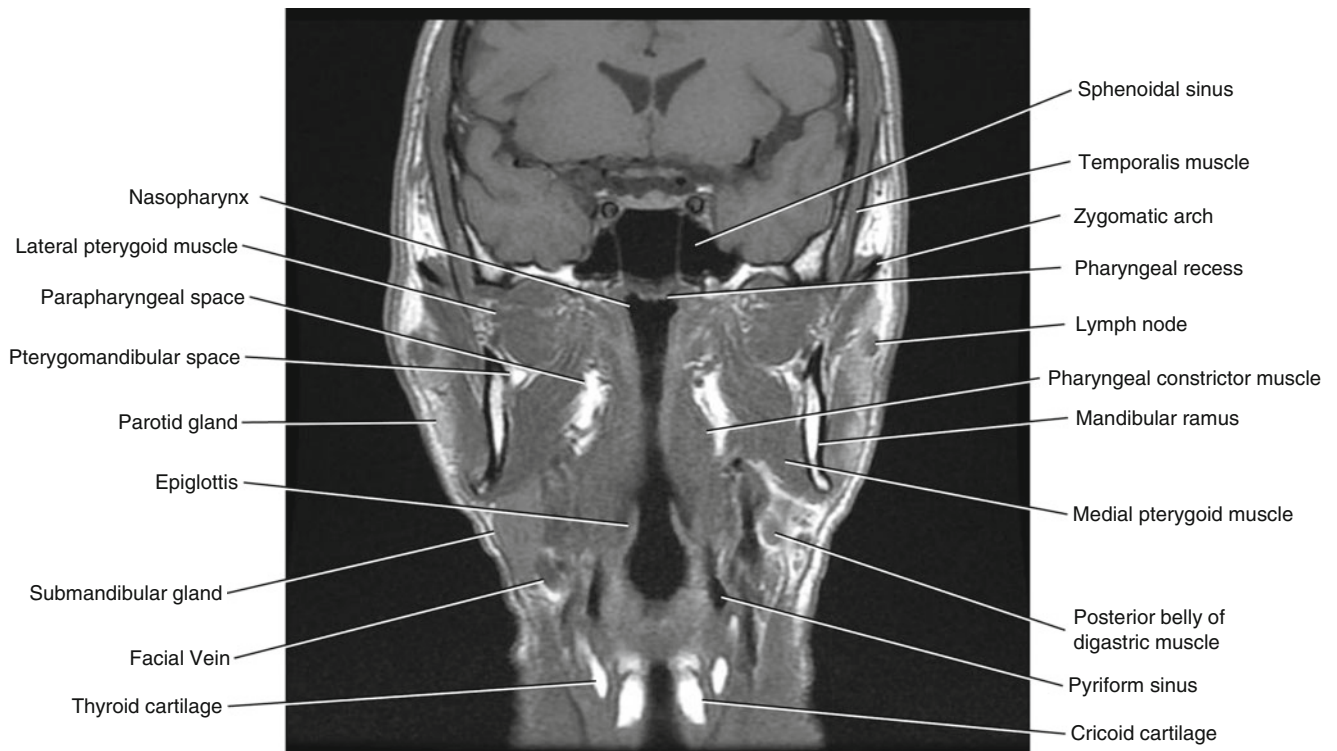


Fig. 5.20 Coronal T1-weighted MRI

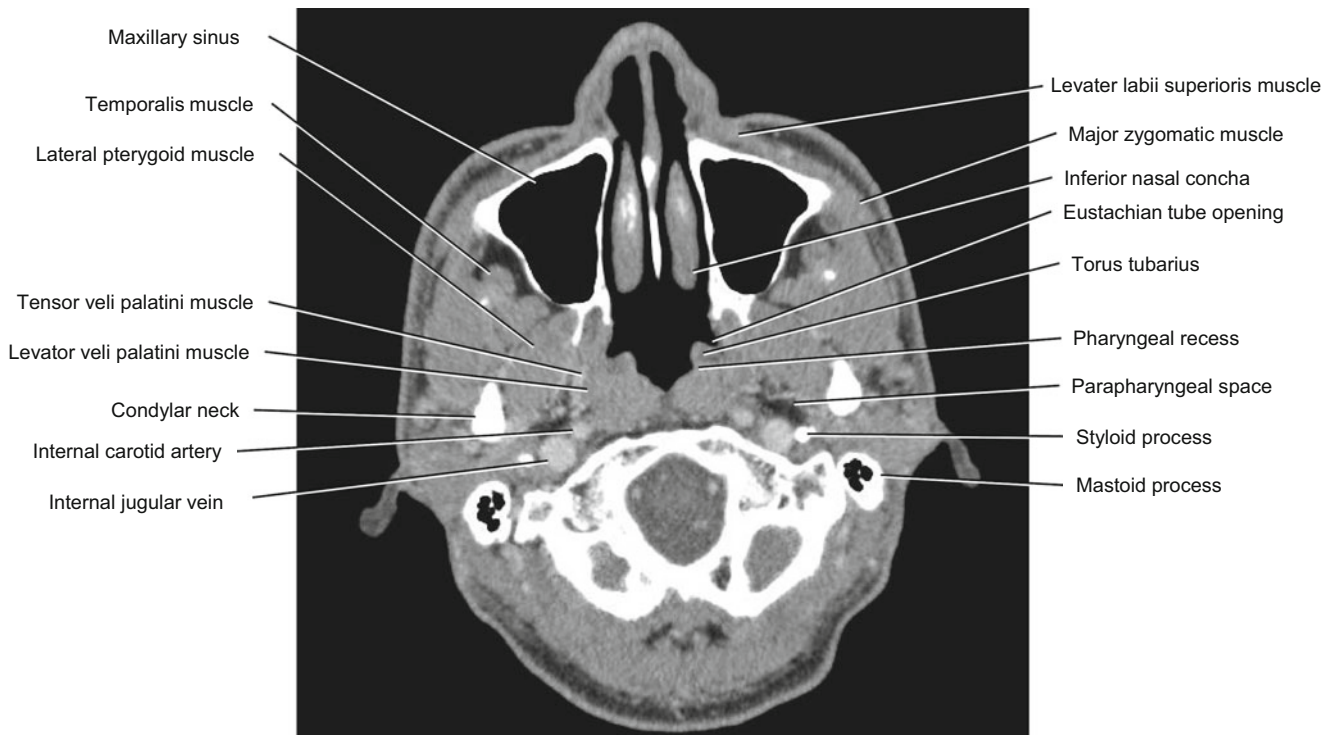


Fig. 5.21 Axial CECT



Fig. 5.22 Axial CECT

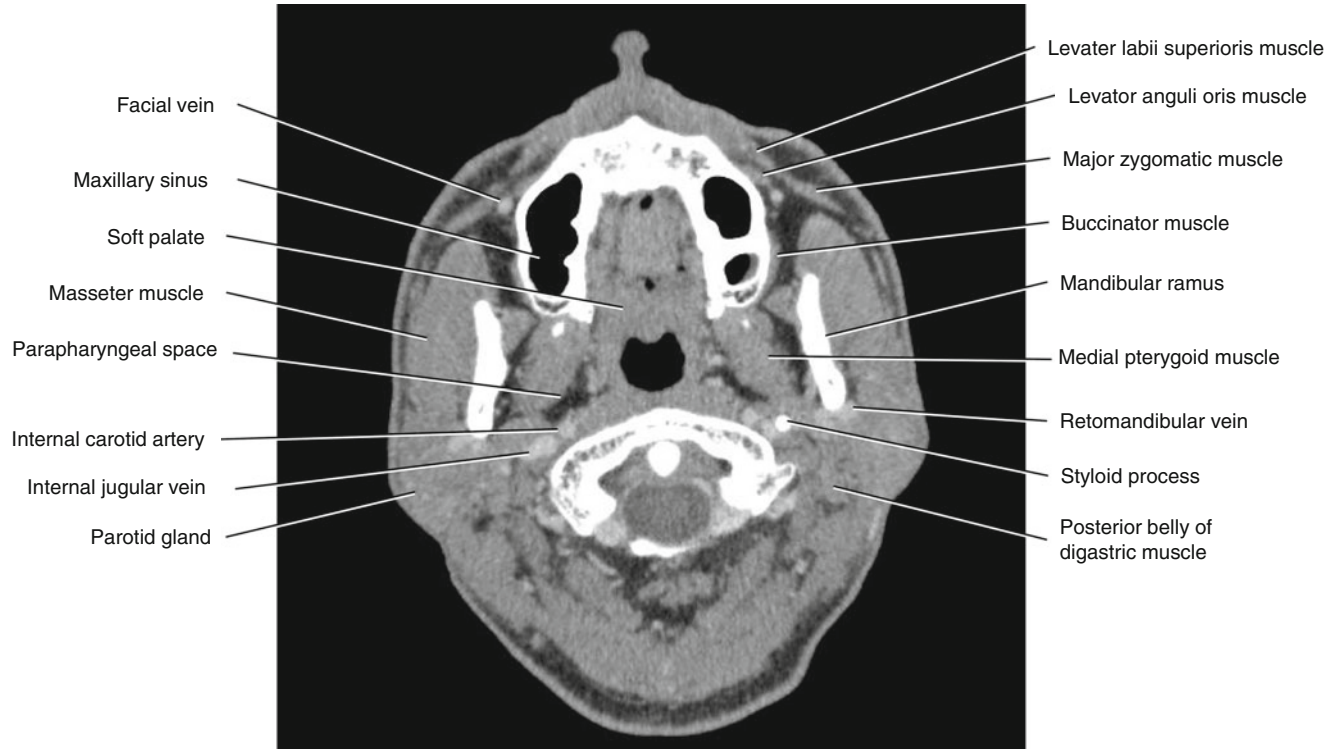


Fig. 5.23 Axial CECT

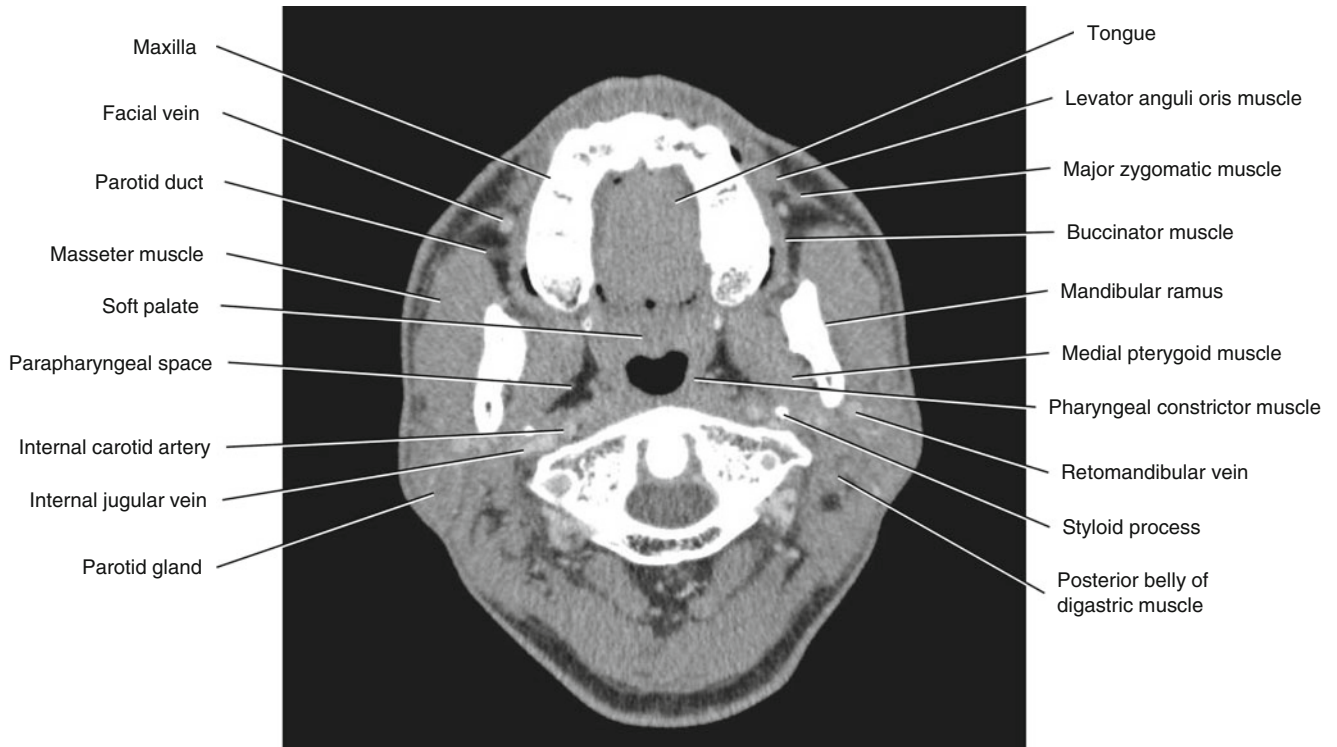


Fig. 5.24 Axial CECT

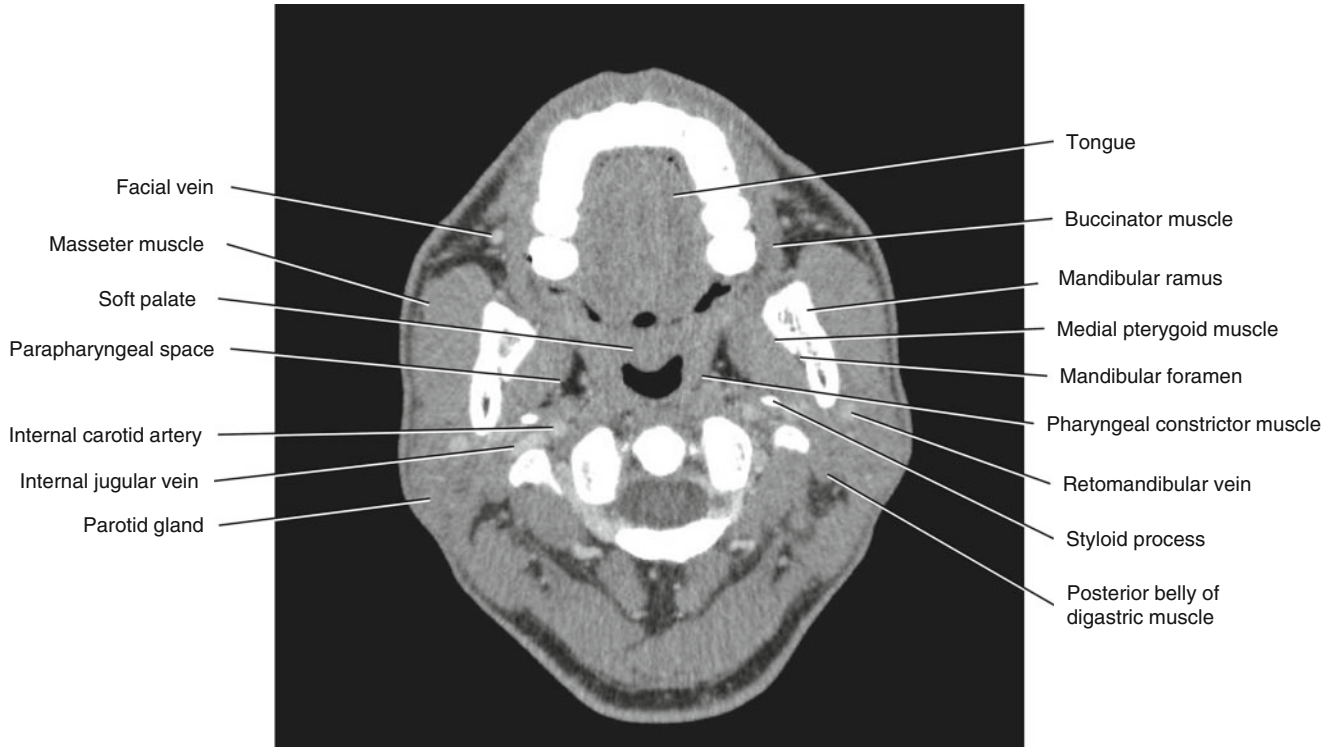


Fig. 5.25 Axial CECT

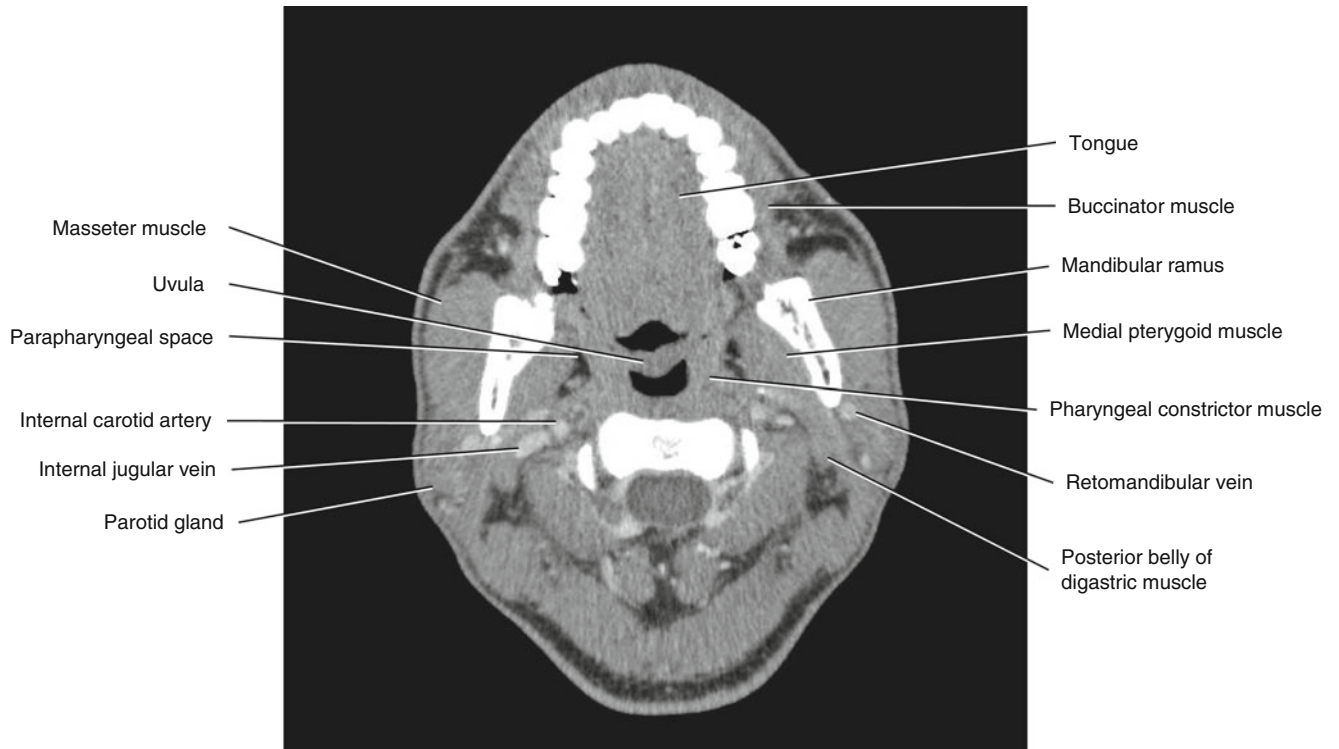


Fig. 5.26 Axial CECT

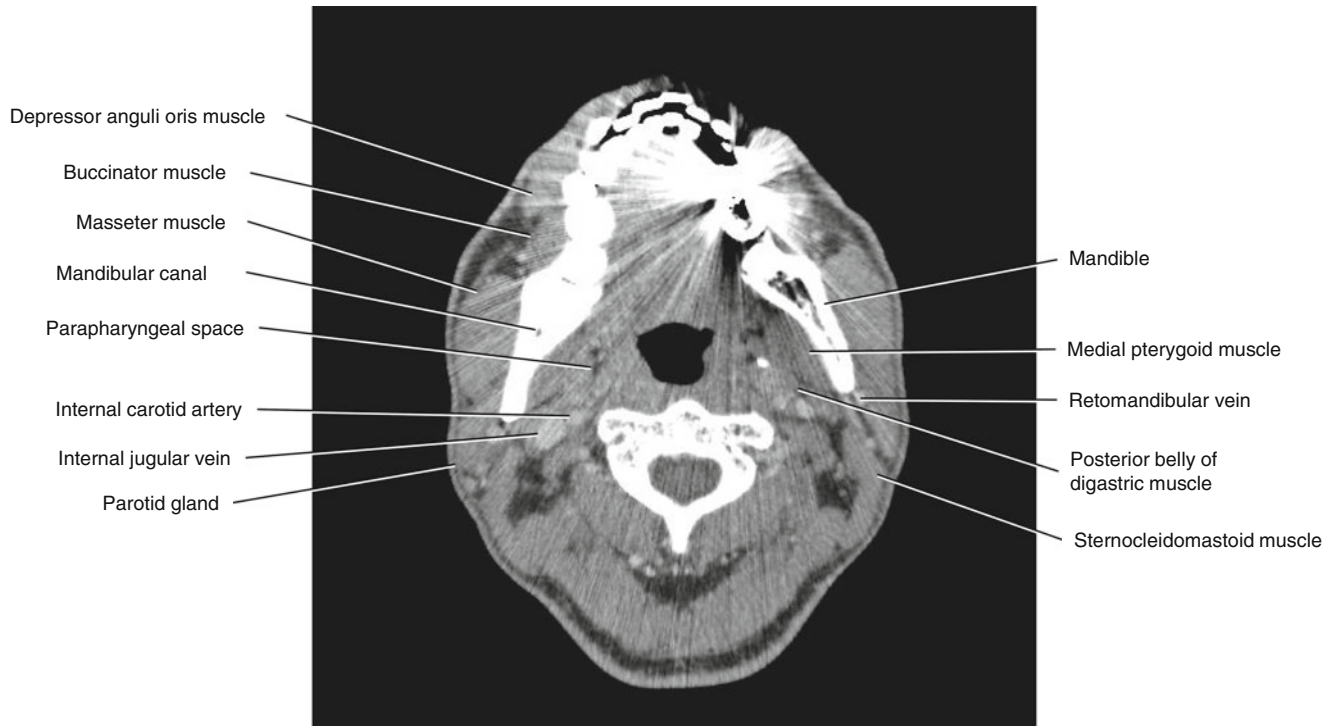


Fig. 5.27 Axial CECT

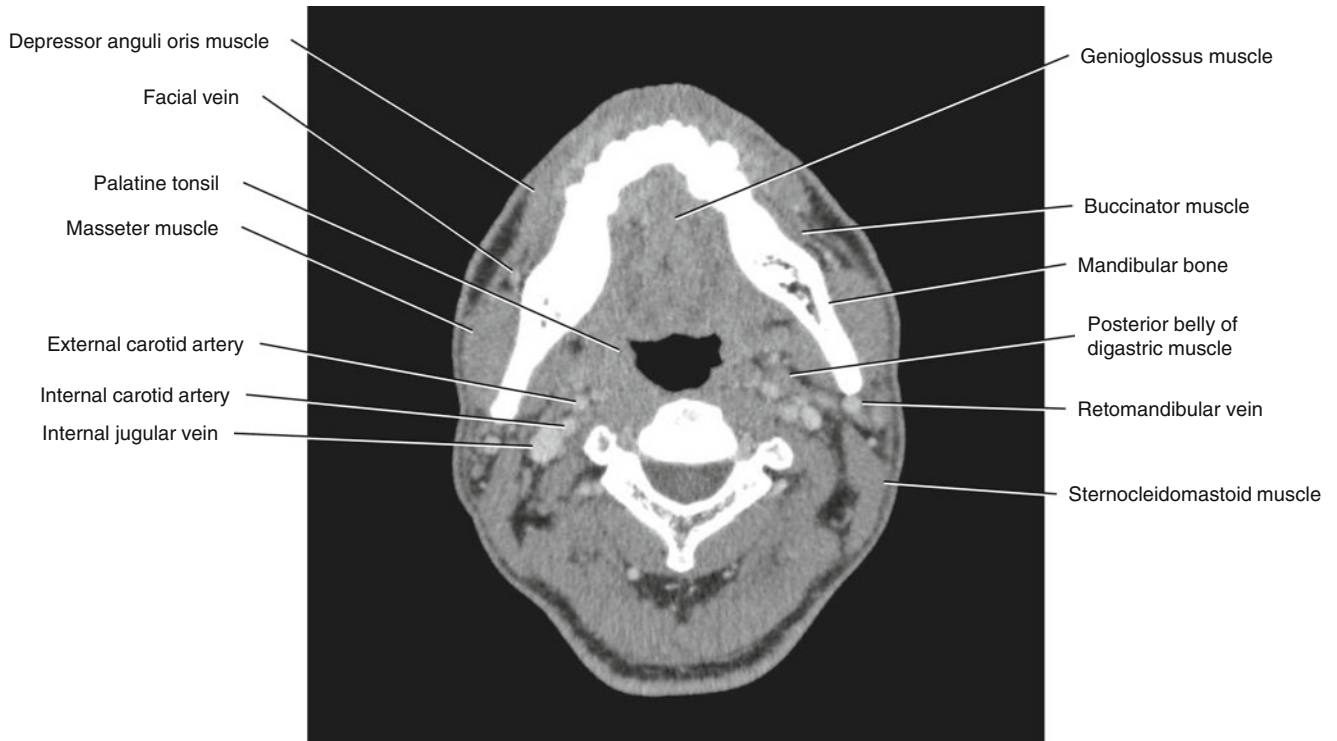


Fig. 5.28 Axial CECT

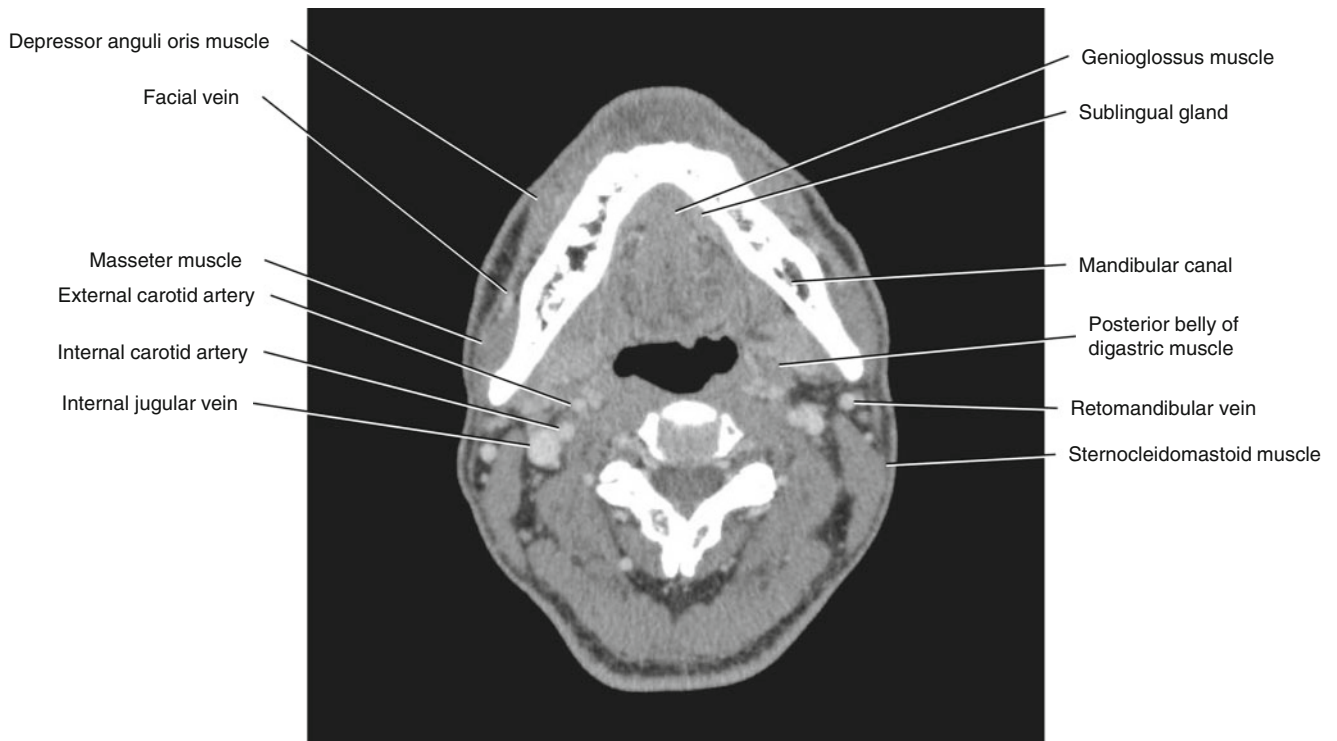


Fig. 5.29 Axial CECT

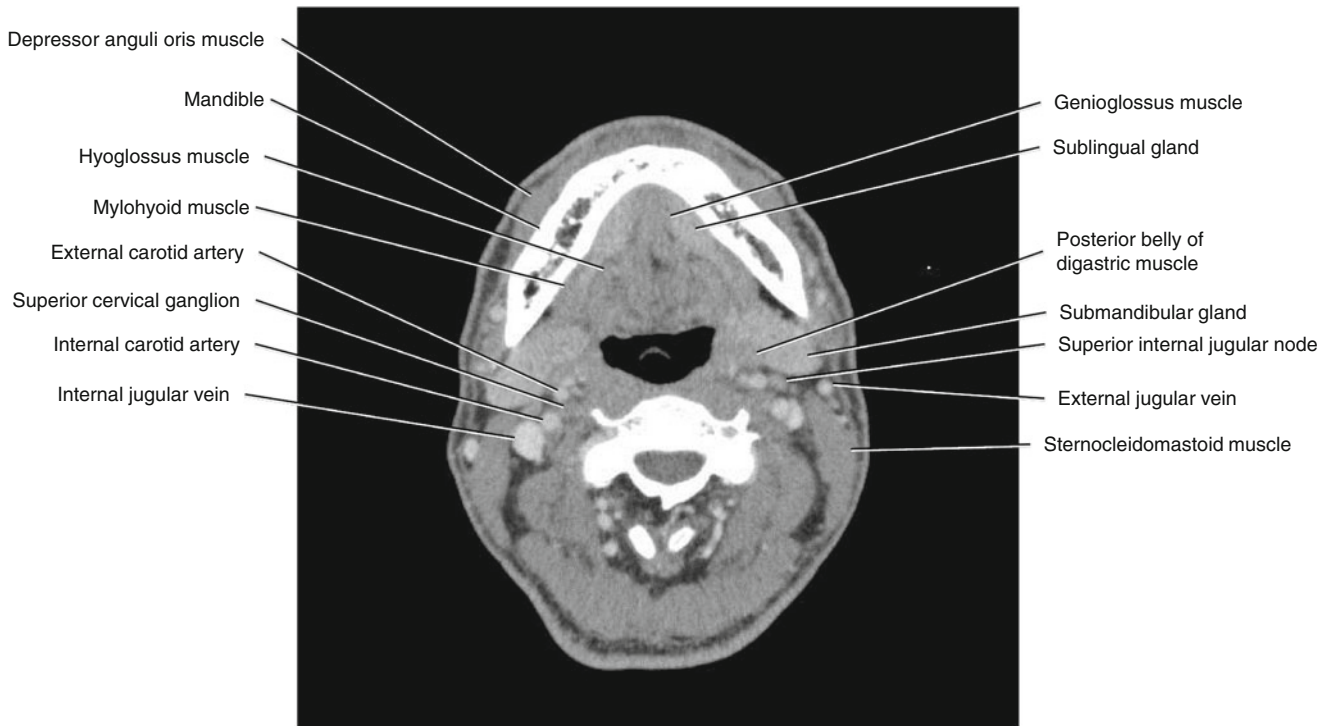


Fig. 5.30 Axial CECT

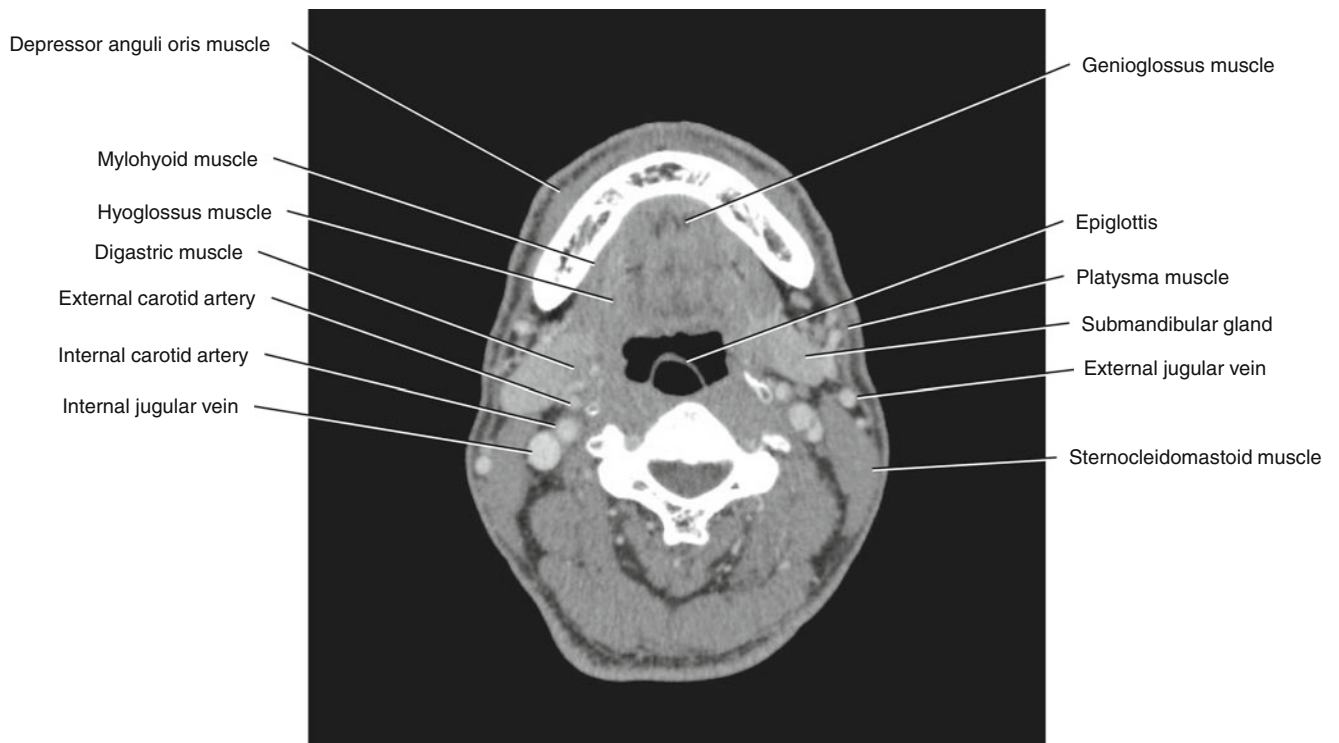


Fig. 5.31 Axial CECT

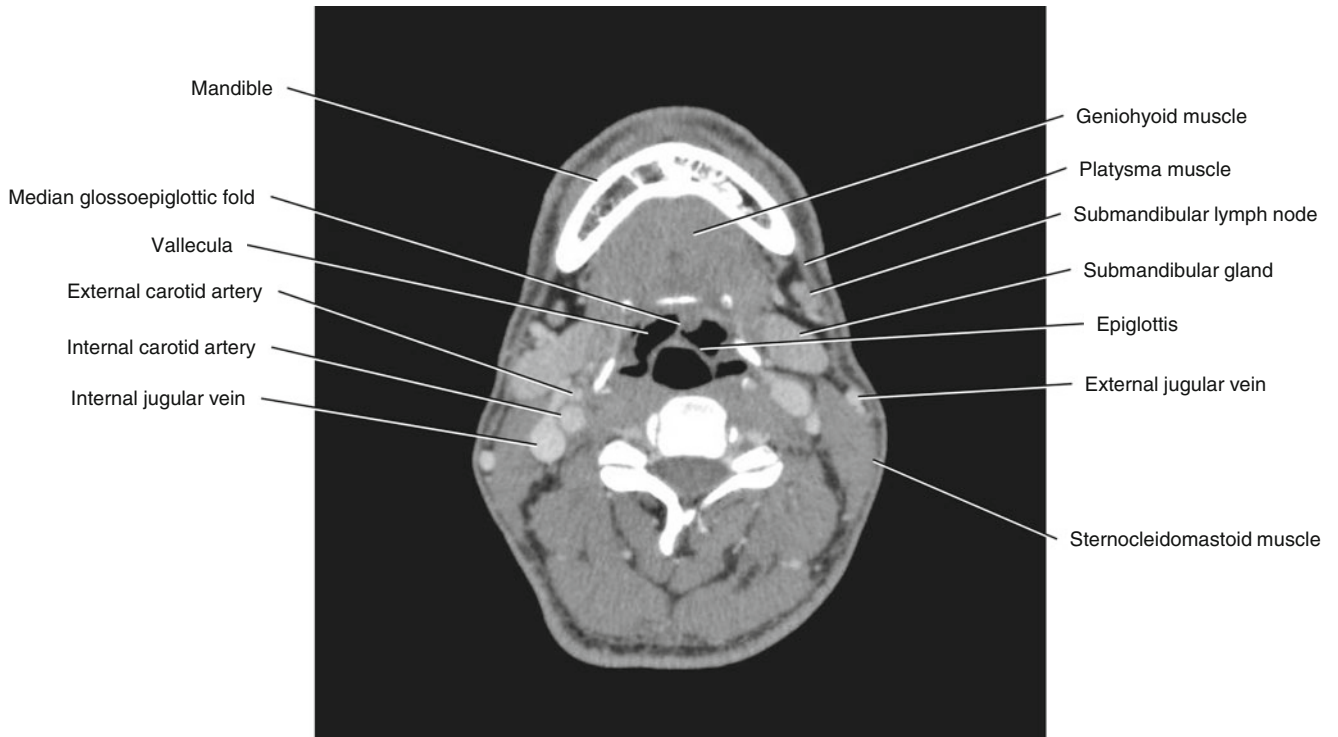


Fig. 5.32 Axial CECT

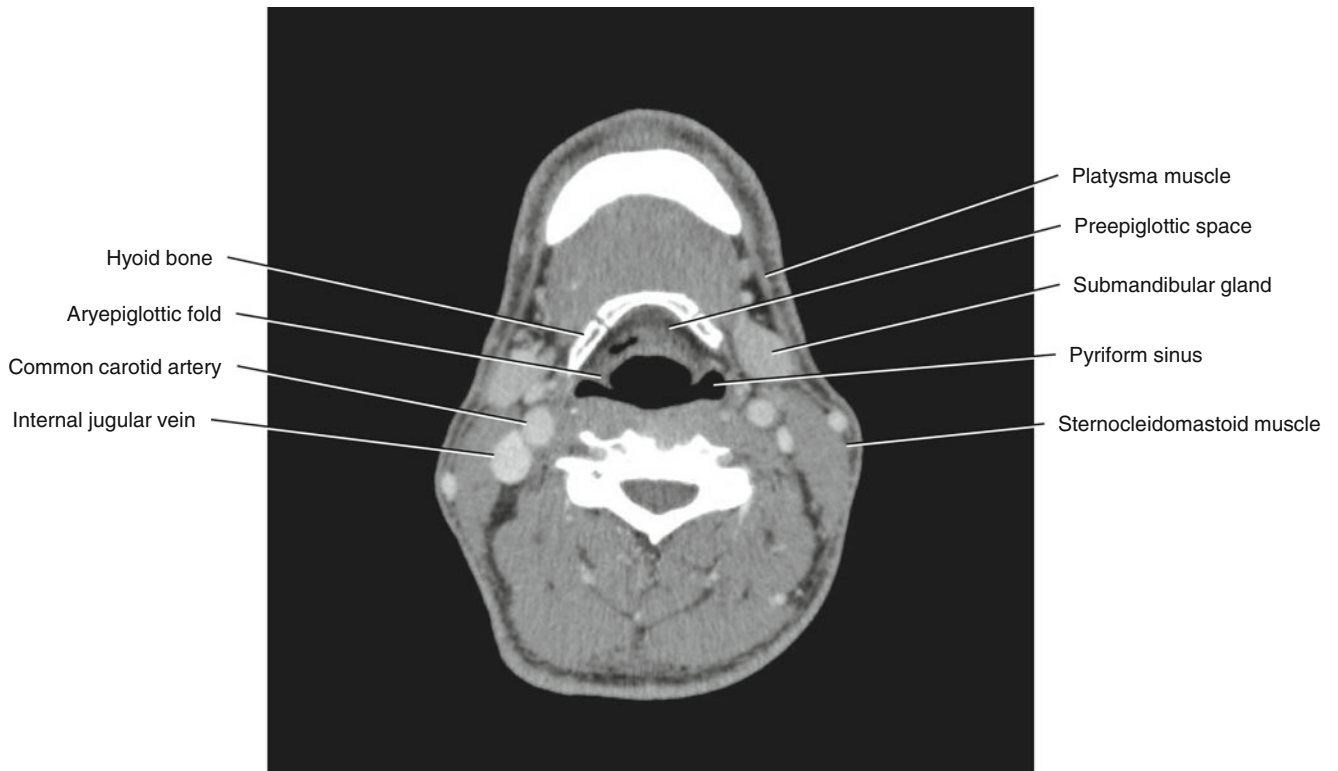


Fig. 5.33 Axial CECT

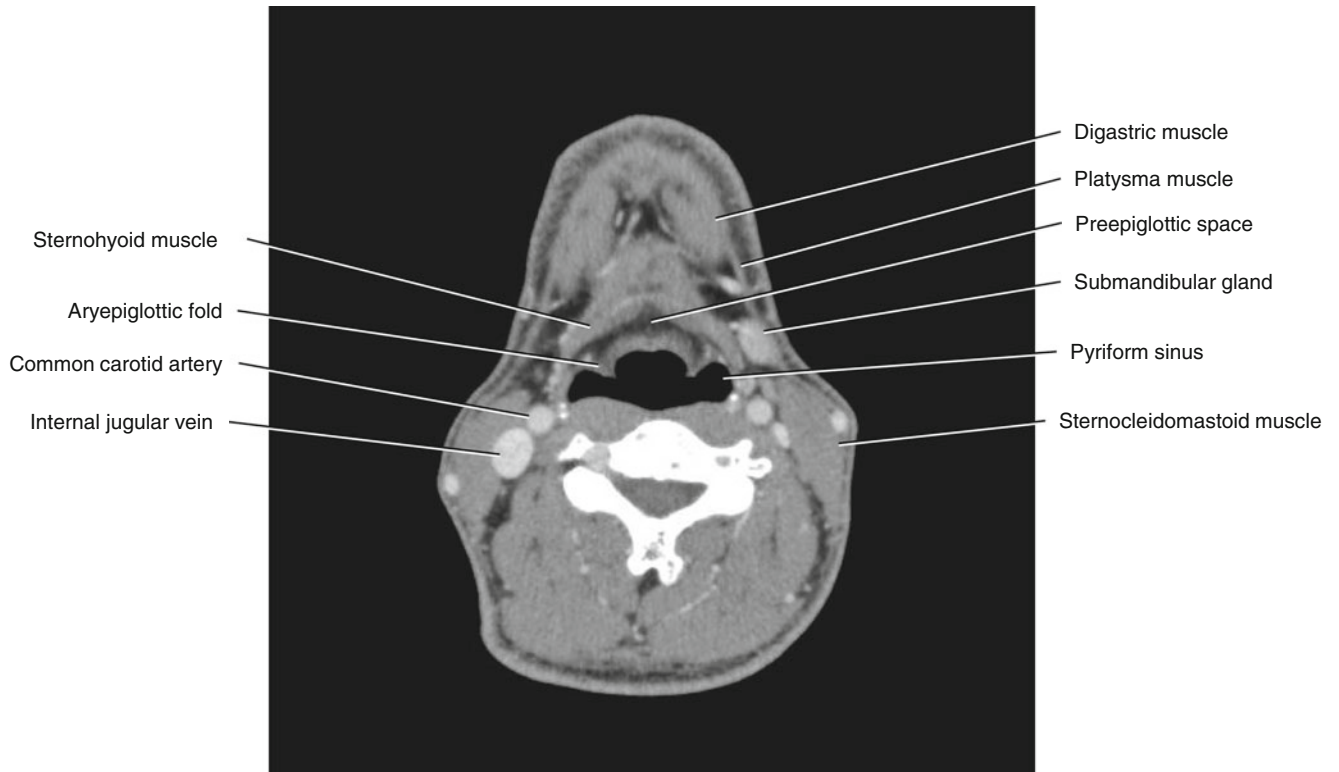


Fig. 5.34 Axial CECT

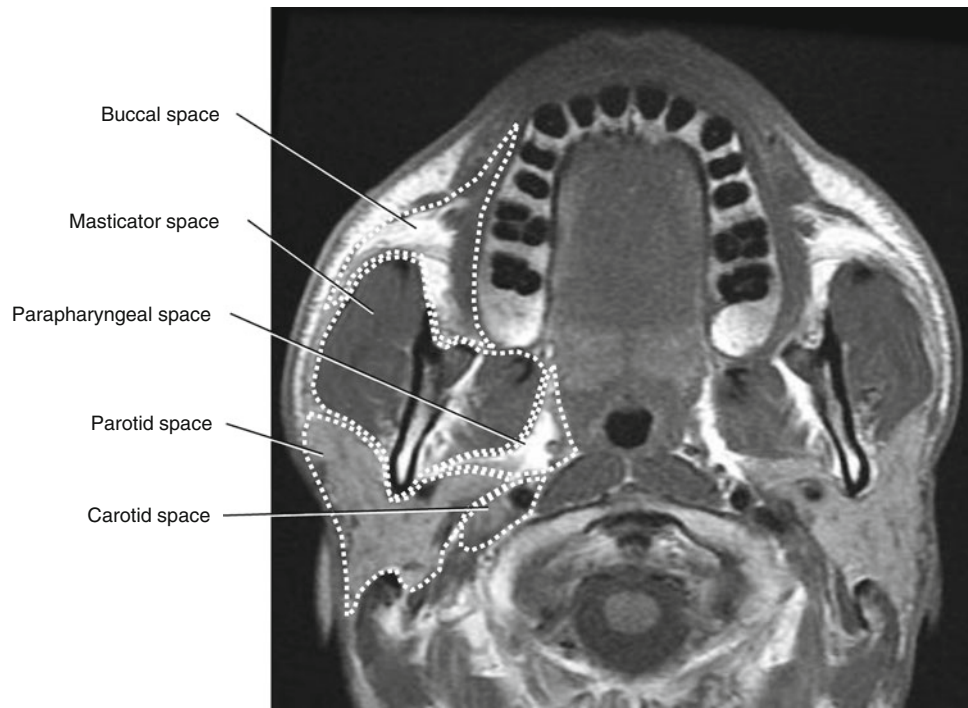


Fig. 5.35 Axial T1-weighted MRI at the level of the maxillary alveolar process

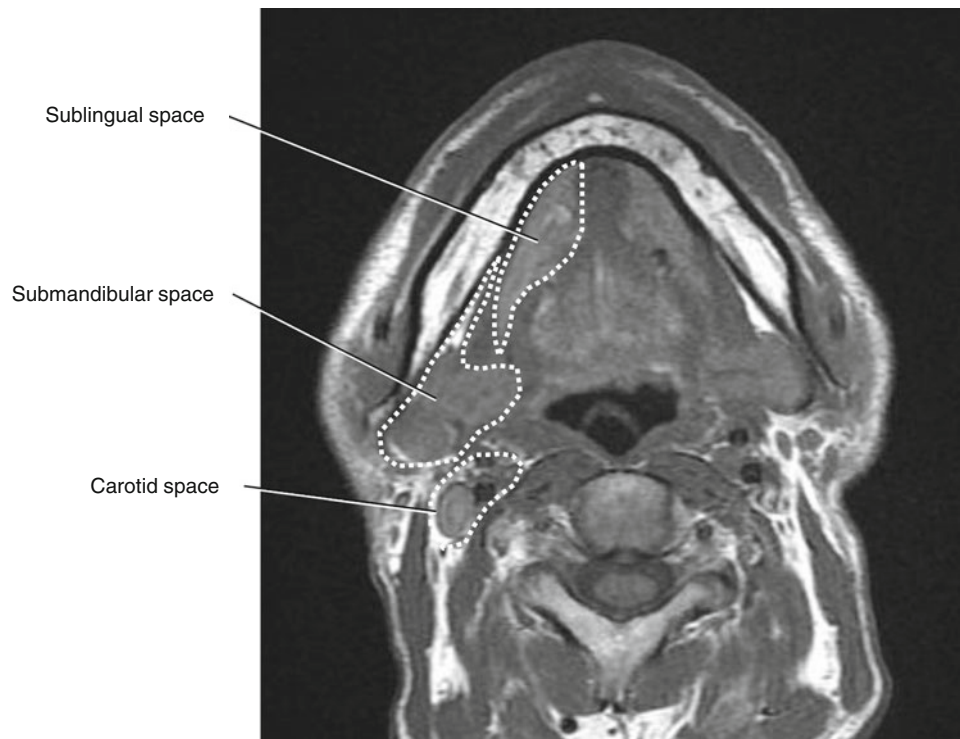


Fig. 5.36 Axial T1-weighted MRI at the level of the mental foramen

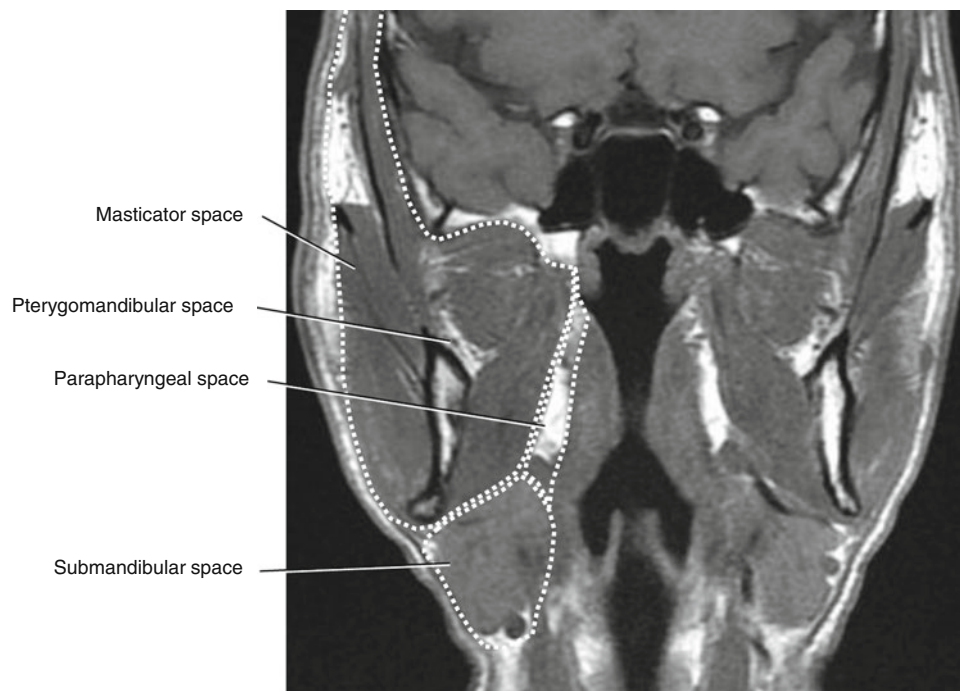


Fig. 5.37 Coronal T1-weighted MRI of the pharyngeal airway

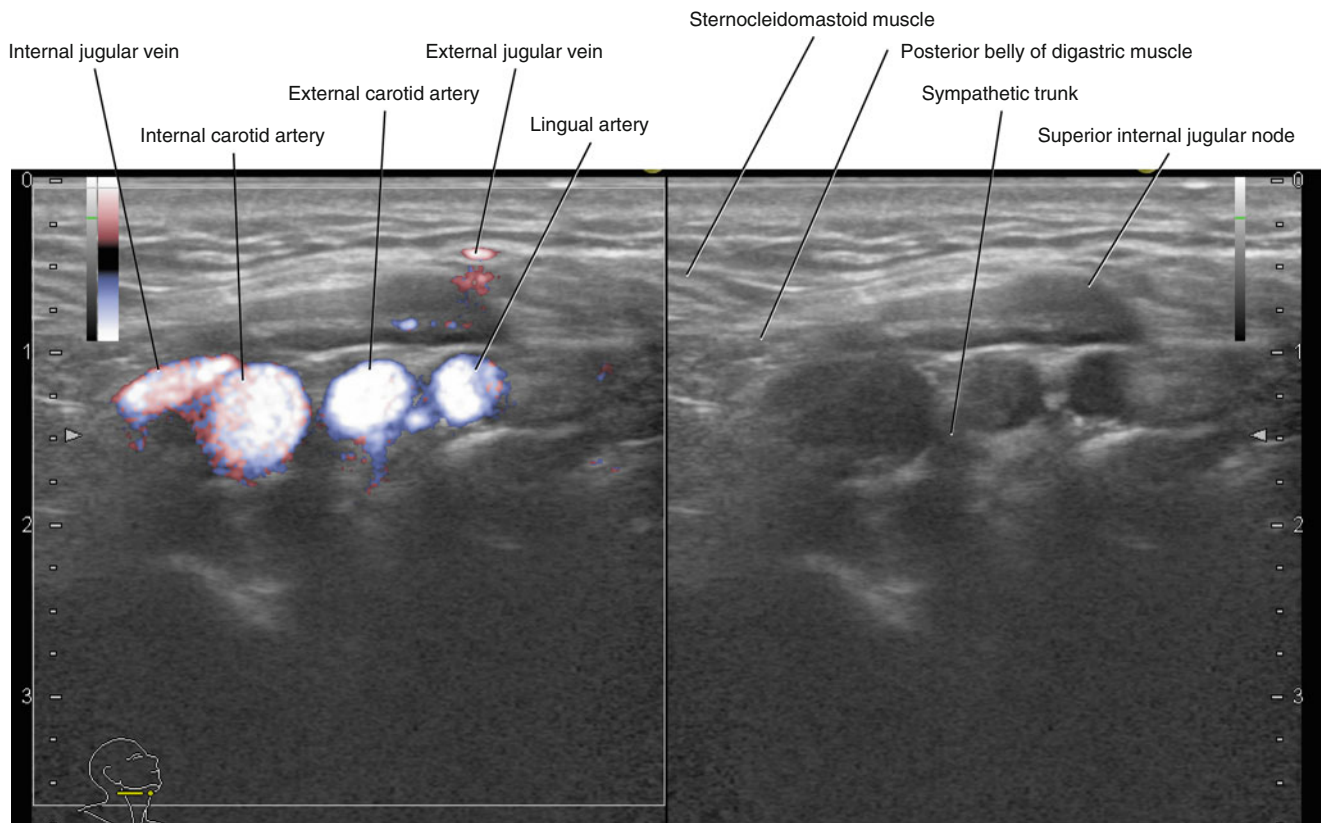


Fig. 5.38 Transverse neck US, right superior internal jugular node (left, fine flow Doppler; right, B-mode)

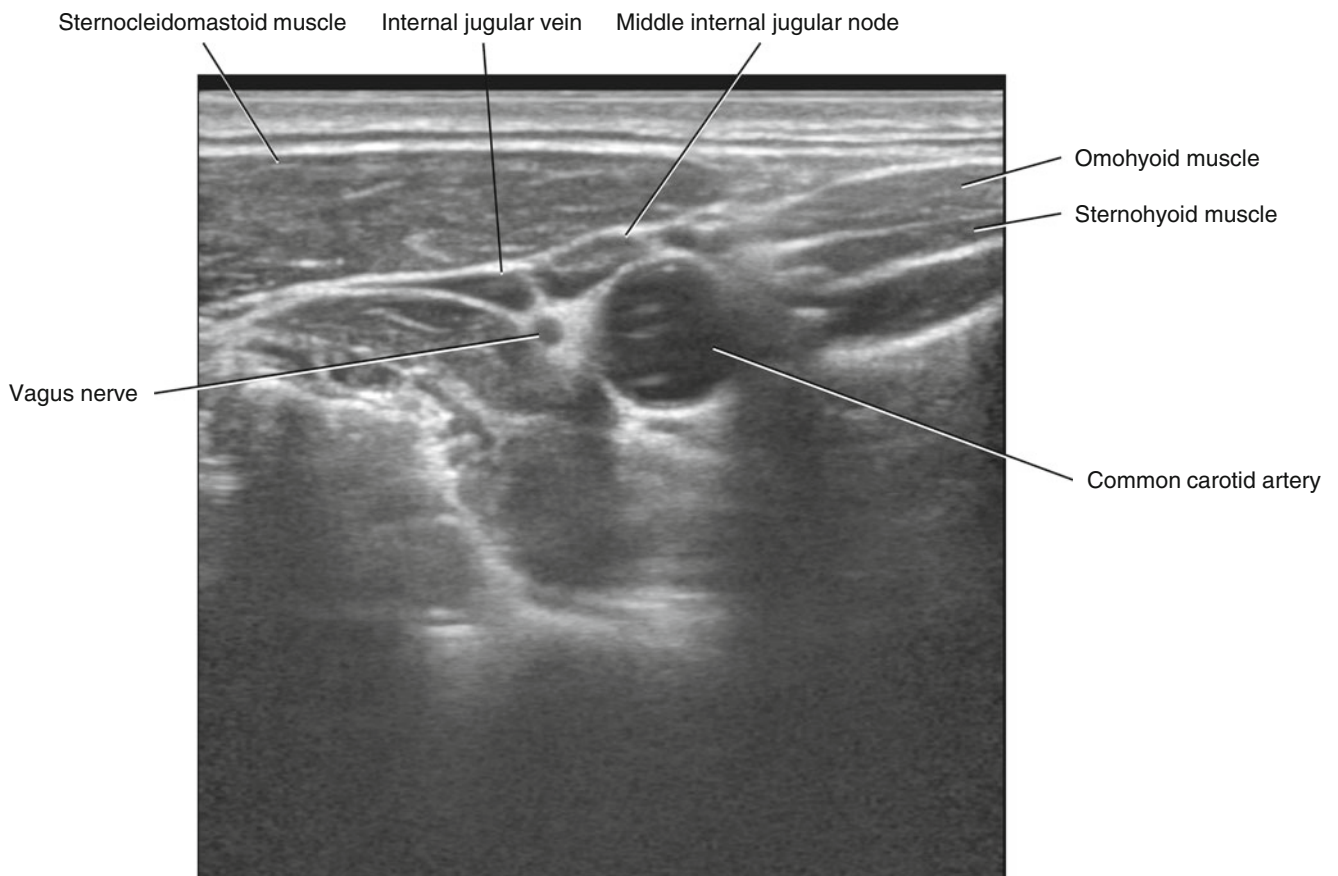


Fig. 5.39 Transverse neck US, right middle internal jugular node

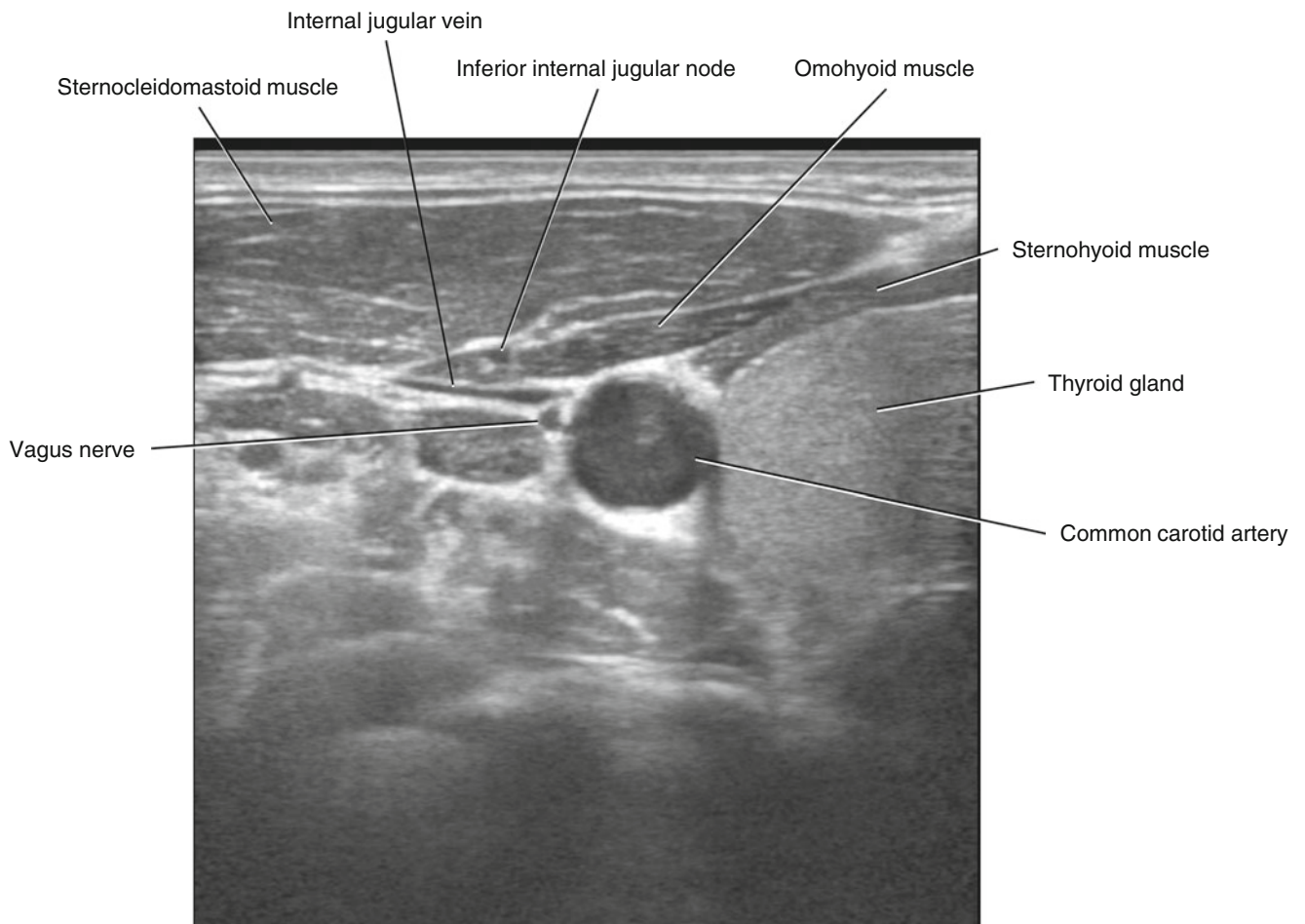


Fig. 5.40 Transverse neck US, right inferior internal jugular node

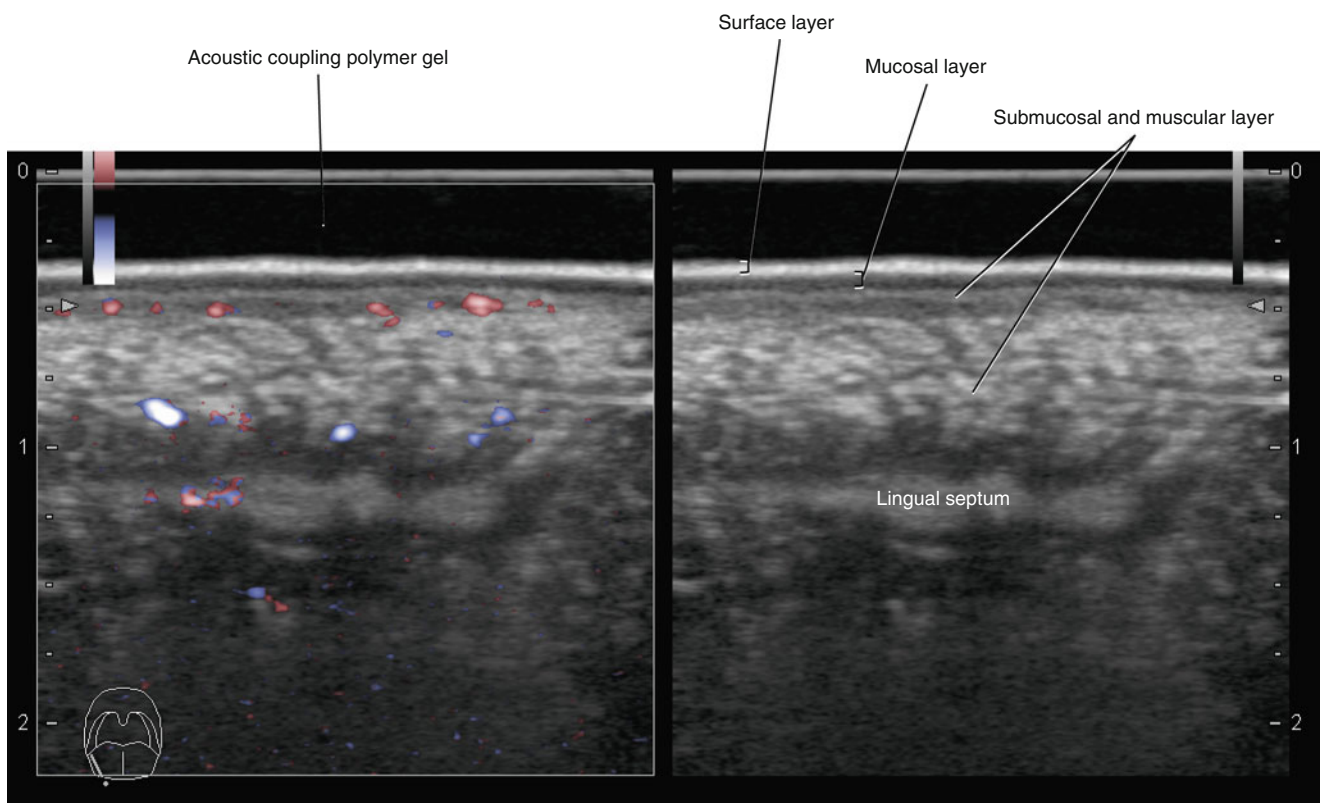


Fig. 5.41 Transverse intraoral US, right lateral margin of the tongue (left, fine flow Doppler; right, B-mode)



Fig. 5.42 Axial CECT of the right normal submandibular lymph node

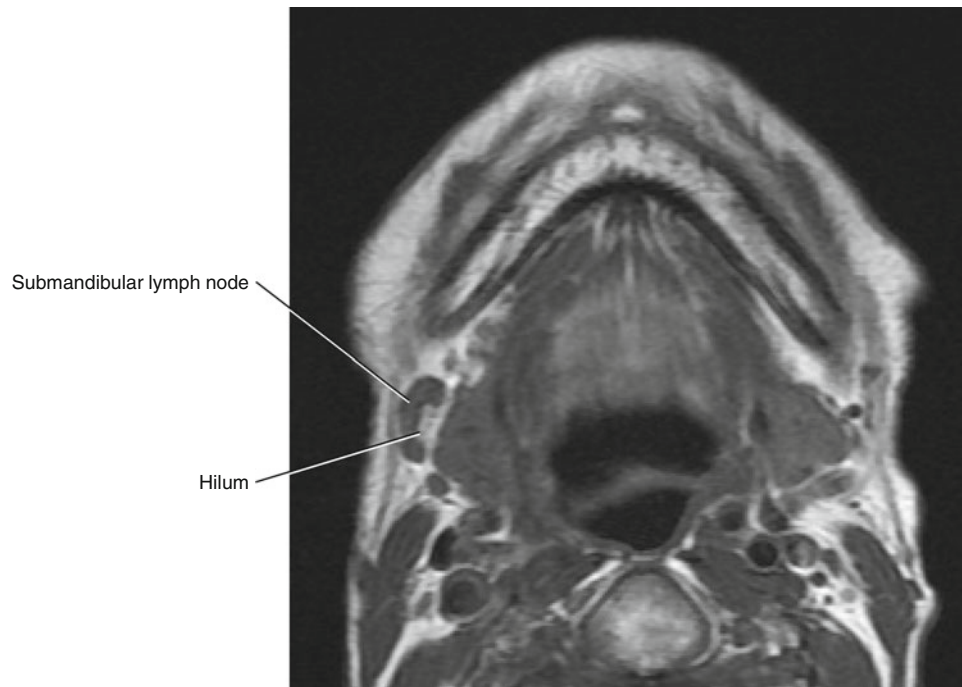


Fig. 5.43 Axial T1-weighted MRI of the right normal submandibular lymph node

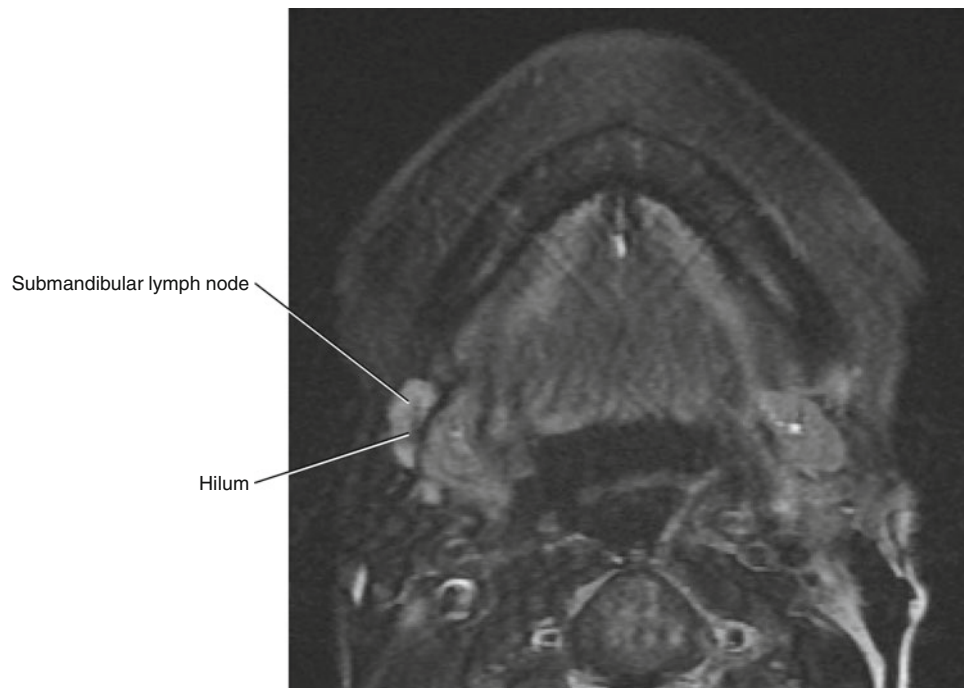


Fig. 5.44 Axial fat-saturated T2-weighted MRI of the right normal submandibular lymph node

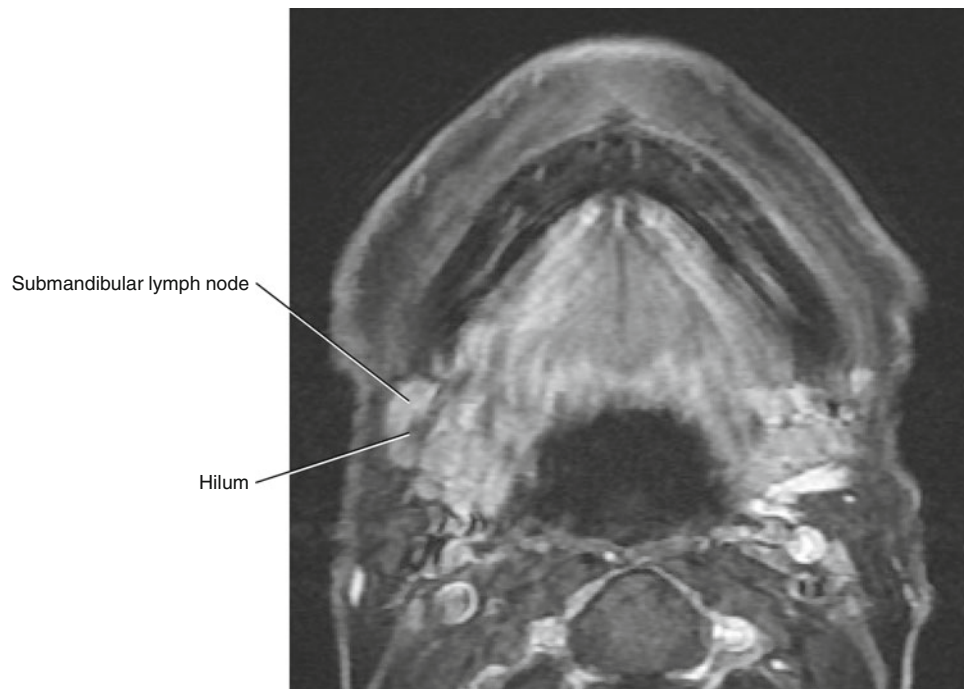


Fig. 5.45 Axial post-contrast fat-saturated T1-weighted MRI of the right normal submandibular lymph node

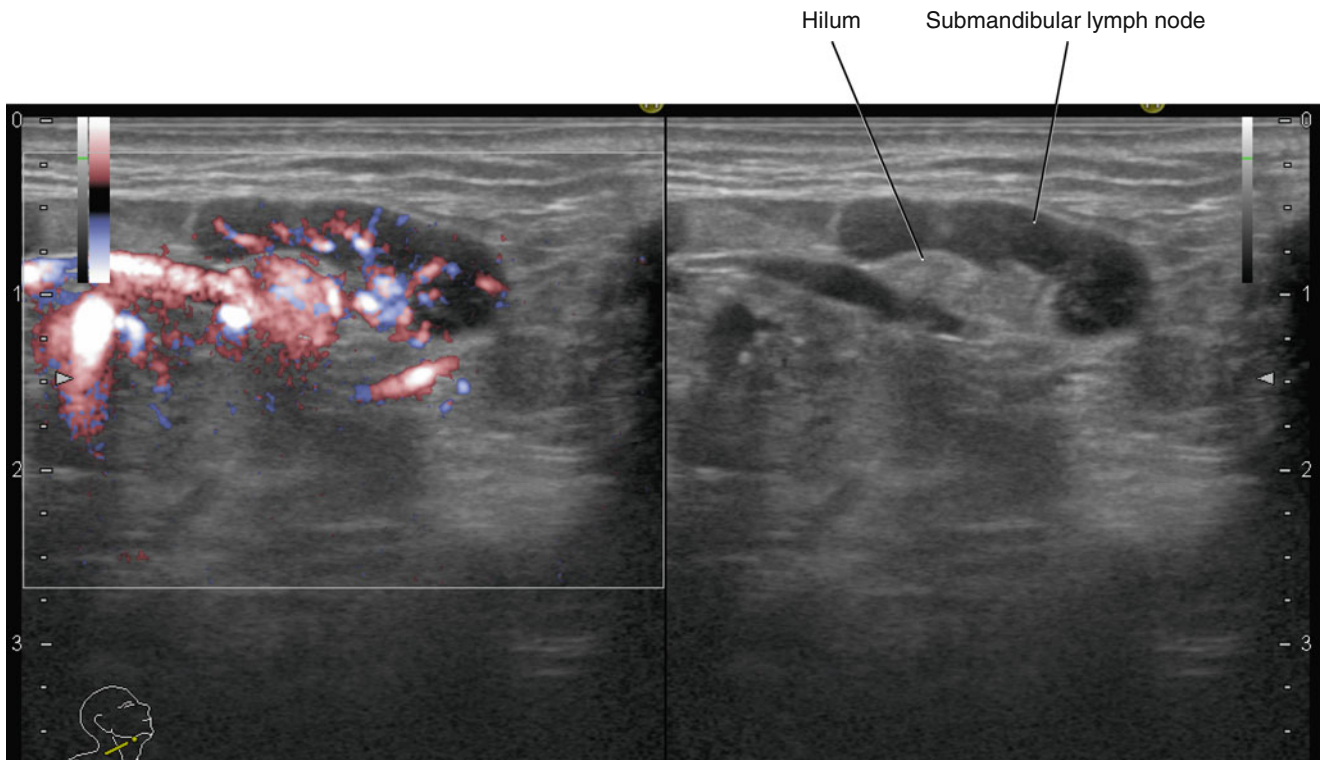


Fig. 5.46 Sagittal ultrasonography of the right normal submandibular lymph node (left, fine flow Doppler; right, B-mode)

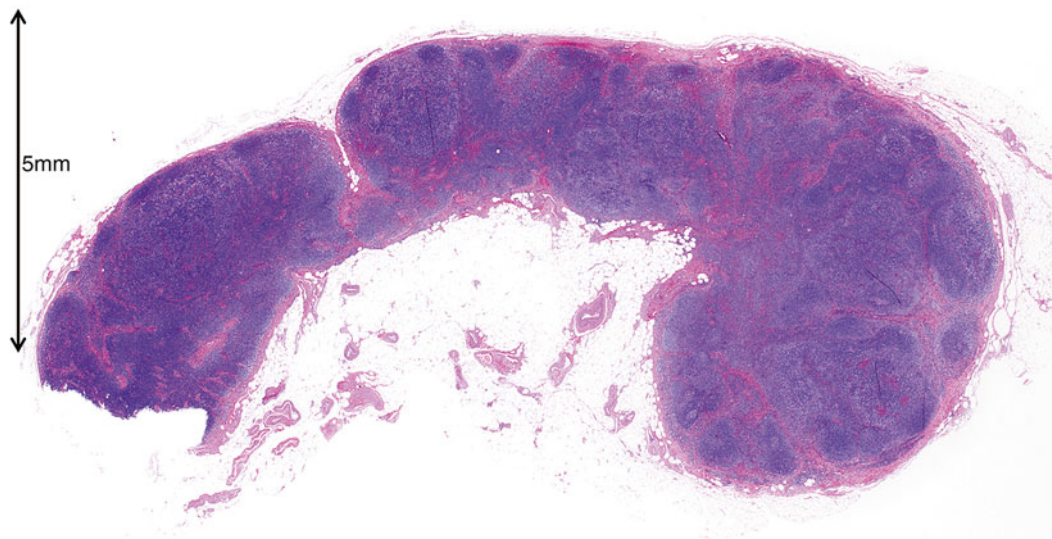


Fig. 5.47 Photomicrograph of histopathological specimen of the right normal submandibular lymph node (hematoxylin-eosin stain)

T3 Tumor more than 4 cm in greatest dimension
 T4a Moderately advanced local disease; tumor invades adjacent structures

(according to the 2012 General Rules for Clinical and Pathological Studies on Oral Cancer by the Scientific Committee of Japan Society for Oral Tumors [5]):

1. Tongue: invasion into the mandibular bone marrow, invasion into the submandibular space, and invasion into the extrinsic muscles of the tongue
2. Upper gingiva: invasion into the maxillary sinus and nasal cavity and invasion into the buccal space or subcutaneous fat
3. Lower gingiva: invasion reaching the mandibular canal, invasion into the buccal space or subcutaneous fat, invasion into the submandibular space, and invasion into the extrinsic muscles of the tongue
4. Buccal mucosa: invasion into the subcutaneous fat, invasion into the maxillary and mandibular bone marrow, and invasion into the maxillary sinus
5. Floor of the mouth: invasion into the mandibular bone marrow, invasion into the submandibular space, and invasion into the extrinsic muscles of the tongue
6. Hard palate: invasion into the maxillary sinus and nasal cavity

T4b Very advanced local disease; tumor invasion into the masticator space, invasion into the pterygoid plate, invasion into the skull base, and invasion circumferentially surrounding the internal carotid artery

5.3.3 Regional Lymph Nodes (N)

The classification and range of cervical lymph nodes are the same as described in the Rules Regarding Lymph Nodes by the Japan Society of Clinical Oncology (JSCO), and lymph node metastasis is evaluated according to the UICC classification. Internationally, the level classification system by the Academy's Committee for Head and Neck Surgery and Oncology (ACHNSO) based on the area of neck dissection is widely used, and the AAO-HNS classification, a fragmented version of the ACHNSO classification, has also been proposed [5].

N factor

- NX Regional lymph nodes cannot be assessed
 N0 No regional lymph node metastasis
 N1 Metastasis in a single ipsilateral lymph node, 3 cm or less in greatest diameter

N2 Metastasis in a single ipsilateral lymph node, more than 3 cm but not more than 6 cm in greatest dimension; or in multiple ipsilateral lymph nodes, none more than 6 cm in greatest dimension; or in bilateral or contralateral lymph nodes, none more than 6 cm in greatest dimension

N2a Metastasis in a single ipsilateral lymph node, more than 3 cm but not more than 6 cm in greatest dimension

N2b Metastasis in multiple ipsilateral lymph nodes, none more than 6 cm in greatest dimension

N2c Metastasis in bilateral or contralateral lymph nodes, none more than 6 cm in greatest dimension

N3 Metastasis in a lymph node, more than 6 cm in greatest dimension

5.3.4 Distant Metastasis (M)

M Factor

M0 No distant metastasis

M1 Distant metastasis present

Staging

0 Tis, N0, M0

I T1, N0, M0

II T2, N0, M0

III T3, N0, M0

T1, T2 or T3, N1, M0

IVA T4a, N0 or N1, M0

T1, T2, T3 or T4a, N2, M0

IVB Any T, N3, M0

T4a and any N, M0

IVC Any T and any N M1

Level Classification (Fig. 5.48)

Level IA Submental lymph nodes; they lie between medial margins of the anterior bellies of the digastric muscles.

Level IB Submandibular lymph nodes; on each side, they lie lateral to the level IA nodes and anterior to the back of each submandibular gland.

Level IIA Superior internal jugular lymph nodes, superior deep cervical lymph nodes (jugulodigastric nodes, anterior); they lie either anterior, medial, lateral, or posterior to the internal jugular vein. If posterior to the vein, the node is inseparable from the vein.

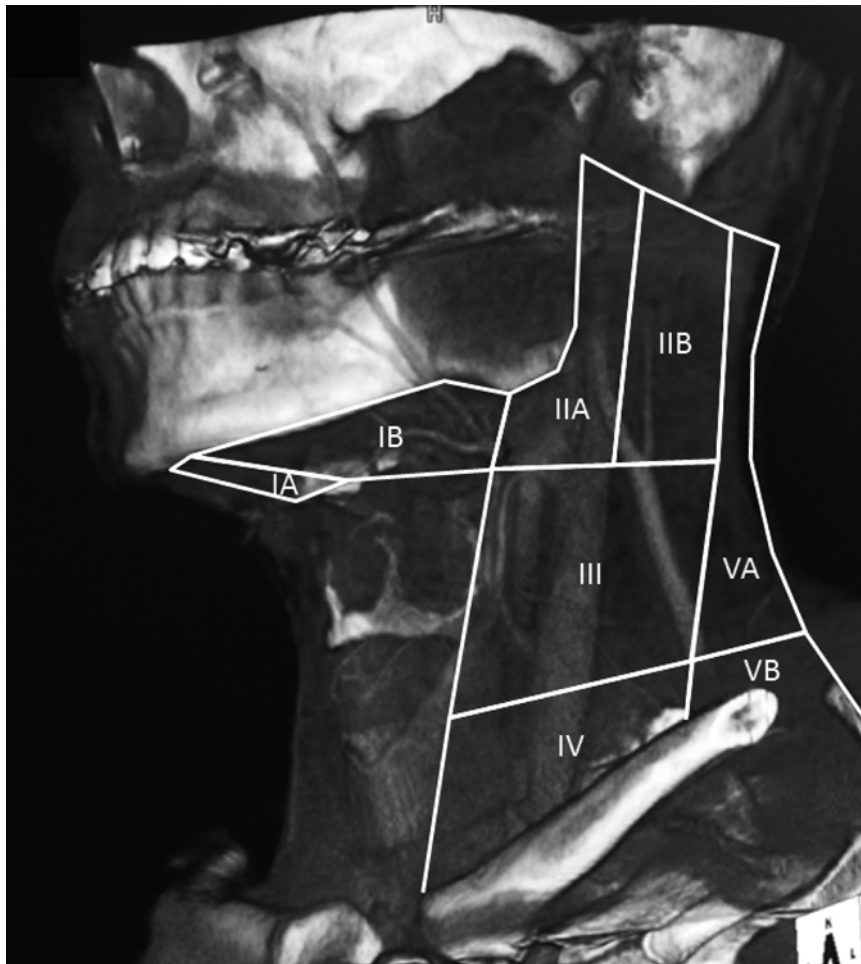


Fig. 5.48 Level classification

- | | |
|--|--|
| <p>Level IIB Superior internal jugular lymph nodes, superior deep cervical lymph nodes (jugulodigastric nodes, posterior); they lie posterior to the internal jugular vein and have a fat plane separating it from the vein.</p> | <p>Level VA Spinal accessory lymph nodes; they extend from the skull base to the level of the bottom of the cricoid arch.</p> |
| <p>Level III Middle internal jugular lymph nodes, middle deep cervical lymph nodes (jugulo-omohyoid nodes); they extend from the level of the bottom of the body of the hyoid bone to the level of the bottom of the cricoid arch. They lie anterior to the back of the sternocleidomastoid muscle.</p> | <p>Level VB Supraclavicular lymph nodes; they extend from the level of the bottom of the cricoid arch to the level of the clavicle.</p> |
| <p>Level IV Inferior internal jugular lymph nodes, inferior deep cervical lymph nodes; they extend from the level of the bottom of the cricoid arch to the level of the clavicle.</p> | |

5.4 Oral Cavity Malignancies

5.4.1 Tongue Carcinoma [Squamous Cell Carcinoma (SCC)]

5.4.1.1 Case 1: 82-Year-Old Female, Left-Tongue SCC T4aN0 (Figs. 5.49, 5.50, 5.51, 5.52, 5.53, 5.54, 5.55, 5.56, 5.57, 5.58 and 5.59)



Fig. 5.49 Axial CECT. Tumor is demonstrated as an ill-defined enhancing mass at the left lateral margin of the tongue involving the floor of the mouth (*arrow*)

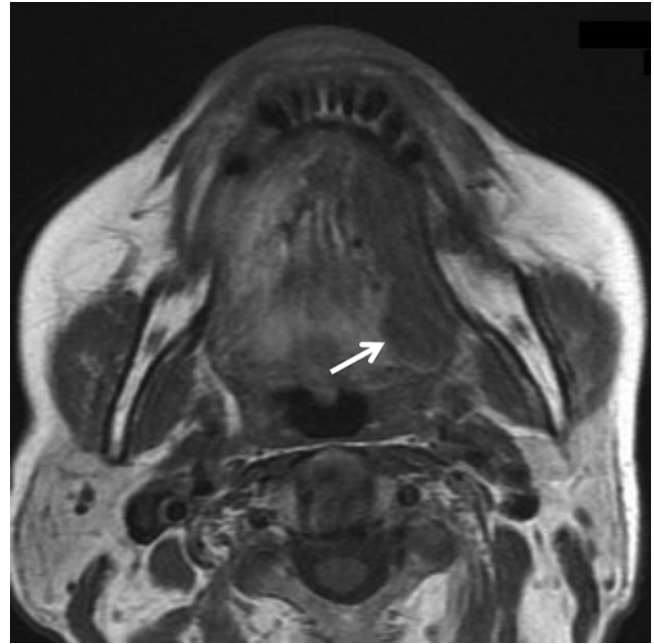


Fig. 5.51 Axial T1-weighted MRI. Tumor is demonstrated as an intermediate signal intensity area with an ill-defined margin (*arrow*)

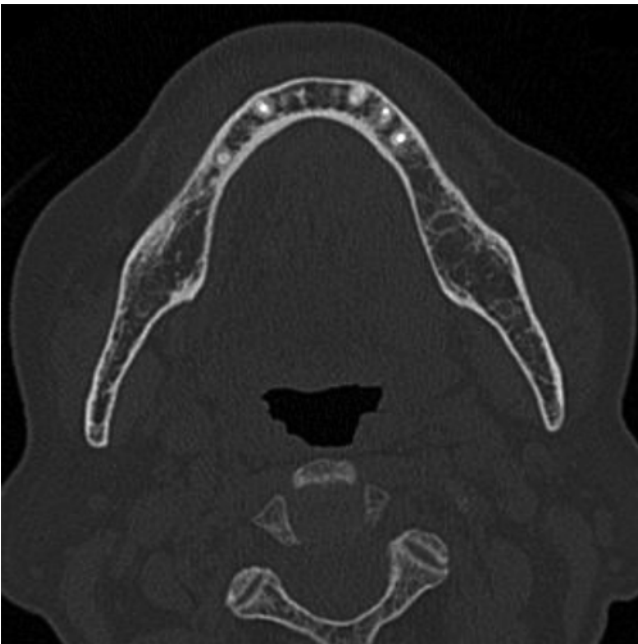


Fig. 5.50 Axial plain CT with bone window. No apparent destruction of adjacent bone cortex of the mandible is seen

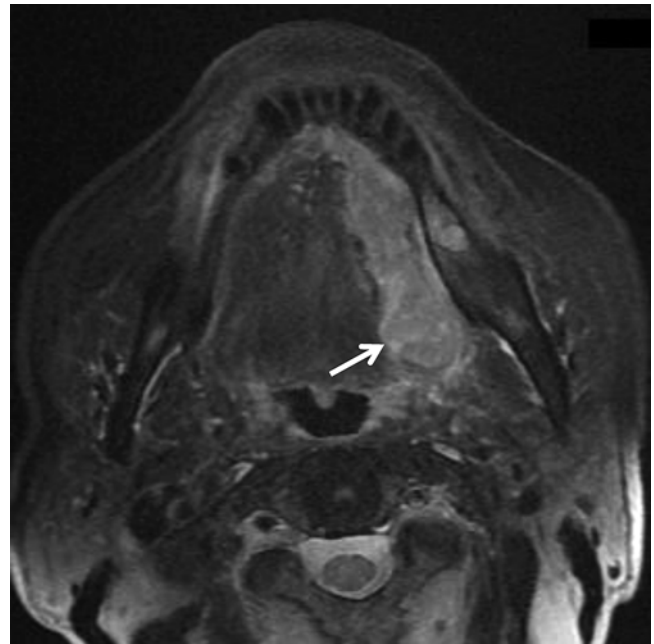


Fig. 5.52 Axial fat-saturated T2-weighted MRI. Tumor is demonstrated as relatively high heterogeneous intensity area with an ill-defined margin (*arrow*)

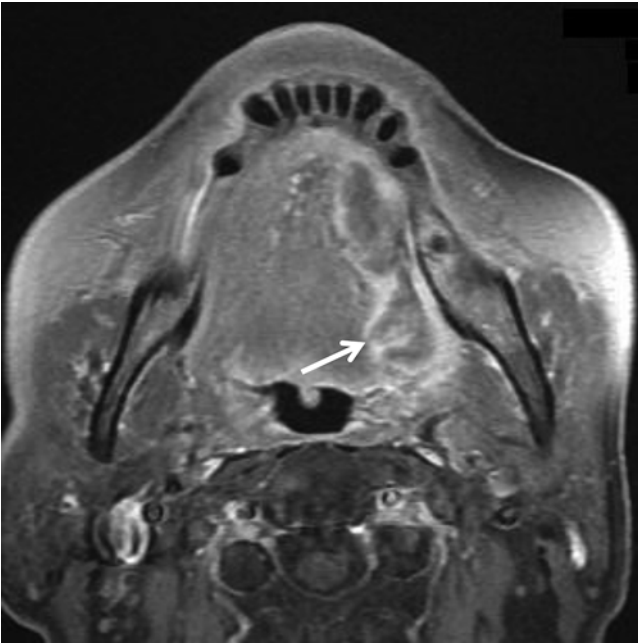


Fig. 5.53 Axial fat-saturated post-contrast T1-weighted MRI. Tumor enhances heterogeneously (*arrow*) and the peripheral portion of the tumor enhances prominently

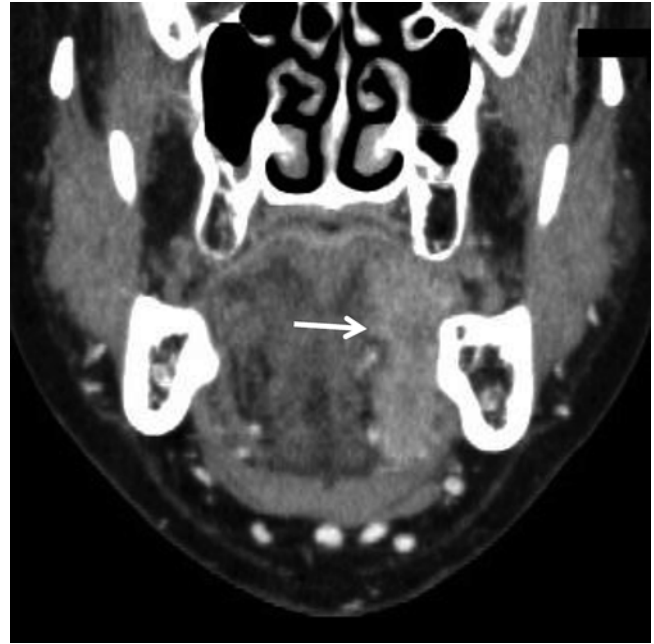


Fig. 5.55 Coronal CECT. Tumor (*arrow*) involves the left sublingual space and the hyoglossus muscle

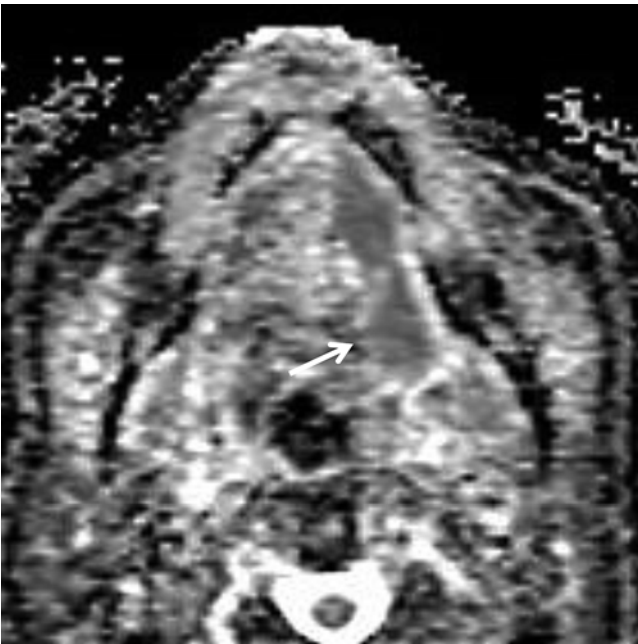


Fig. 5.54 Axial ADC map MRI. Tumor is demonstrated as a restricted diffusion area (*arrow*)

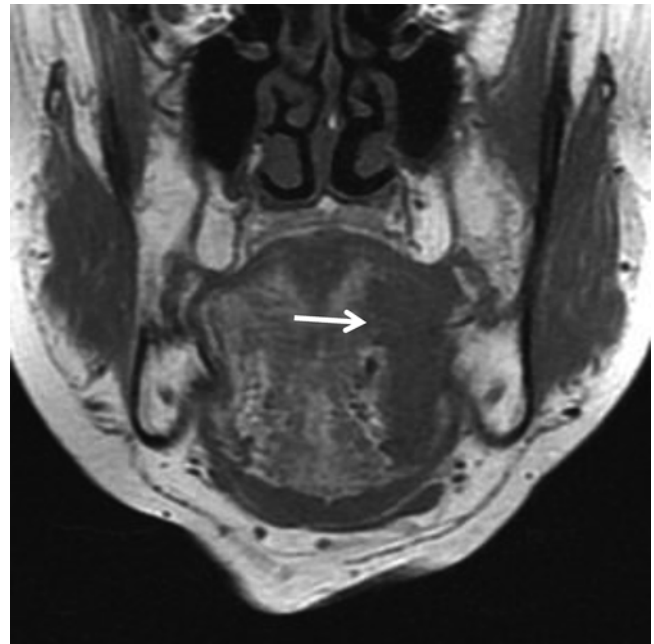


Fig. 5.56 Coronal T1-weighted MRI. Tumor is demonstrated as intermediate signal intensity (*arrow*)

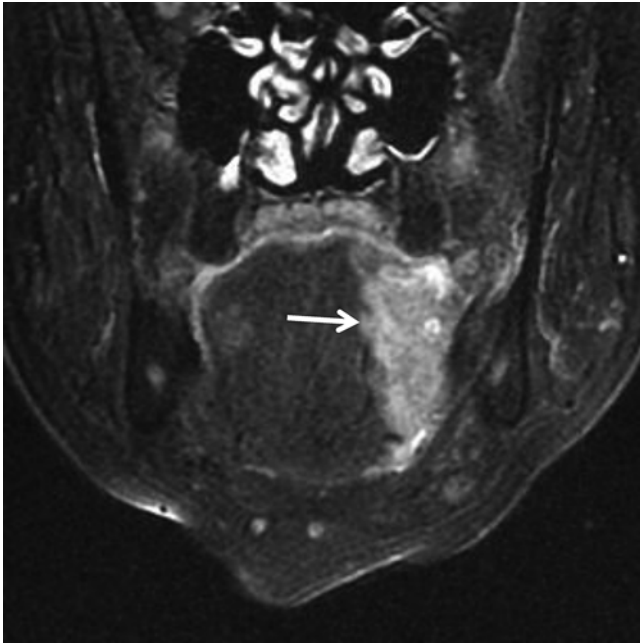


Fig. 5.57 Coronal fat-saturated T2-weighted MRI. Tumor is demonstrated as relatively high heterogeneous intensity (*arrow*)

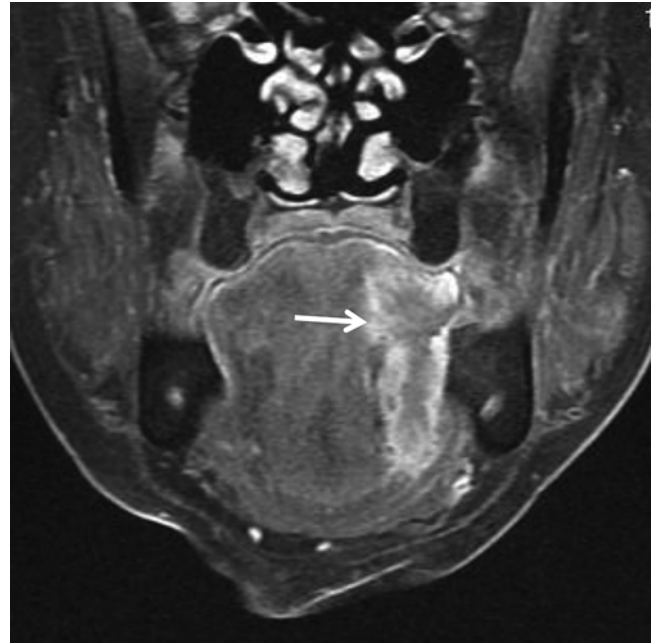


Fig. 5.58 Coronal fat-saturated post-contrast T1-weighted MRI. Tumor (*arrow*) enhances heterogeneously and involves the hyoglossus muscle



Fig. 5.59 Photomicrograph of histopathological specimen, coronal section (hematoxylin-eosin stain)

5.4.1.2 Case 2: 60-Year-Old Female, Left-Tongue SCC T4aN0 (Figs. 5.60, 5.61, 5.62, 5.63, 5.64, 5.65, 5.66 and 5.67)

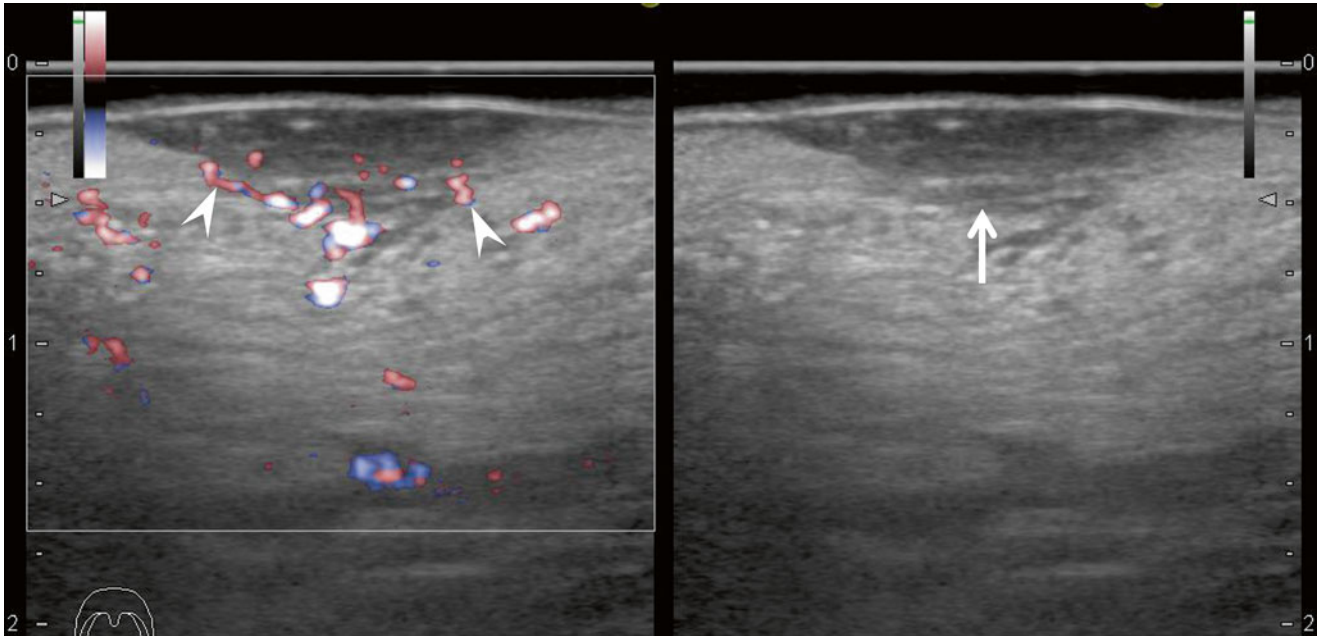


Fig. 5.60 Intraoral ultrasonography with the acoustic coupling device between the probe surface and the tumor surface (left, fine flow Doppler; right, B-mode). Tumor is demonstrated as an ill-defined hypoechoic area (*arrow*) continuous with the surrounding normal mucosal layer. Note the vascularity around the deep margins arising from neoangiogenesis at the tumor invasion front (*arrowheads*)



Fig. 5.61 Axial CECT. Tumor is demonstrated as an ill-defined enhancing mass at the left lateral margin of the tongue (*arrow*)

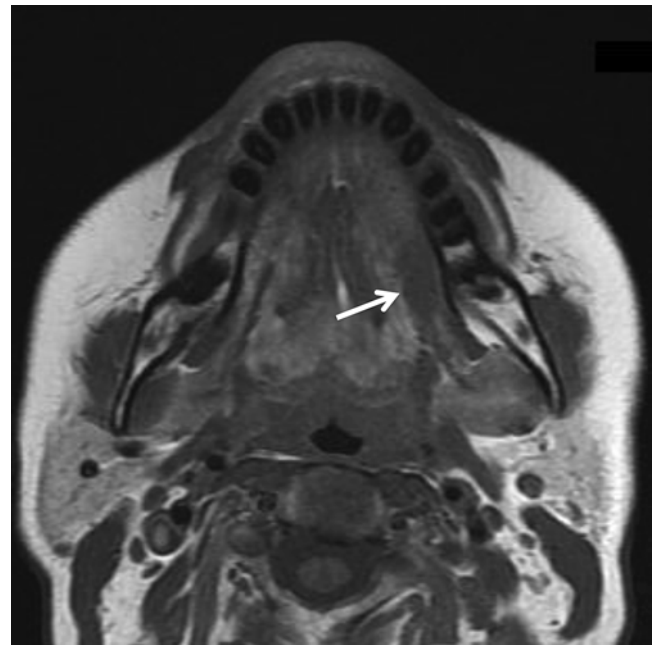


Fig. 5.62 Axial T1-weighted MRI. Tumor (*arrow*) is demonstrated as an intermediate signal intensity area with an ill-defined margin involving the left hyoglossus muscle

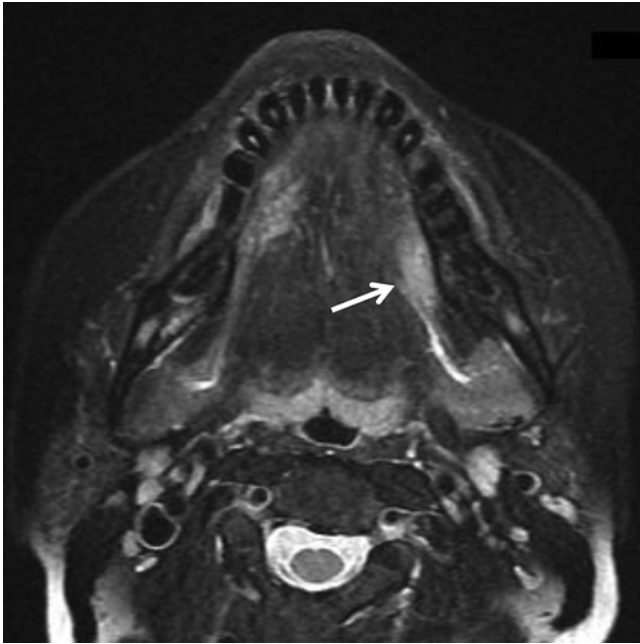


Fig. 5.63 Axial fat-saturated T2-weighted MRI. Tumor is demonstrated as relatively high heterogeneous intensity area with an ill-defined margin (*arrow*)

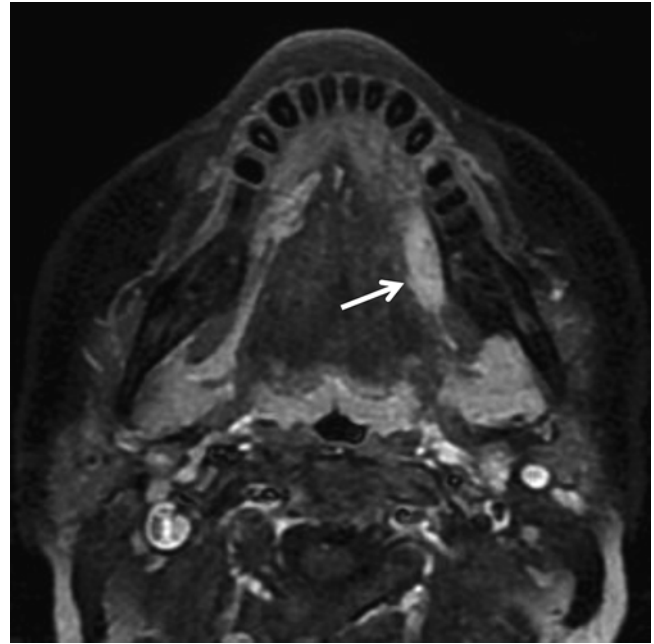


Fig. 5.64 Axial dynamic MRI. Tumor enhances homogeneously (*arrow*)

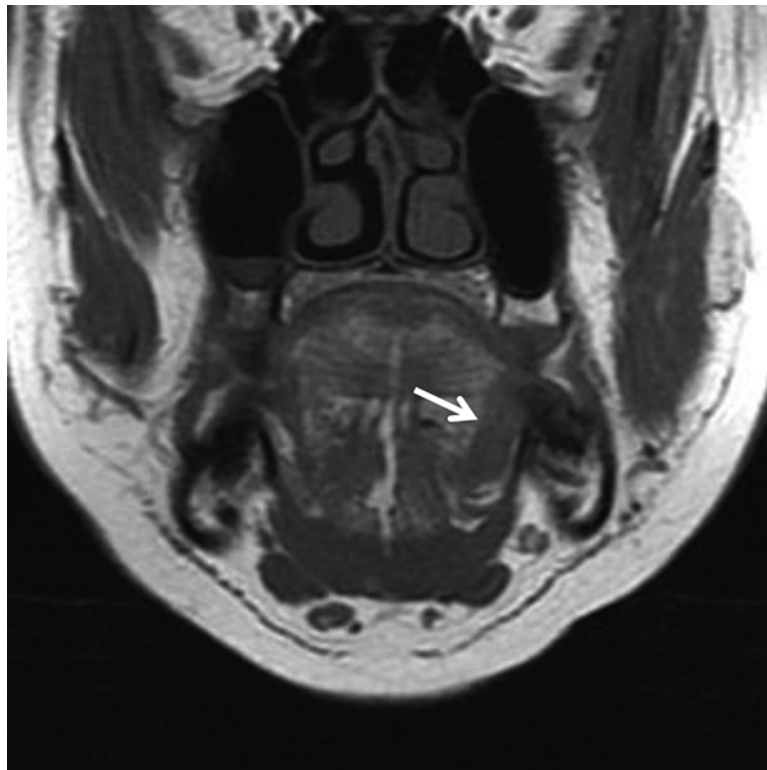


Fig. 5.65 Coronal T1-weighted MRI. Tumor is demonstrated as intermediate signal intensity (*arrow*)

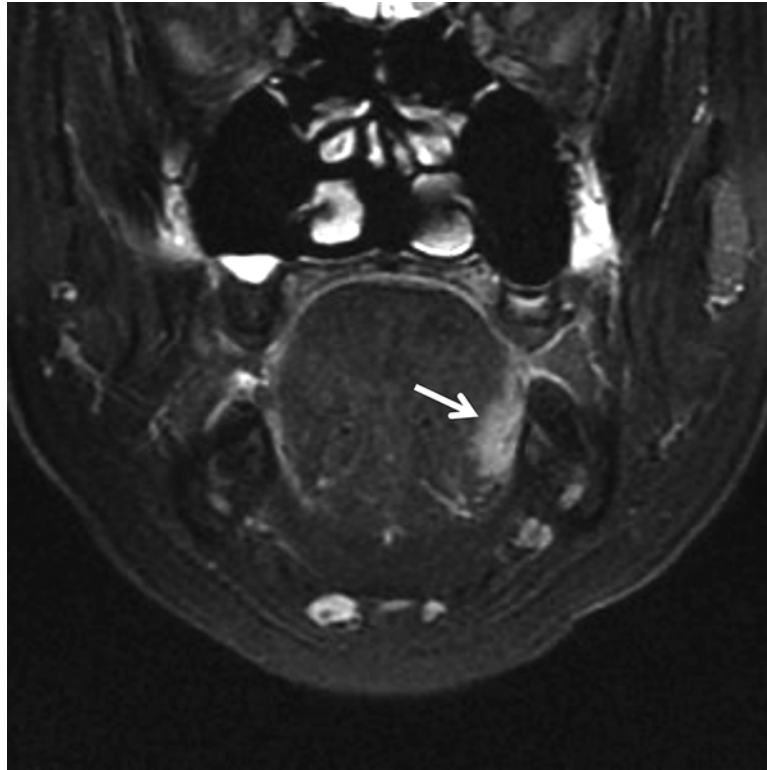


Fig. 5.66 Coronal fat-saturated T2-weighted MRI. Tumor is demonstrated as relatively high heterogeneous intensity (*arrow*)

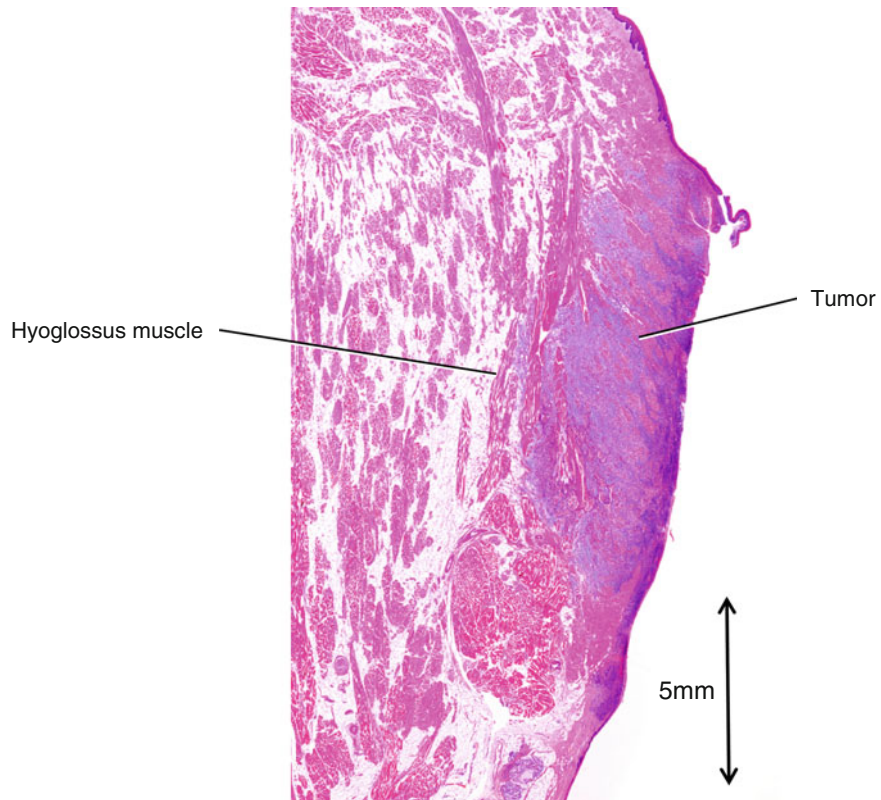


Fig. 5.67 Photomicrograph of histopathological specimen, coronal section (hematoxylin-eosin stain)

5.4.1.3 Case 3: 60-Year-Old Female, Right-Tongue SCC T2N0 (Figs. 5.68, 5.69, 5.70 and 5.71)

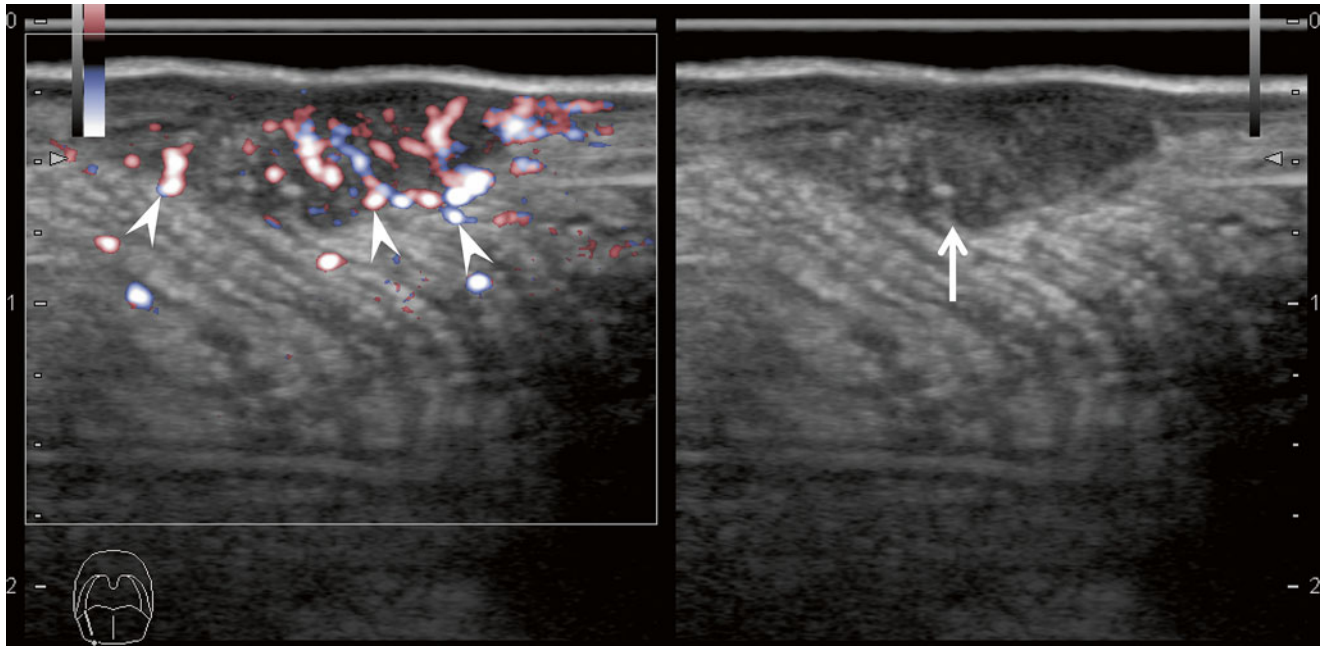


Fig. 5.68 Intraoral ultrasonography with the acoustic coupling device between the probe surface and the tumor surface (left, fine flow Doppler; right, B-mode). Tumor is demonstrated clearly as an ill-defined hypoechoic area (*arrow*) continuous with the surrounding normal mucosal layer. Note the prominent vascularity around the deep margins arising from neoangiogenesis at the tumor invasion front (*arrowheads*)

Fig. 5.69 Axial CECT. Tumor is markedly obscured by severe metal artifact of dental prosthesis

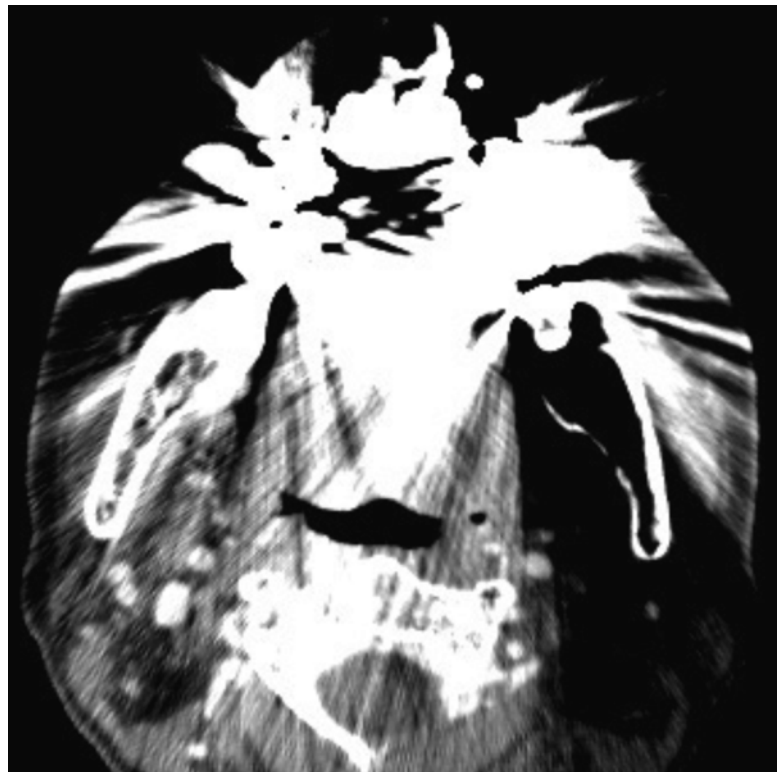


Fig. 5.70 Axial post-contrast T1-weighted MRI. Tumor is also obscured by susceptibility artifact of dental prosthesis

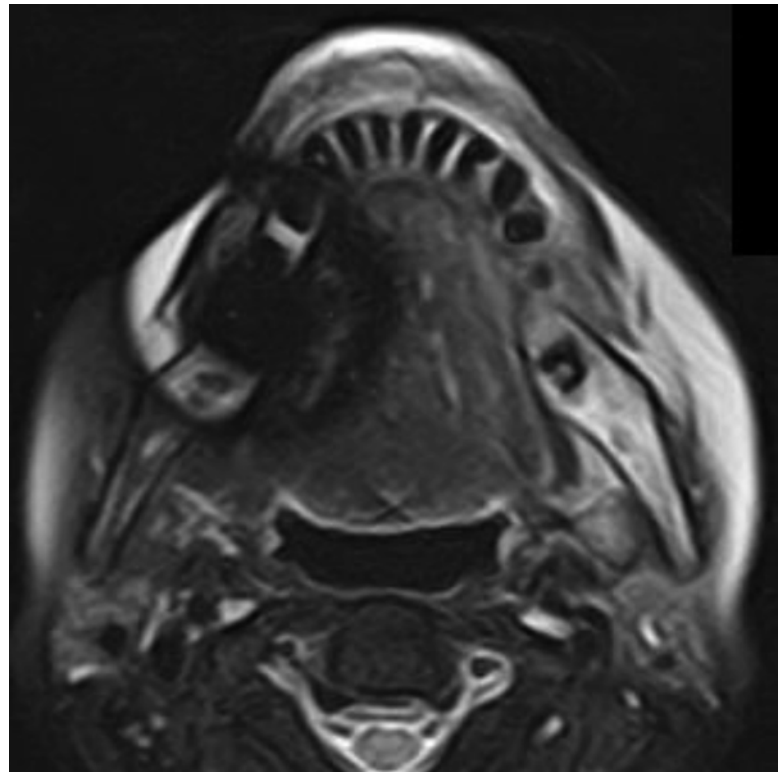


Fig. 5.71 Photomicrograph of histopathological specimen, coronal section (hematoxylin-eosin stain)

5.4.2 Gingival Carcinoma

5.4.2.1 Case 3: 62-Year-Old Male, Left-Mandibular Gingival SCC T4aN0 (Figs. 5.72, 5.73, 5.74, 5.75, 5.76, 5.77, 5.78, 5.79, 5.80, 5.81, 5.82, 5.83 and 5.84)

Fig. 5.72 Orthopantomography. An ill-defined bone destruction possibly caused by gingival SCC is demonstrated as an intermediate-type absorption at the left lower molar region possibly involving the mandibular canal (arrowhead)

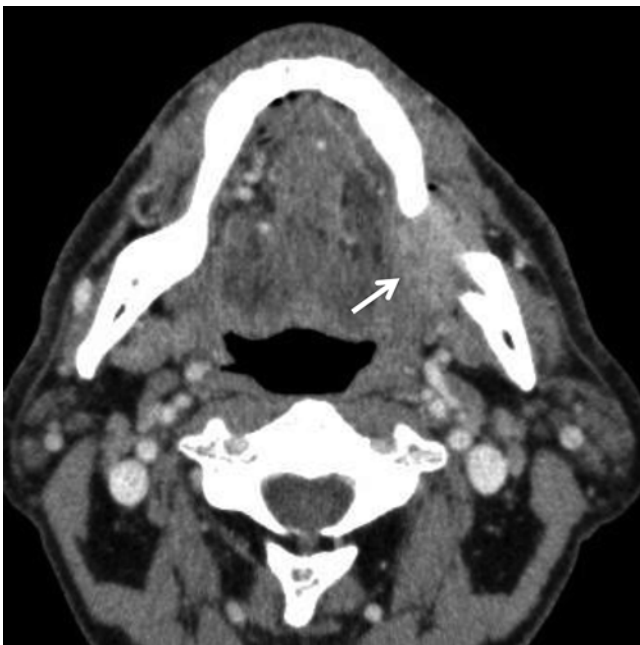
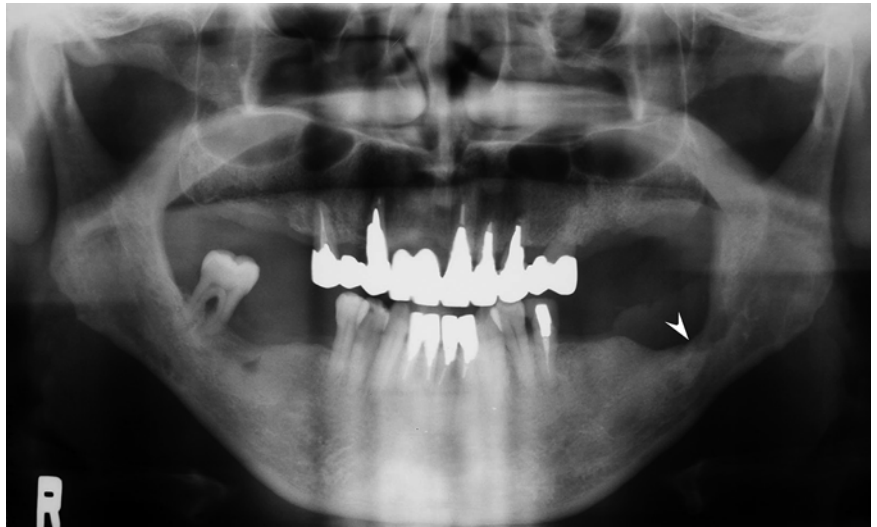


Fig. 5.73 Axial CECT. Tumor is demonstrated as an ill-defined enhancing mass involving the floor of the mouth (arrow)



Fig. 5.74 Axial plain CT with bone window



Fig. 5.75 Coronal plain CT with bone window

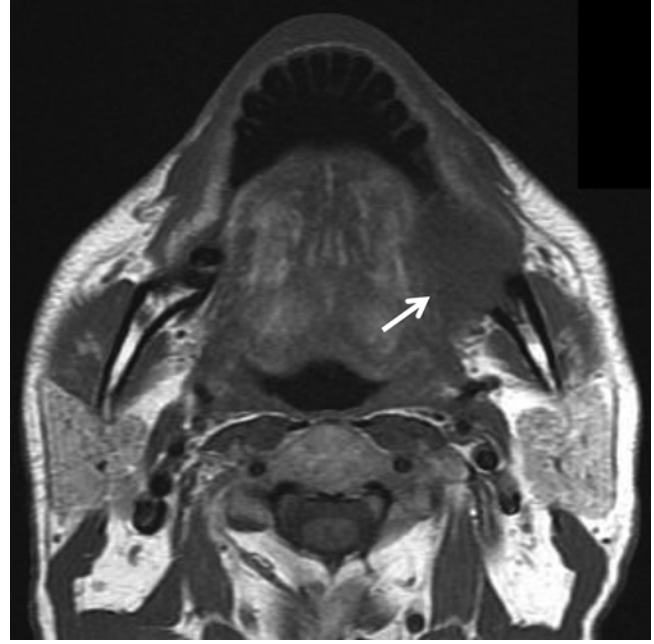


Fig. 5.77 Axial T1-weighted MRI. Tumor is demonstrated as an intermediate signal intensity area (*arrow*) with an ill-defined margin

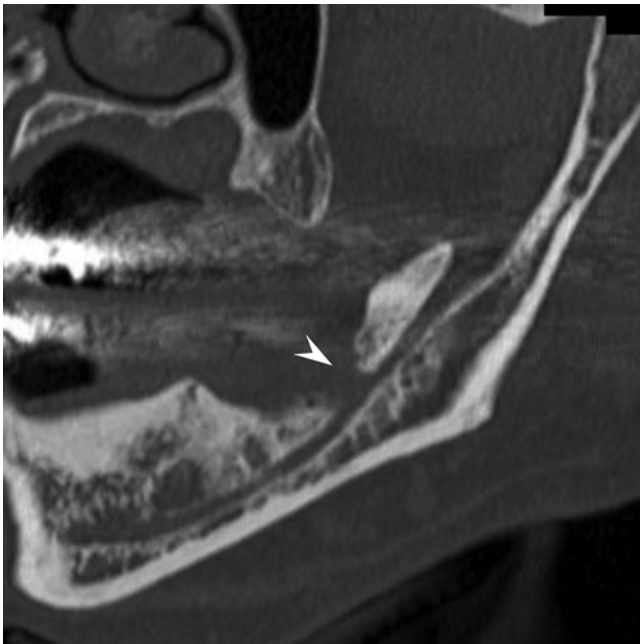


Fig. 5.76 Parasagittal plain CT with bone window. Destruction of the lower alveolar bone with an irregular margin possibly involving the mandibular canal wall is demonstrated (*arrowhead*)

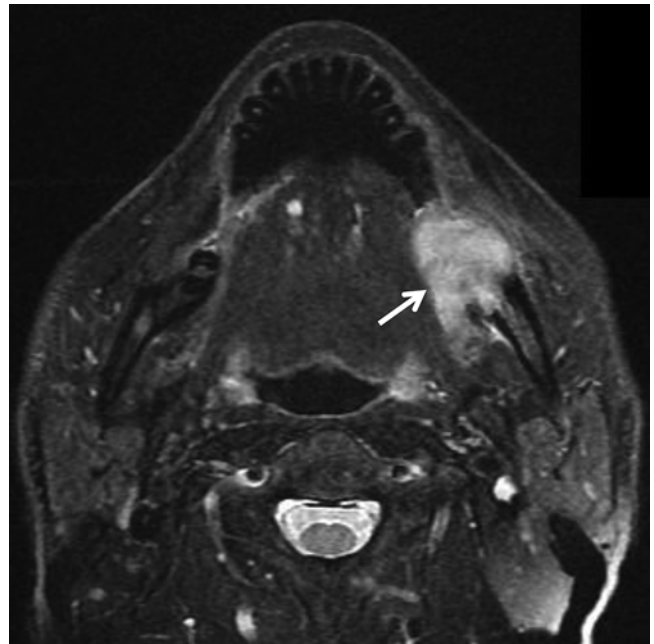


Fig. 5.78 Axial fat-saturated T2-weighted MRI. Tumor is demonstrated as relatively high heterogeneous intensity area (*arrow*) with bone marrow involvement

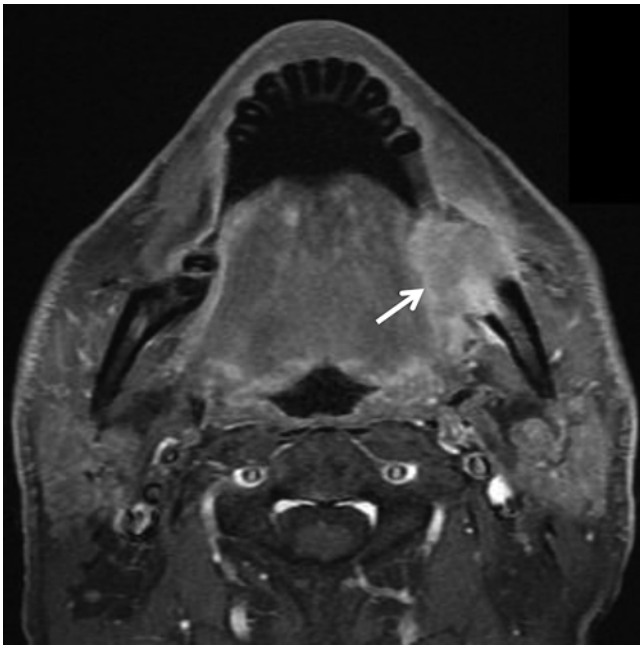


Fig. 5.79 Axial fat-saturated post-contrast T1-weighted MRI. Tumor enhances heterogeneously (*arrow*) and the peripheral portion of the tumor enhances prominently

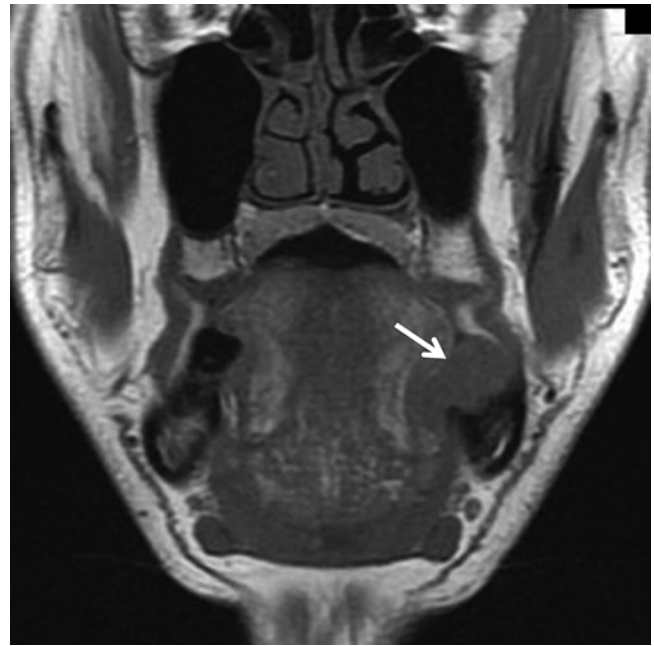


Fig. 5.81 Coronal T1-weighted MRI. Tumor is demonstrated as an intermediate signal intensity area involving the left mylohyoid muscle

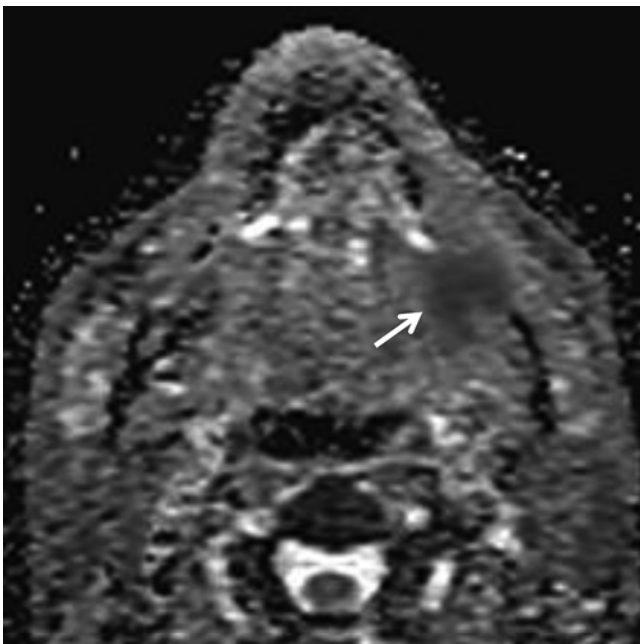


Fig. 5.80 Axial ADC map MRI. Tumor is demonstrated as a restricted diffusion area (*arrow*)

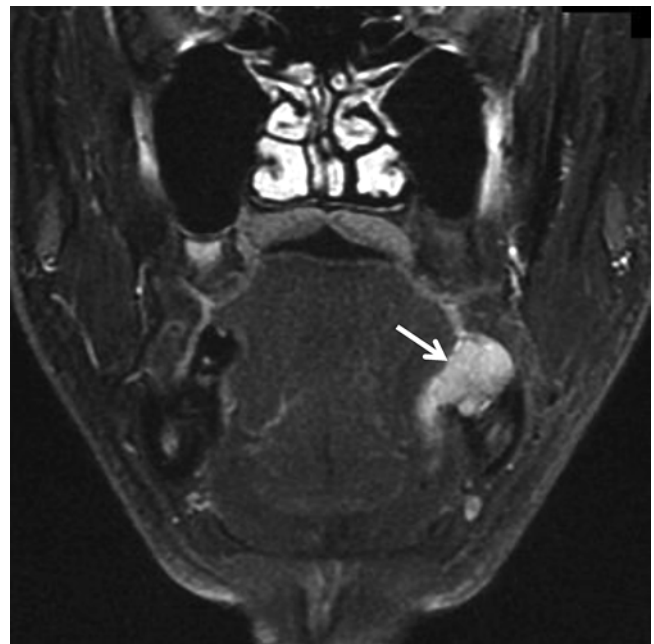


Fig. 5.82 Coronal fat-saturated T2-weighted MRI. Tumor is demonstrated as relatively high heterogeneous intensity (*arrow*)

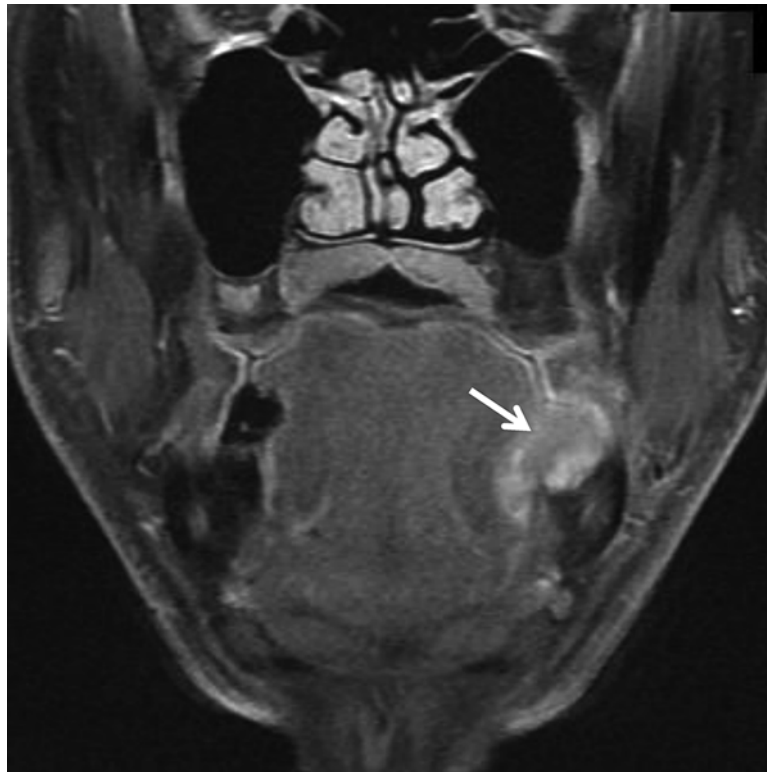


Fig. 5.83 Coronal fat-saturated post-contrast T1-weighted MRI. Tumor (*arrow*) enhances heterogeneously

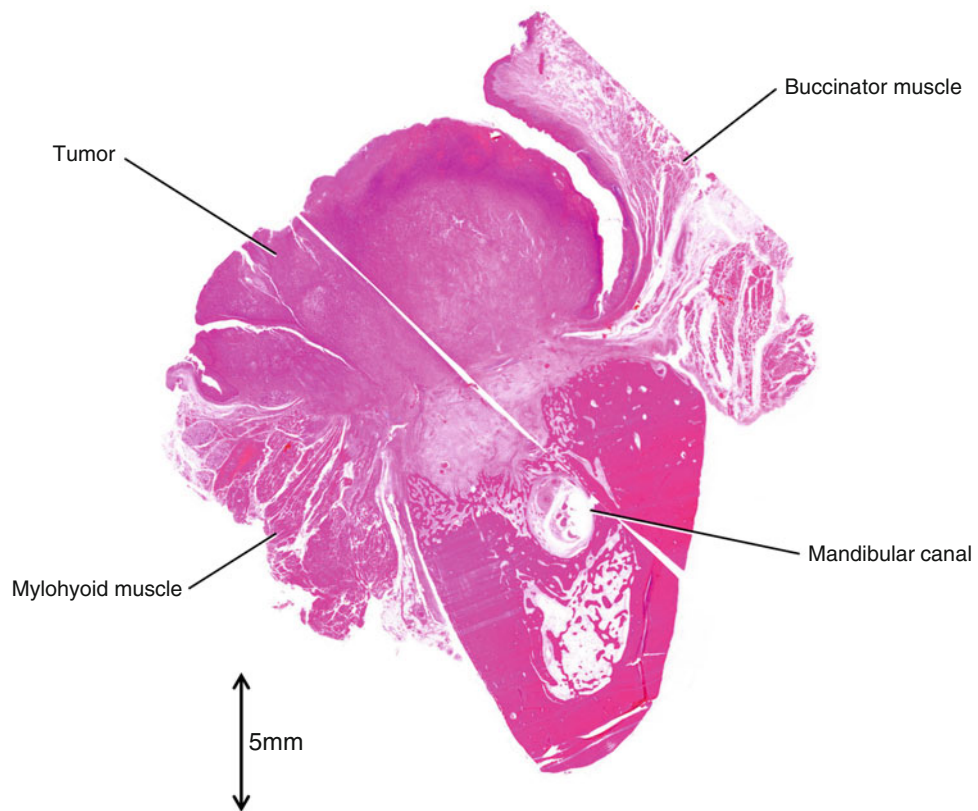


Fig. 5.84 Photomicrograph of histopathological specimen, coronal section (hematoxylin-eosin stain)

5.4.2.2 Case 4: 85-Year-Old Male, Right-Maxillary Gingival SCC, T4aN0 (Figs. 5.85, 5.86, 5.87, 5.88, 5.89, 5.90, 5.91, 5.92, 5.93, 5.94, 5.95 and 5.96)

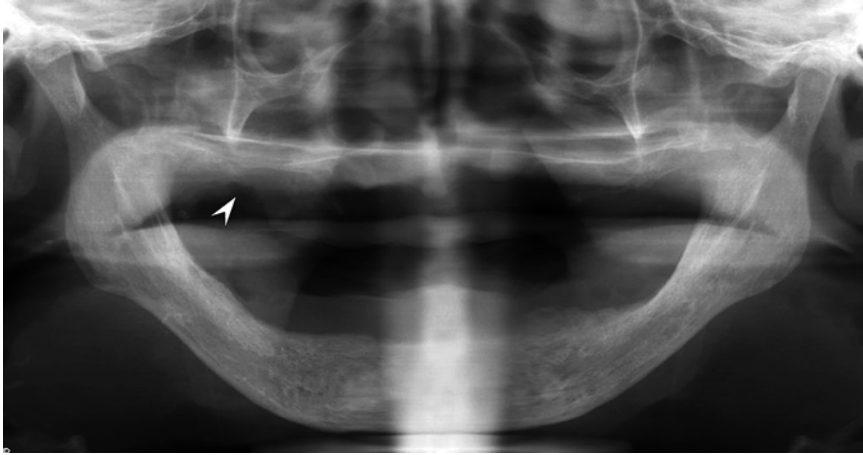


Fig. 5.85 Orthopantomography. An ill-defined bone destruction possibly caused by gingival SCC is demonstrated at the right upper molar region possibly involving the maxillary sinus (*arrowhead*)



Fig. 5.86 Axial CECT. Tumor is demonstrated as an ill-defined heterogeneously enhancing mass (*arrow*) and the periphery and central portions of the tumor enhance prominently

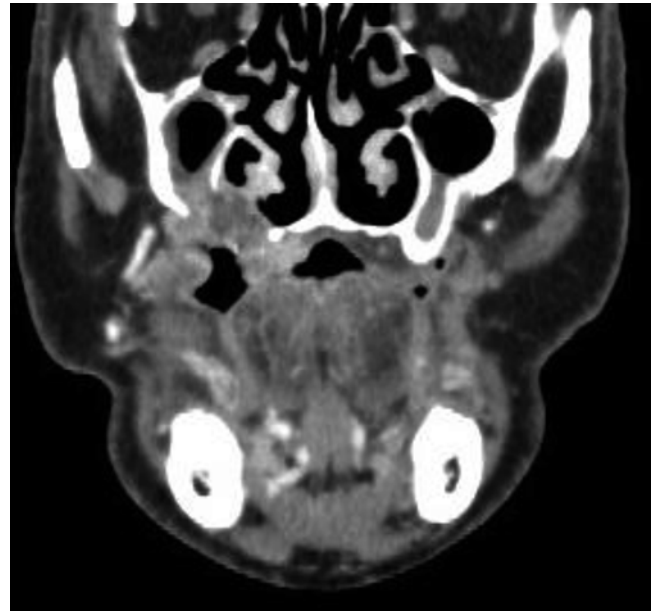


Fig. 5.87 Coronal CECT. Tumor (*arrow*) involves the buccinator muscle, the maxillary sinus, the nasal cavity, and the hard palate

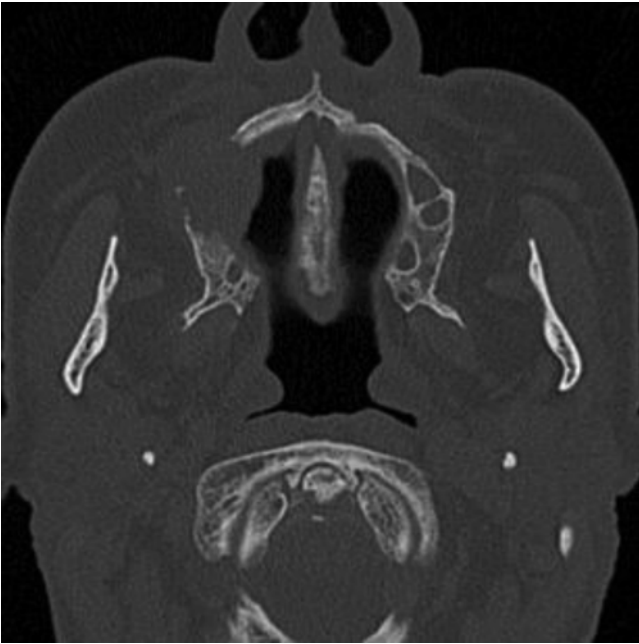


Fig. 5.88 Axial plain CT with bone window

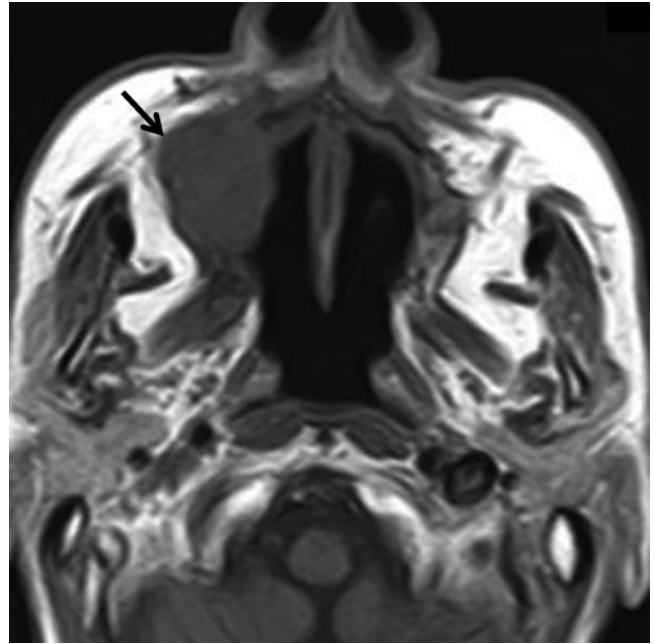


Fig. 5.90 Axial T1-weighted MRI. Tumor is demonstrated as an intermediate signal intensity area (*arrow*) with an ill-defined margin

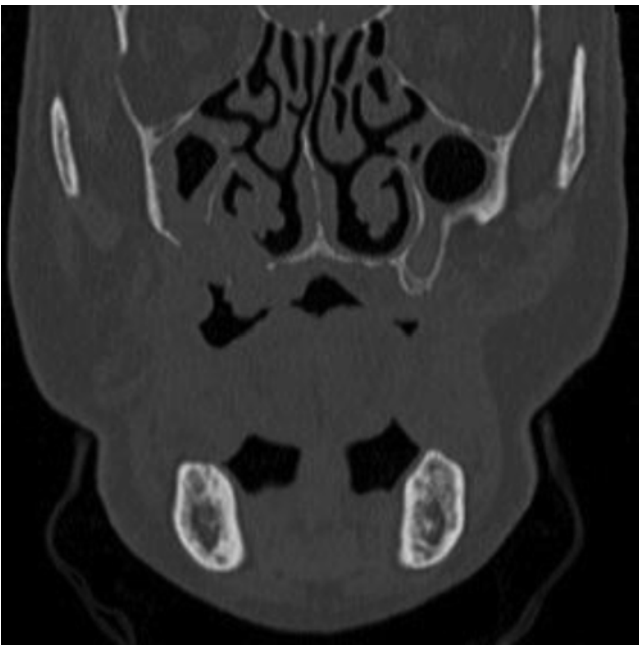


Fig. 5.89 Coronal plain CT with bone window. Destruction of the upper alveolar process, floor of the maxillary sinus, lateral wall of the nasal cavity, and the hard palate are demonstrated

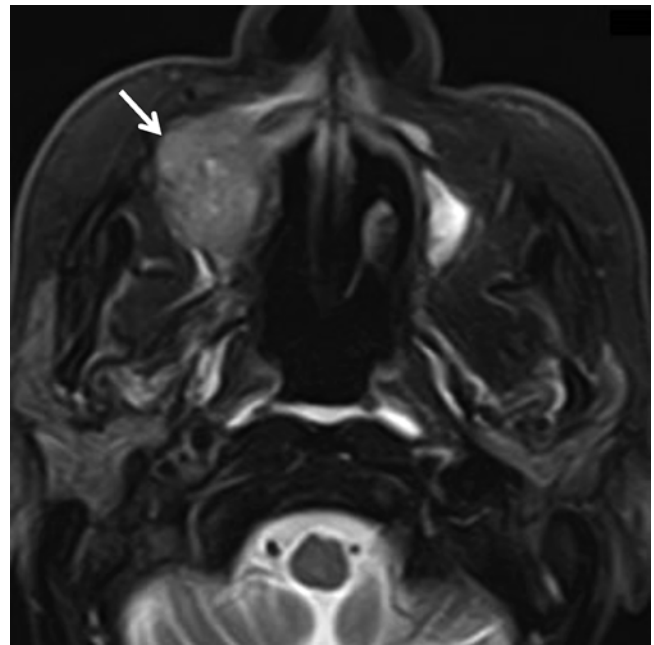


Fig. 5.91 Axial fat-saturated T2-weighted MRI. Tumor is demonstrated as relatively high heterogeneous intensity area (*arrow*)

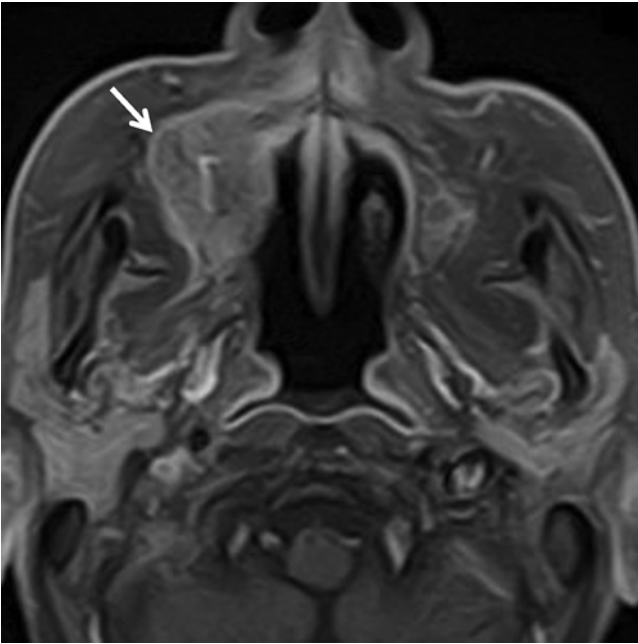


Fig. 5.92 Axial fat-saturated post-contrast T1-weighted MRI. Tumor enhances heterogeneously with an ill-defined margin (*arrow*) and the periphery and central portions of the tumor enhance prominently

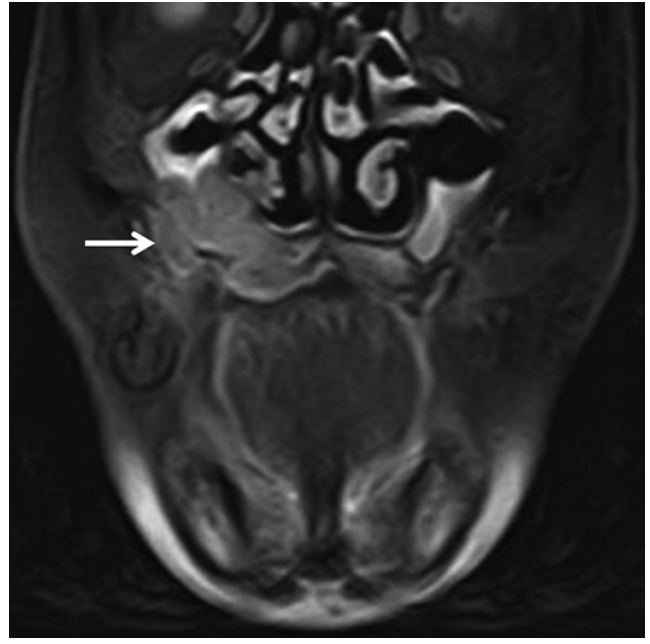


Fig. 5.94 Coronal fat-saturated T2-weighted MRI. Tumor is demonstrated as relatively high heterogeneous intensity (*arrow*). The signal intensity of the tumor is lower than that of thickened mucous membrane locating just above the tumor

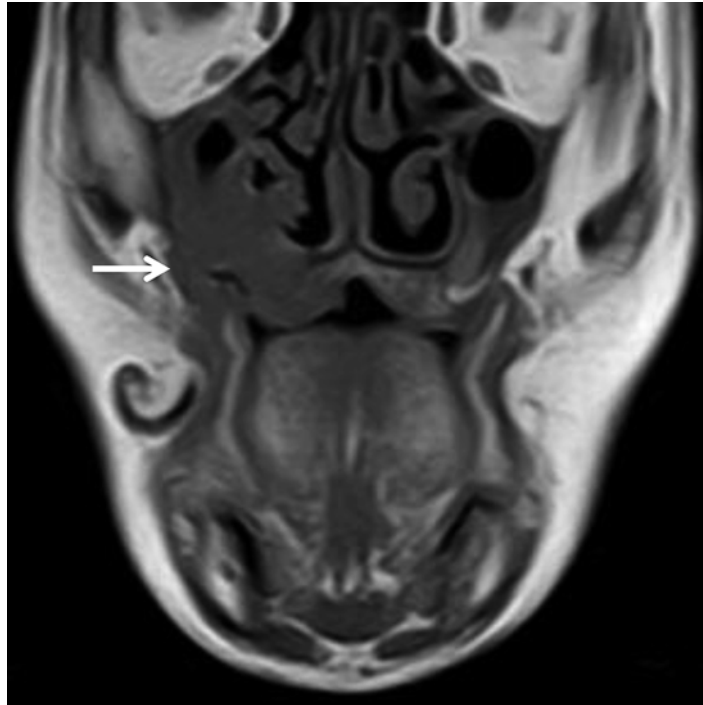


Fig. 5.93 Coronal T1-weighted MRI. Tumor is demonstrated as an intermediate signal intensity area (*arrow*)

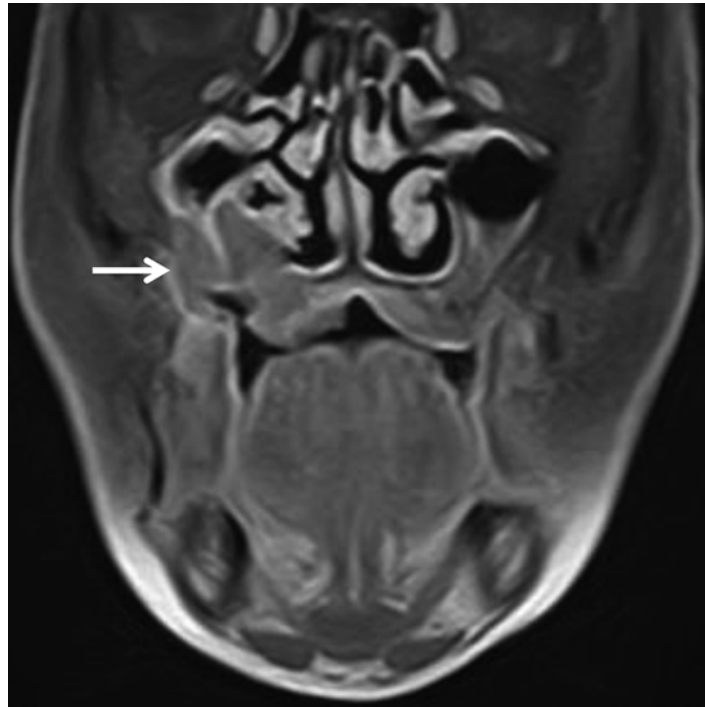


Fig. 5.95 Coronal fat-saturated post-contrast T1-weighted MRI. Tumor enhances heterogeneously and the signal intensity of the enhanced tumor is lower than that of thickened mucous membrane

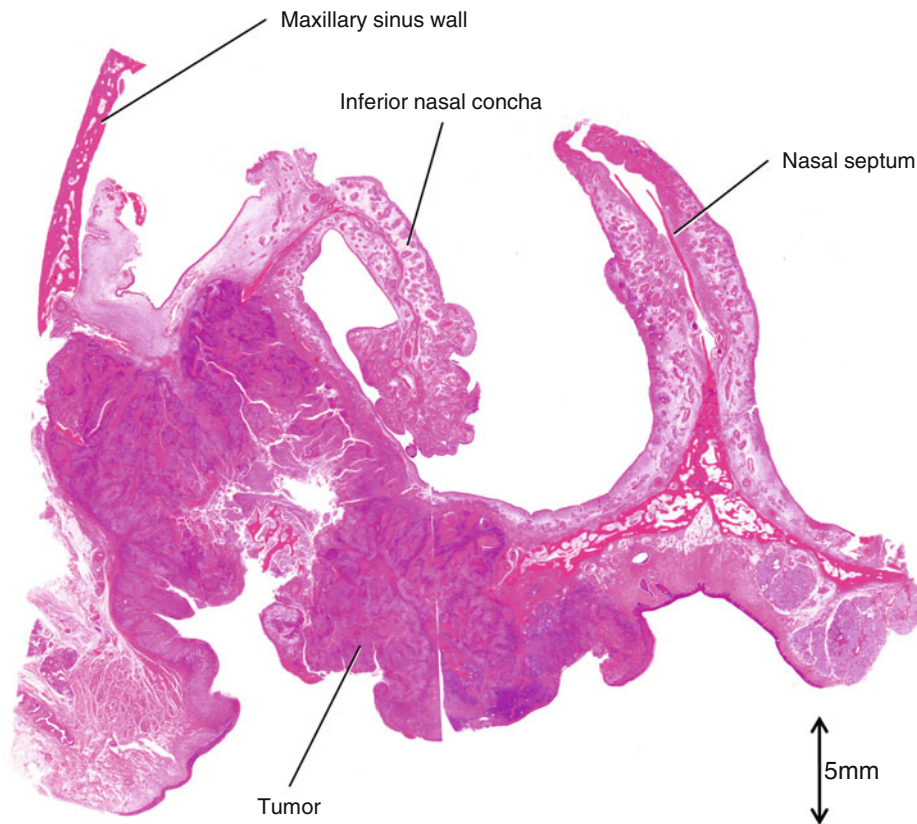


Fig. 5.96 Photomicrograph of histopathological specimen, coronal section (hematoxylin-eosin stain)

5.4.3 Floor of the Mouth Carcinoma

5.4.3.1 Case 5: 64-Year-Old Male, Floor of the Mouth SCC T4aN2c (Figs. 5.97, 5.98, 5.99, 5.100, 5.101, 5.102, 5.103, 5.104 and 5.105)

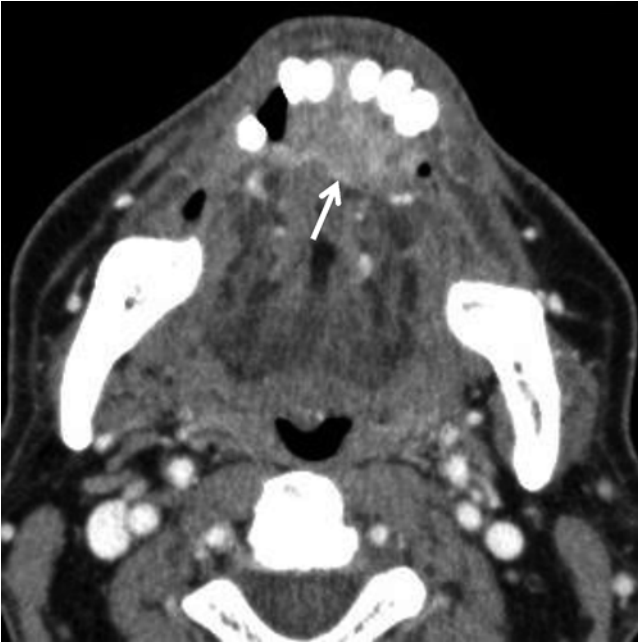


Fig. 5.97 Axial CECT. Tumor is demonstrated as an ill-defined heterogeneously enhancing mass (*arrow*) involving the bilateral sublingual space



Fig. 5.98 Sagittal CECT. Tumor (*arrow*) involves the gingival mucosa and the genioglossus muscle

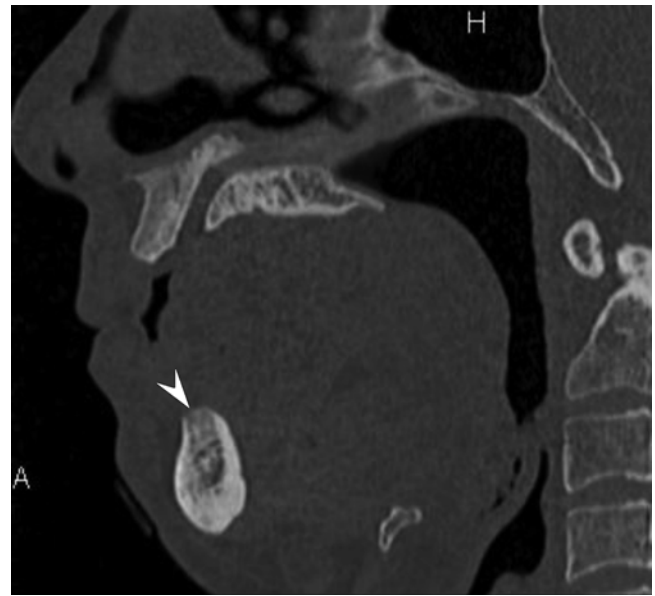


Fig. 5.99 Sagittal plain CT with bone window. Erosion of the cortex of the lower alveolar ridge is demonstrated (*arrowheads*)

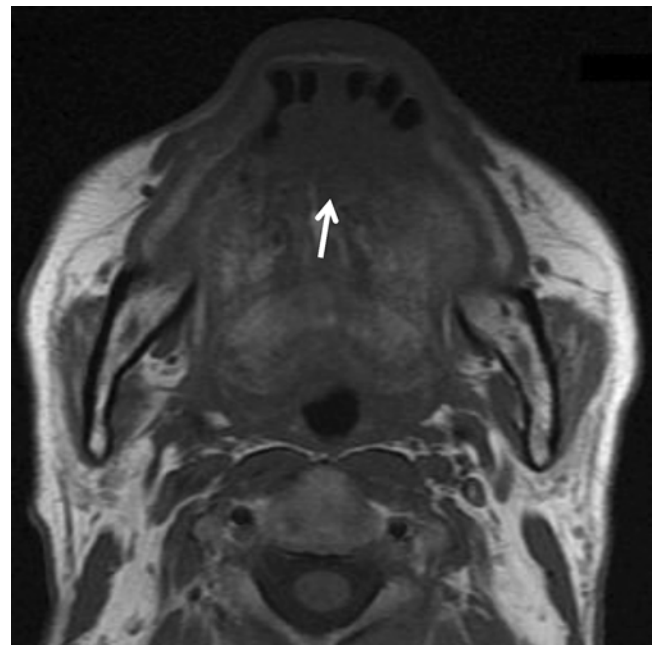


Fig. 5.100 Axial T1-weighted MRI. Tumor is demonstrated as an intermediate signal intensity area (*arrow*) with an ill-defined margin. Tumor (*arrow*) involves the genioglossus muscle

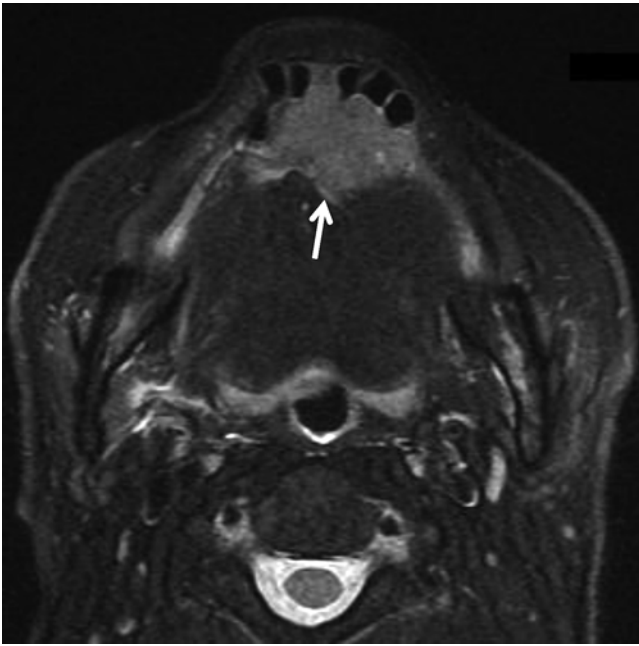


Fig. 5.101 Axial fat-saturated T2-weighted MRI. Tumor is demonstrated as relatively high heterogeneous intensity area (*arrow*)

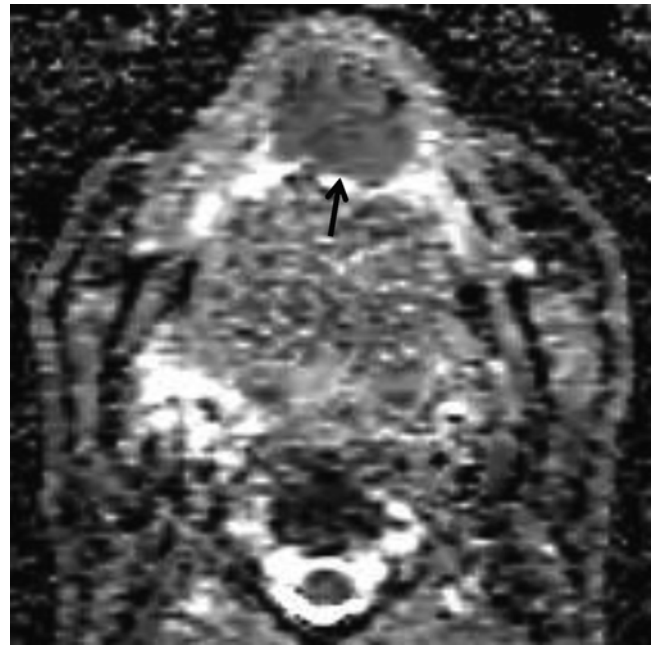


Fig. 5.103 Axial ADC map MRI. Tumor is demonstrated as a restricted diffusion area (*arrow*)

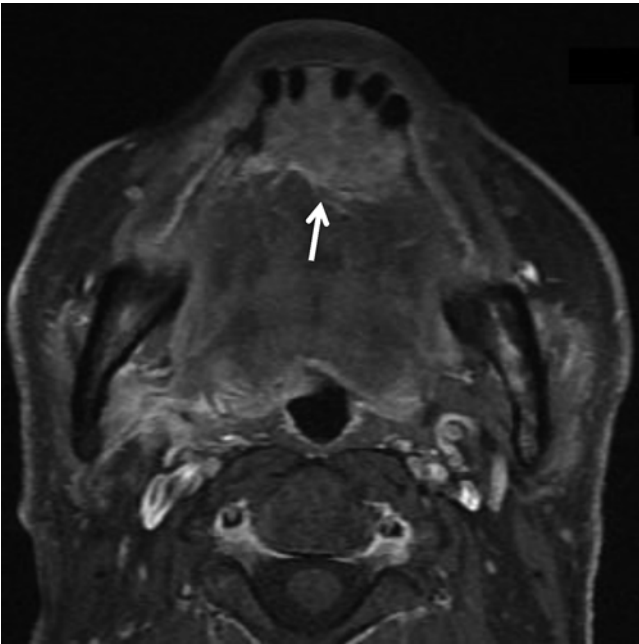


Fig. 5.102 Axial fat-saturated post-contrast T1-weighted MRI. Tumor enhances heterogeneously with an ill-defined margin (*arrow*)

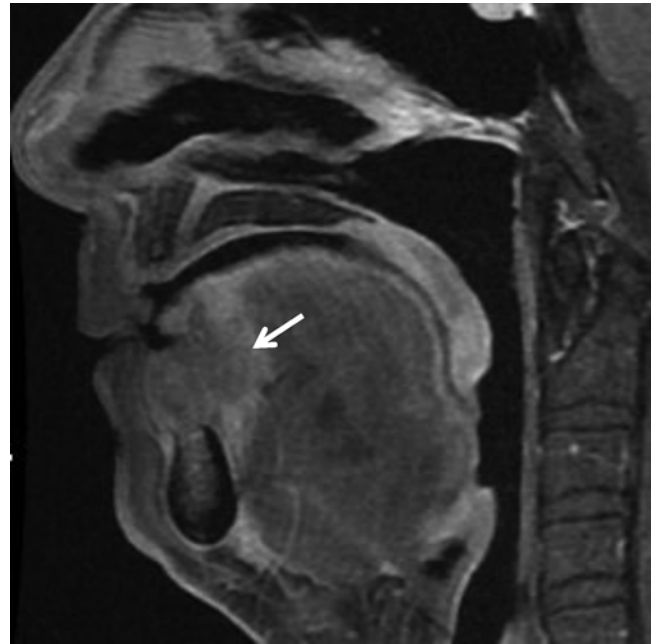


Fig. 5.104 Sagittal fat-saturated post-contrast T1-weighted MRI. Tumor enhances heterogeneously with an ill-defined margin (*arrow*)

5.4.4 Buccal Mucosa Carcinoma

5.4.4.1 Case 6: 78-Year-Old Male, Buccal Mucosa SCC T2N0 (Figs. 5.106, 5.107, 5.108, 5.109, 5.110, 5.111, 5.112, 5.113, 5.114 and 5.115)

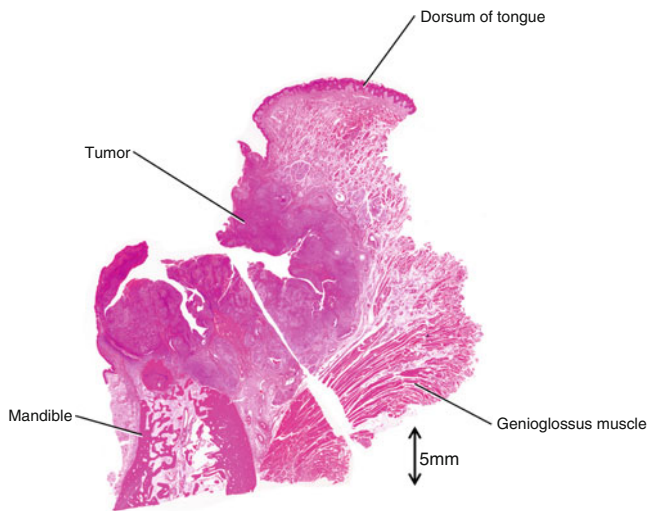


Fig. 5.105 Photomicrograph of histopathological specimen, sagittal section (hematoxylin-eosin stain)



Fig. 5.106 Axial CECT. Tumor is demonstrated as an ill-defined heterogeneously enhancing mass (*arrow*) involving the buccinator muscle

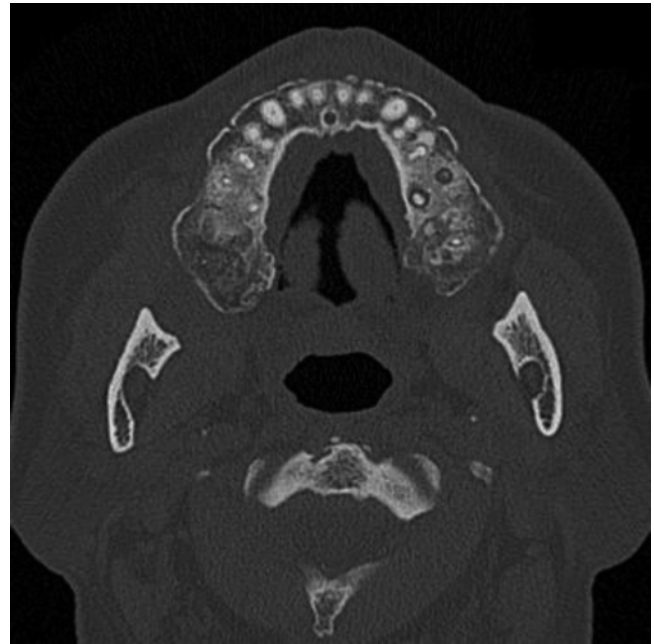


Fig. 5.107 Axial plain CT with bone window. No apparent destruction of adjacent bone cortex of the maxilla is observed

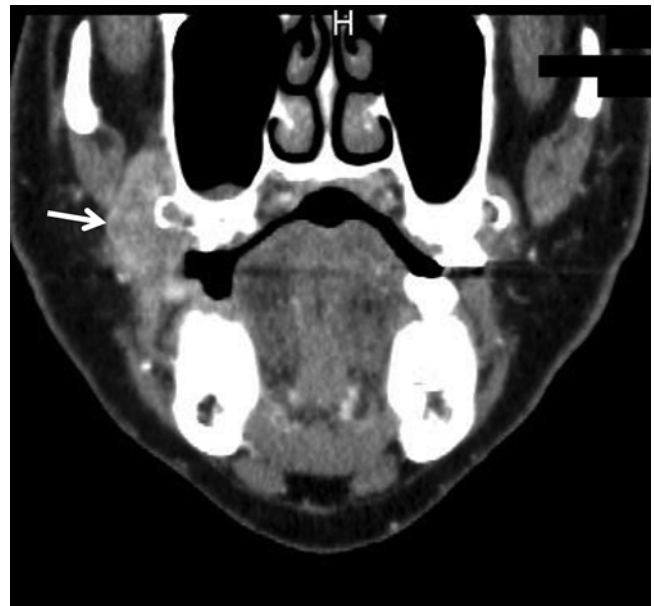


Fig. 5.108 Coronal CECT. Tumor (*arrow*) involves the buccal space



Fig. 5.109 Axial T1-weighted MRI. Tumor is demonstrated as an intermediate signal intensity area (*arrow*) with an ill-defined margin

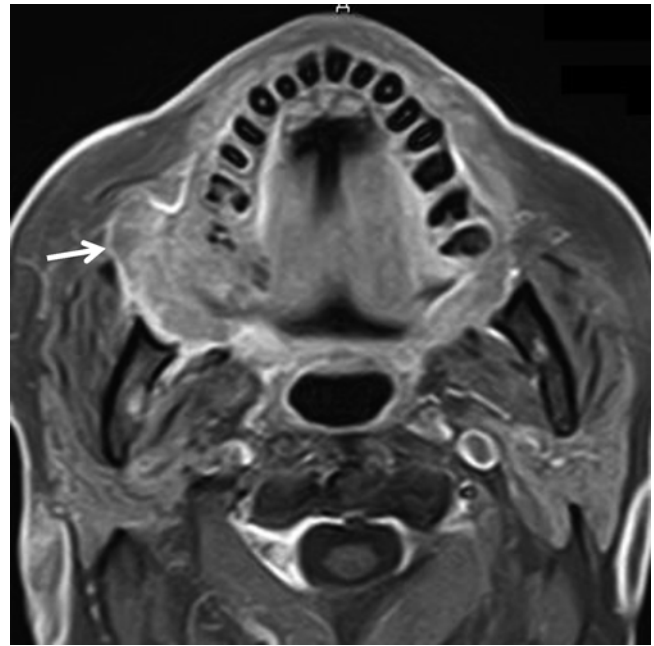


Fig. 5.111 Axial fat-saturated post-contrast T1-weighted MRI. Tumor enhances heterogeneously with an ill-defined margin (*arrow*)

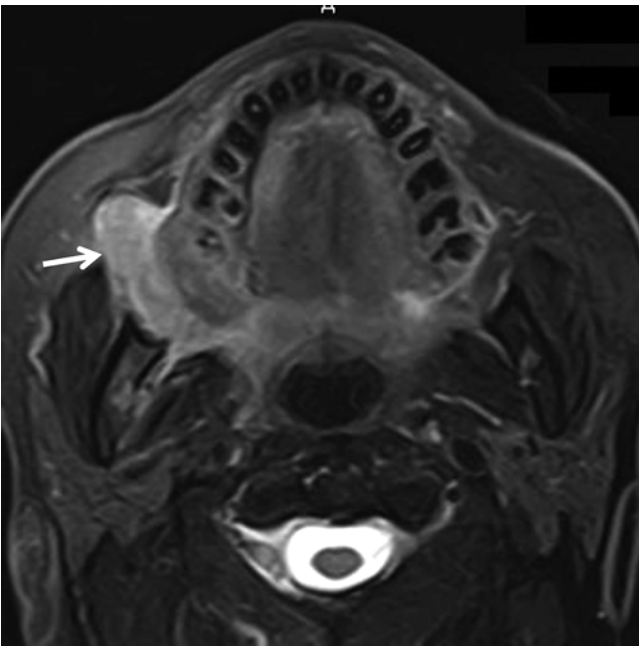


Fig. 5.110 Axial fat-saturated T2-weighted MRI. Tumor is demonstrated as relatively high heterogeneous intensity area (*arrow*)

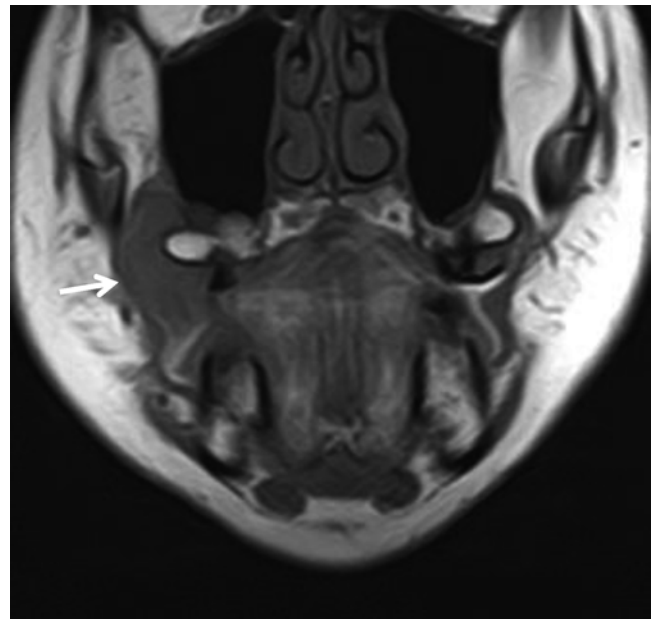


Fig. 5.112 Coronal T1-weighted MRI. Tumor is demonstrated as an intermediate signal intensity area (*arrow*)

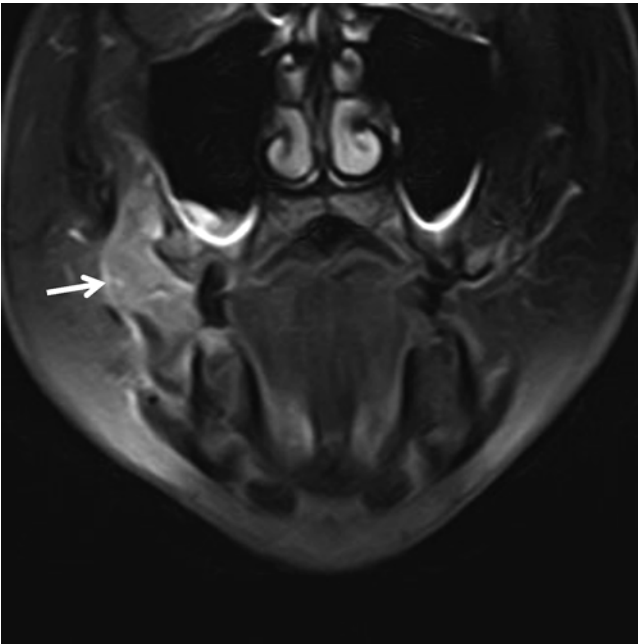


Fig. 5.113 Coronal fat-saturated T2-weighted MRI. Tumor is demonstrated as relatively high heterogeneous intensity (*arrow*). The signal intensity of the tumor is lower than that of thickened mucous membrane at the floor of the maxillary sinus

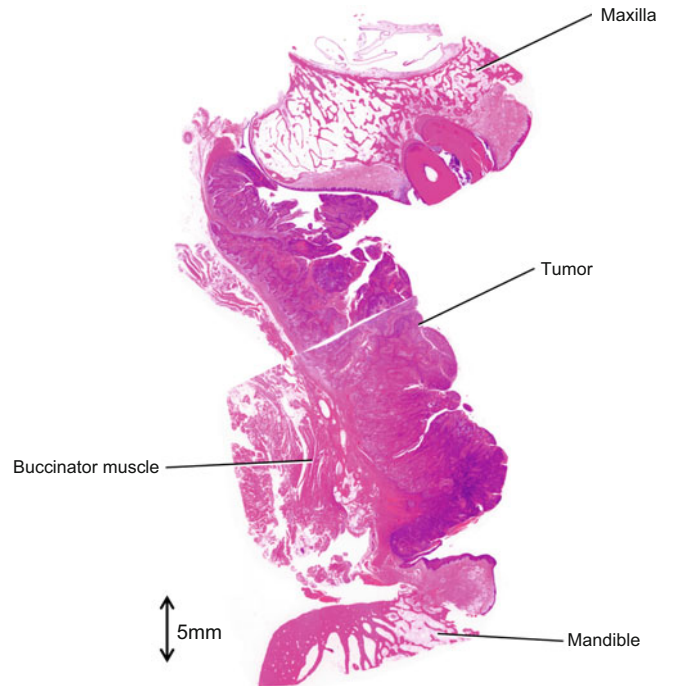


Fig. 5.115 Photomicrograph of histopathological specimen, coronal section (hematoxylin-eosin stain)

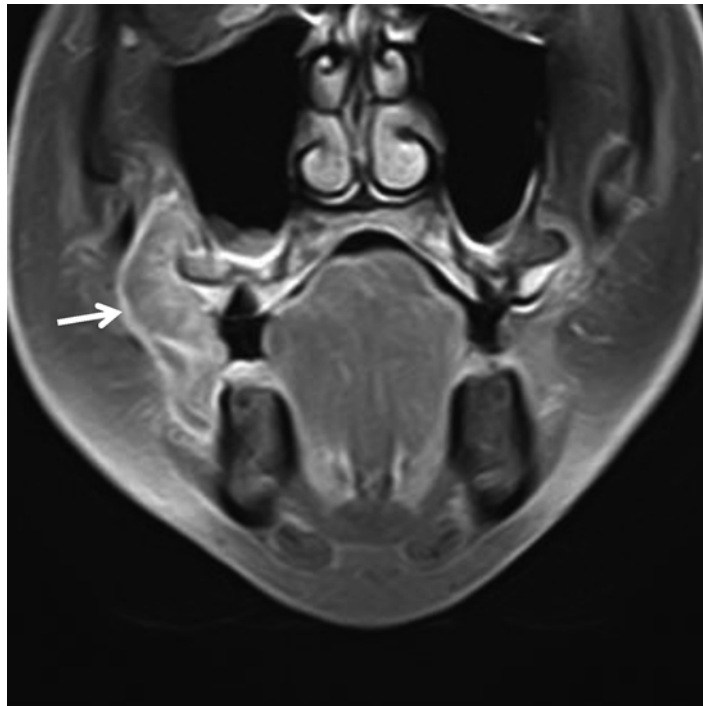


Fig. 5.114 Coronal fat-saturated post-contrast T1-weighted MRI. Tumor enhances heterogeneously (*arrow*) and the peripheral portion of the tumor enhances prominently

5.4.5 Lymph Node Metastasis

5.4.5.1 Case 7: 64-Year-Old Male, Floor of the Mouth SCC T4aN2c (Figs. 5.116, 5.117, 5.118, 5.119, 5.120, 5.121, 5.122, 5.123, 5.124, 5.125 and 5.126)

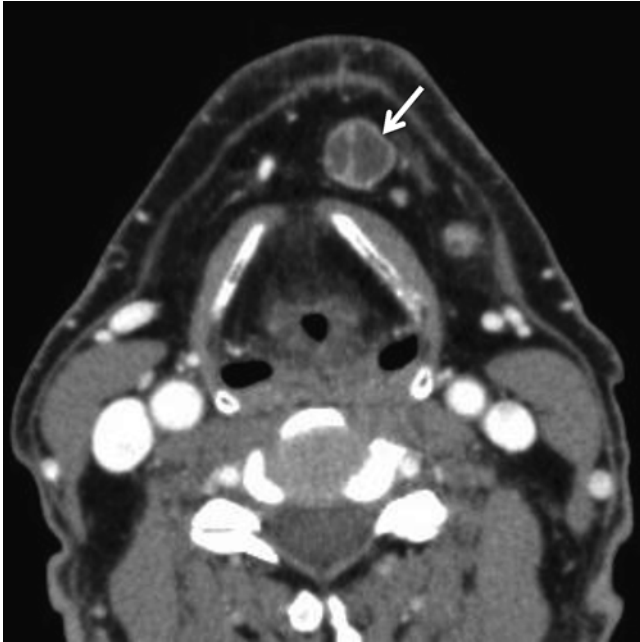


Fig. 5.116 Axial CECT. The metastatic left submental lymph node (*arrow*) is demonstrated as an oval-shaped nodule without distinct fatty hilum. Note the enhancing margin (rim enhancement) and central low-density area caused by central necrosis



Fig. 5.117 Sagittal CECT. The left submental lymph node with rim enhancement is demonstrated (*arrow*)

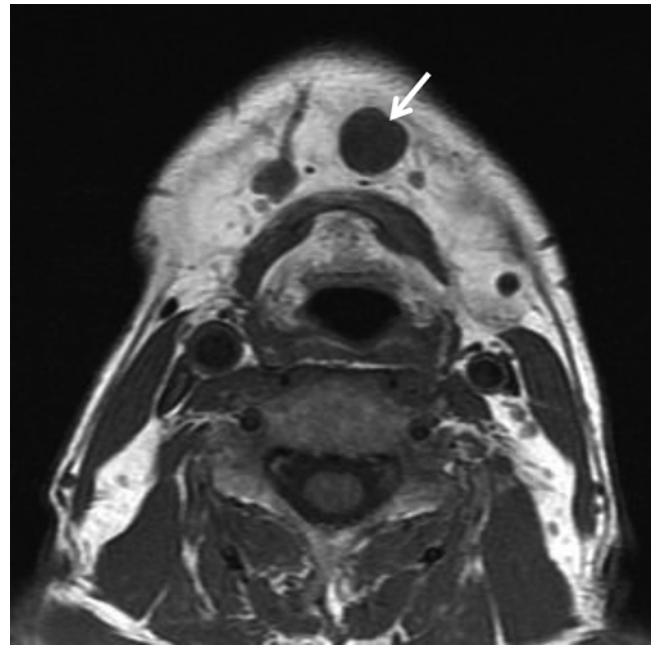


Fig. 5.118 Axial T1-weighted MRI. The left submental lymph node shows intermediate signal intensity

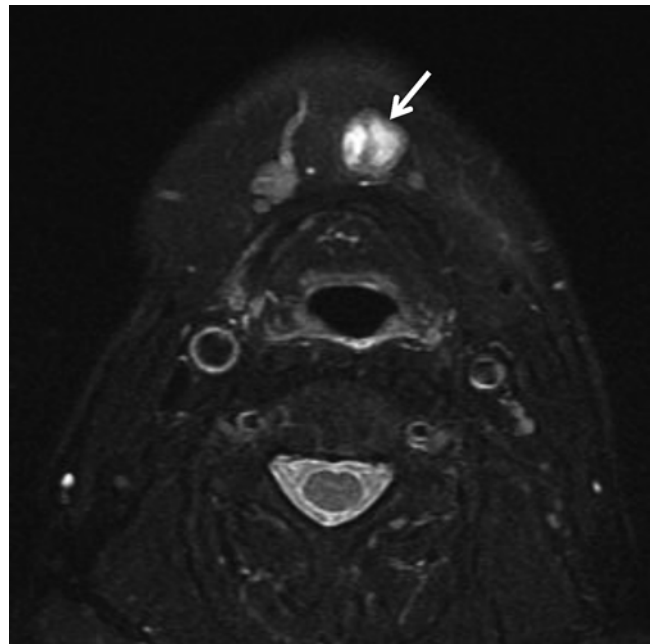


Fig. 5.119 Axial fat-saturated T2-weighted MRI. The left submental lymph node (*arrow*) shows heterogeneous intensity. Marginal portion of the node shows intermediate intensity and central portion shows high intensity

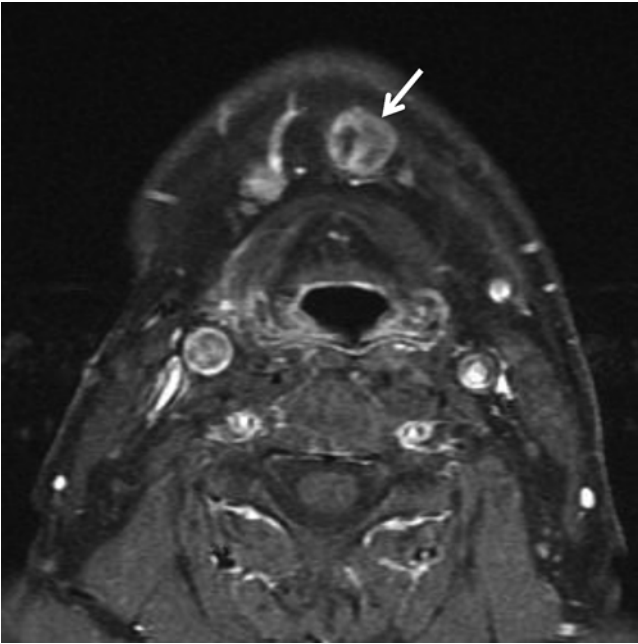


Fig. 5.120 Axial fat-saturated post-contrast T1-weighted MRI. Marginal portion of the left submental lymph node enhances and central portion remains unenhanced

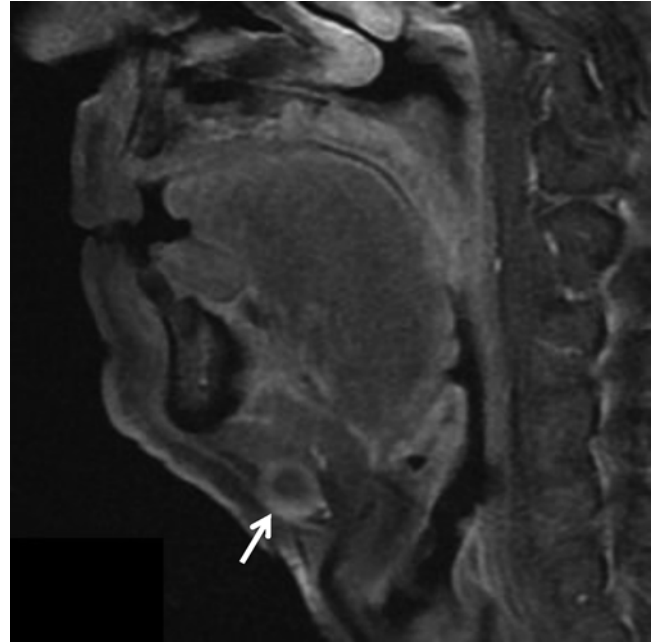


Fig. 5.121 Sagittal fat-saturated post-contrast T1-weighted MRI. The left submental lymph node with rim enhancement is demonstrated (*arrow*)

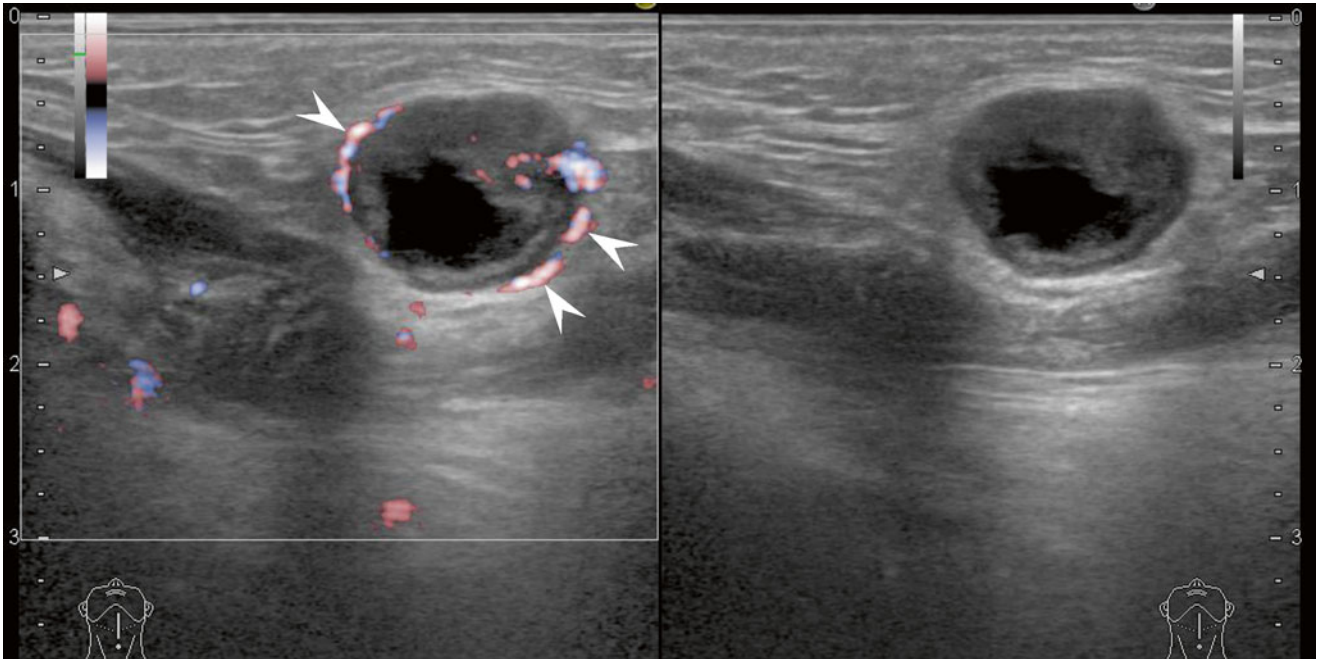


Fig. 5.122 Sagittal ultrasonography of the submental region (left, fine flow Doppler; right, B-mode). The left submental lymph node with anechoic area caused by central necrosis is demonstrated. Note the characteristic peripheral vascularity (*arrowheads*)

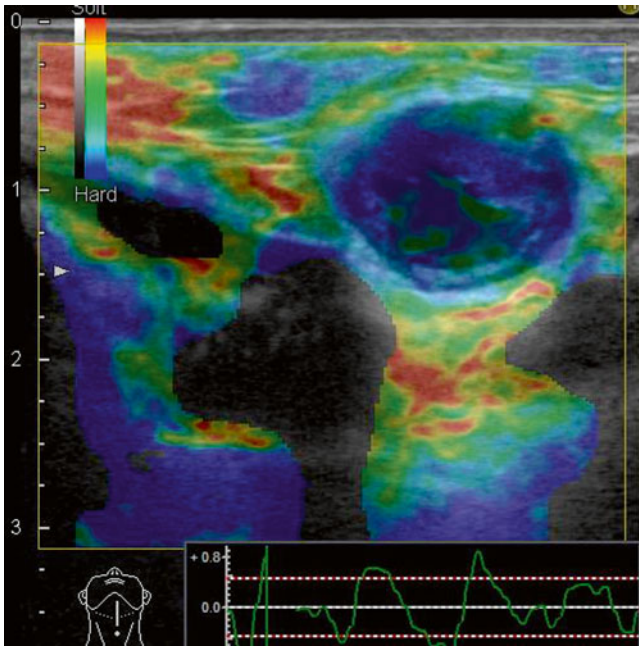


Fig. 5.123 Sagittal elastosonography of the left submental lymph node. Almost the whole node is occupied with a blue, hard area suggesting malignancy

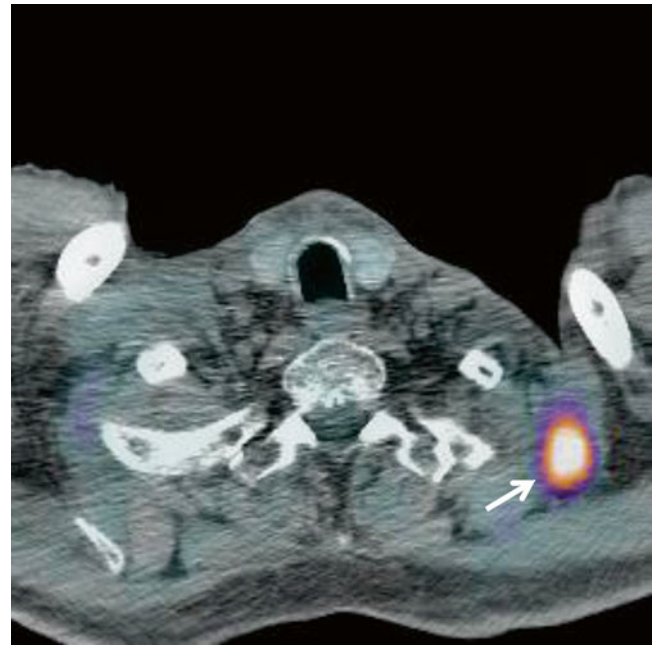


Fig. 5.125 Axial PET/CT. Recurrent tumor locating at the left supraclavicular fossa is disclosed after initial treatment (*arrow*)

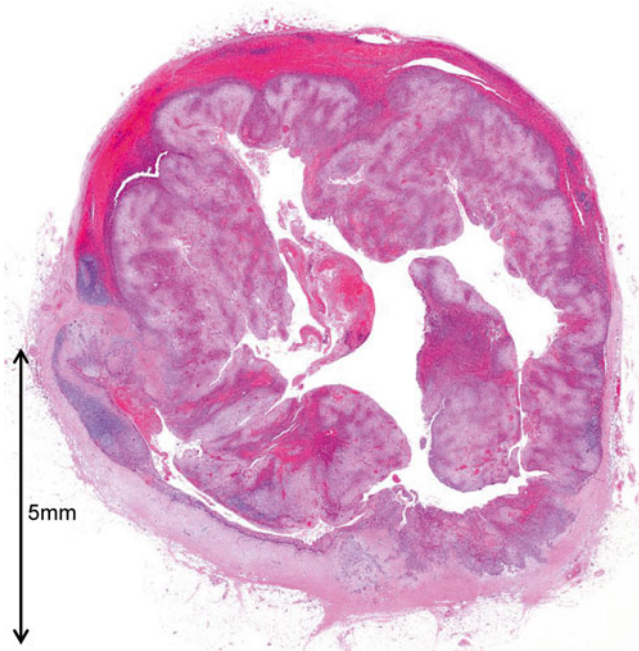


Fig. 5.124 Photomicrograph of histopathological specimen of the left submental lymph node (hematoxylin-eosin stain)



Fig. 5.126 Axial CECT. Recurrent tumor locating at the left supraclavicular fossa (*arrow*)

5.4.5.2 Case 8: 61-Year-Old Male, Left-Maxillary Gingival SCC T1N2b (Figs. 5.127, 5.128, 5.129, 5.130 and 5.131)

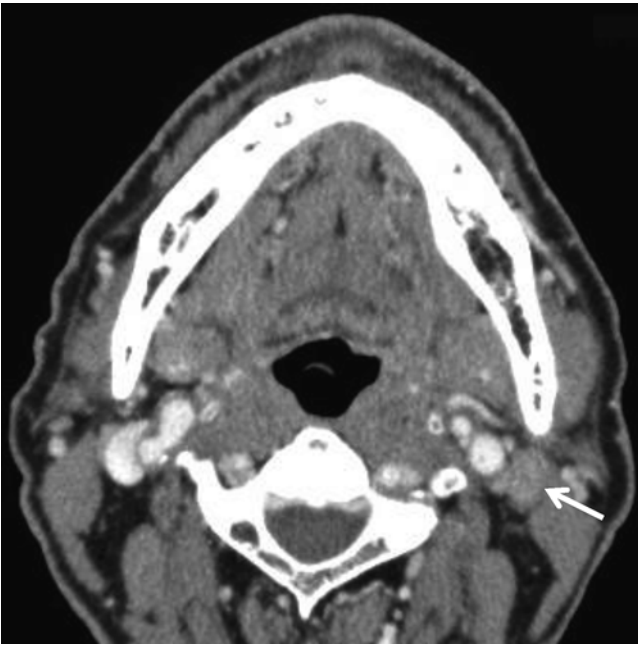


Fig. 5.127 Axial CECT. An enlarged homogeneously enhancing superior internal jugular node is demonstrated (*arrow*). No apparent necrosis is observed

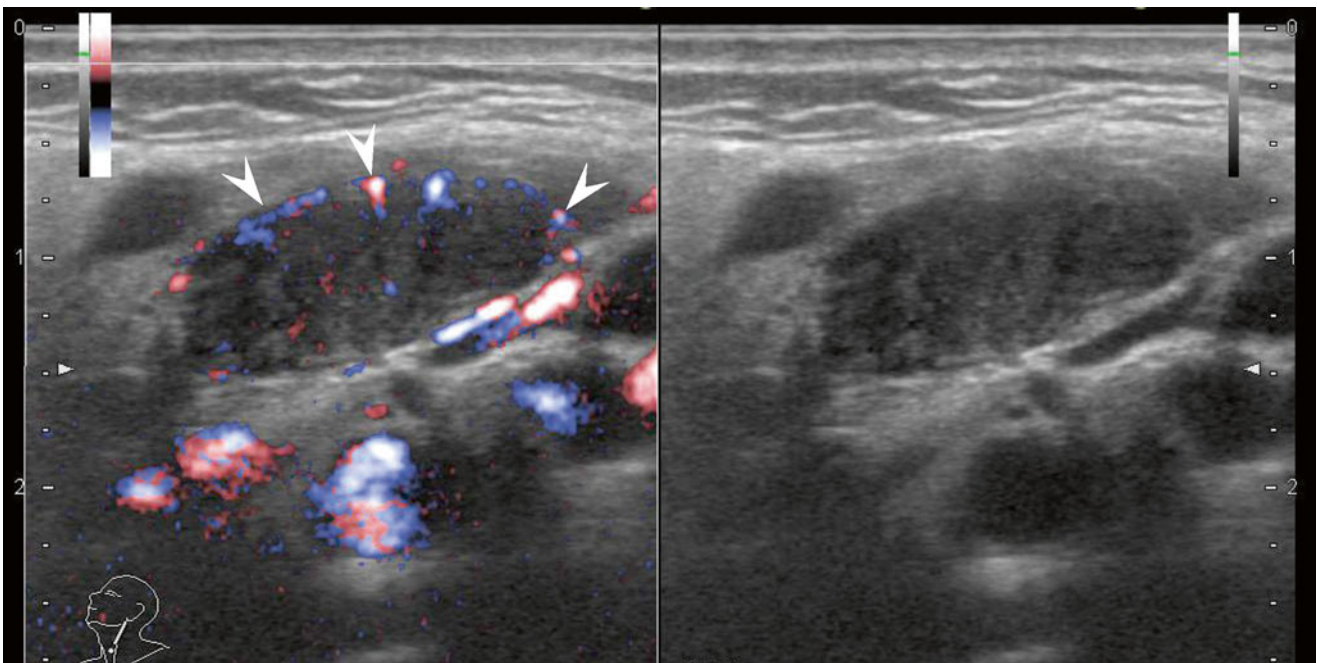


Fig. 5.128 Transverse ultrasonography at the upper neck level (left, fine flow Doppler; right, B-mode). An enlarged superior internal jugular node with an ill-defined margin is demonstrated. Note the characteristic peripheral vascularity (*arrowheads*)

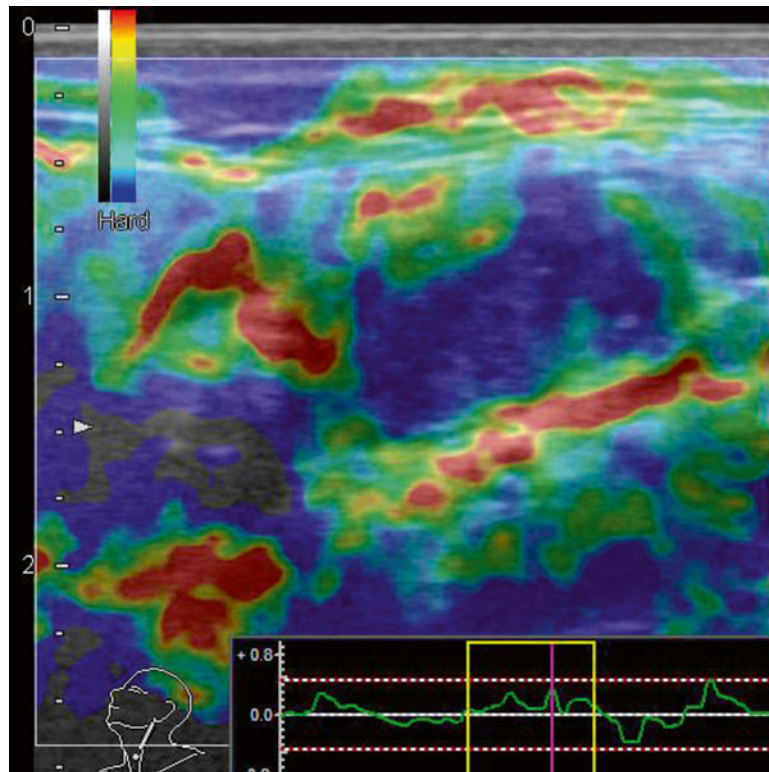


Fig. 5.129 Transverse elastosonography of the superior internal jugular node. The most part of the node is occupied with a blue, hard area suggesting malignancy

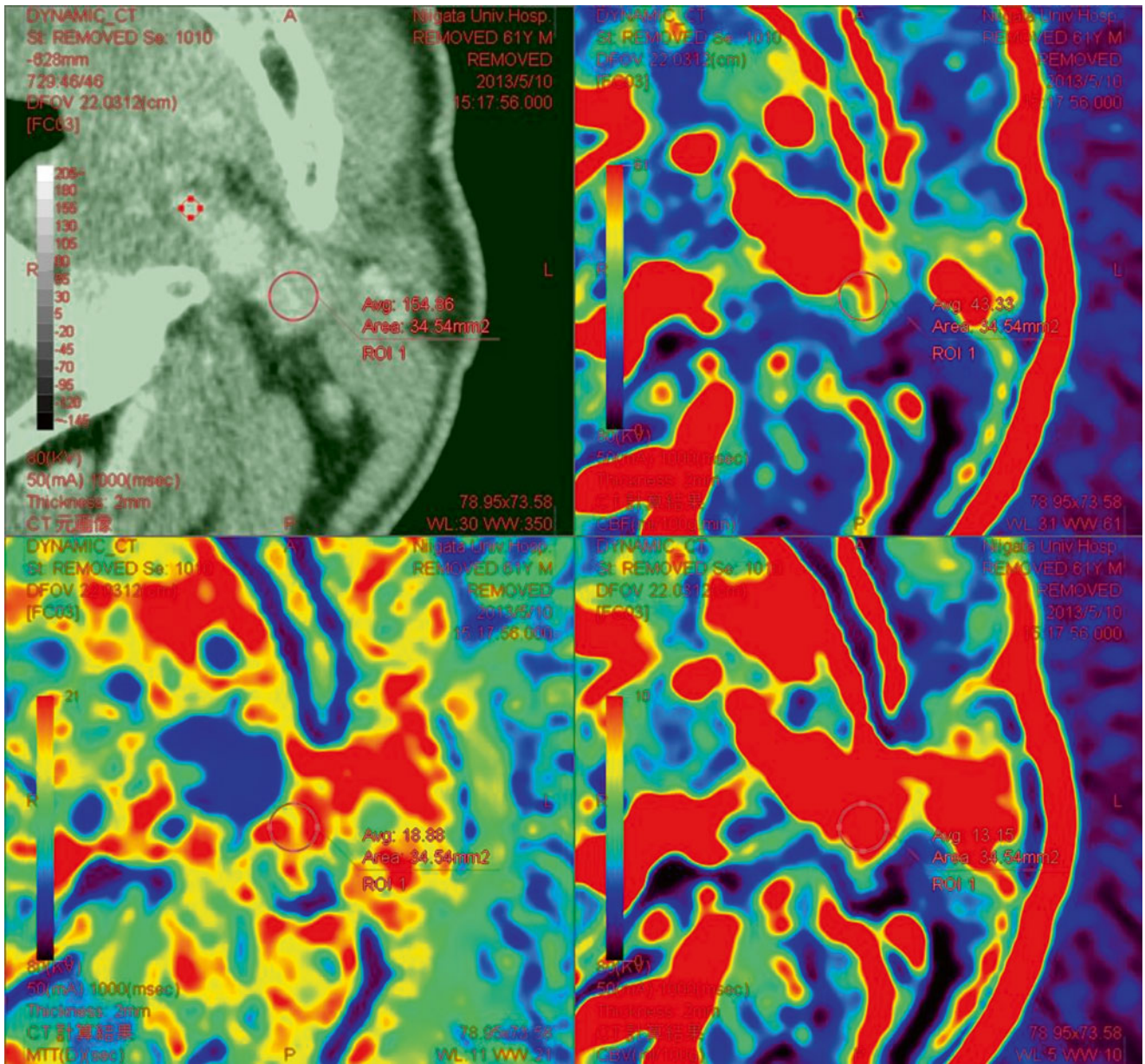
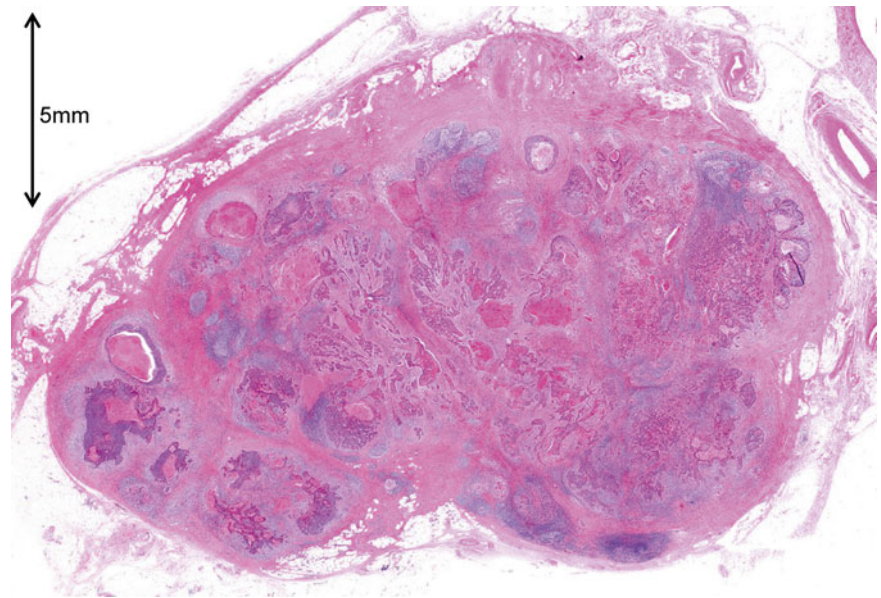


Fig.5.130 CTP at the level of the superior internal jugular node. According to the CTP analysis, blood flow and mean transit time of the superior internal jugular node present significantly different values compared with normal contralateral node

Fig. 5.131 Photomicrograph of histopathological specimen of the superior internal jugular node (hematoxylin-eosin stain)



References

- Izumo T, Ariji E, Ozeki S, Okada N, Okabe S, Okazaki Y, Omura K, Kirita T, Kusama M, Sato T, Shinohara M, Shimozato K, Shintani S, Tanaka Y, Nakayama E, Hayashi T, Miyazaki A, Yagishita H, Yamane M, Working Group 1 on the 'Guidelines for Clinical and Pathological Studies of Oral Cancer', Scientific Committee, Japan Society for Oral Tumors (2010) General rules for clinical and pathological studies on oral cancer, 1st edn. Kaneharashuppan, Tokyo
- Glastonbury CM, Harnsberger HR, Michel MA, Branstetter BF, Hudgins PA, Shatzkes D (eds) (2012) Specialty imaging: head and neck cancer: state of the art diagnosis, staging, and surveillance. Amirsys Publishing, Inc., Salt Lake City
- Som PM, Curtin HD (2011) Head and neck imaging, 5th edn. Elsevier Mosby Inc., St. Louis
- Edge SB, Byrd DR, Compton CC et al (eds) (2010) AJCC cancer staging manual, 7th edn. Springer, New York
- Izumo T, Kirita T, Ariji E, Ozeki S, Okada N, Okabe S, Okazaki Y, Omura K, Kusama M, Sato T, Shinohara M, Shimozato K, Shintani S, Tanaka Y, Nakayama E, Hayashi T, Miyazaki A, Yagishita H, Yamane M, Working Group 1 on the "Guidelines for Clinical and Pathological Studies of Oral Cancer", Scientific Committee, Japan Society for Oral Tumors (2012) General rules for clinical and pathological studies on oral cancer: a synopsis. *Jpn J Clin Oncol* 42:1099–1109. doi:10.1093/jjco/hys141